UNIVERSITY OF
LINCOLN

Computer Modelling of Block Copolymers Under External Fields

R Dessí

Doctor of Phylosophy

2016

Declaration

I declare that this thesis and the work presented in it has been planned and generated by myself and my supervisors. This work has not been reported in any previous thesis.

Roberta Dessí

Abstract

This thesis reports on modelling the morphological of Block Copolymers (BCPs) by using computer simulation. In this work, the Cell Dynamics Simulation (CDS) method is used, which is a good compromise between computational speed and physical accuracy.

First, it has been performed a 3-dimensional study of diblock copolymer standing up cylinders in two different types of confinement: topographical and chemical patterns. In the case of square walls of small sizes the system is dominated by the walls, inducing a 2x2 square lattice of cylinders, while in large boxes the system is dominated by hexagonal packing. For intermediate sizes topographical confinement has a stronger influence than chemical pattern confinement and can induce a better system of 3x3 square lattice cylinders. For square confinement compatible with a 4x4 square lattice the tetragonal phase is observed to be a transient system leading towards a twisted hexagonal packing. Simulations have also been performed in a diamond lattice which can naturally accommodate hexagonal packing, and rectangular boxes which can induce better orientation of the hexagonal lattice along the direction parallel to the long side.

Next, diblock copolymer cylinder-forming thin films confined between two parallel selective homogeneous walls have been investigated. By changing the value of the surface field and the value of the film thickness several morphologies have been observed. In order to tailor desired structures some of these morphologies are studied under a simple steady shear flow. Shear flow is observed to induce a better hexagonal packing of a monolayer of perforated lamellae and of a monolayer of cylinders perpendicular to the thin film plane. A monolayer of cylinders parallel to the thin film plane with random orientation is found to align perfectly in the shear flow direction. Further increase of the shear rate induces a phase transition: from one perforated lamellae layer to one lamellae layer; from a double layer of perforated lamellae to parallel cylinder layers; and from a monolayer of cylinders perpendicular to the thin film plane to two half parallel cylinder layers.

In the end, self-assembly of lamellae-, cylinder-, bicontinuous, and sphere-forming diblock copolymers in spherical confinement is studied. The effects of different confinement size and selective surface are examined systematically. The simulations reveal that a rich variety of morphologies, ranging from onion-like structures, perforated lamellae, helices structures, and the coexistence of perforated and lamellae structures, can be formed spontaneously from a randomly generated initial state. The structure diagrams of lamellae-forming diblock copolymers show that the morphologies obtained with a selective surface are similar to those obtained with a negative selective surface, but different to those found with a neutral selective surface. The structural diagrams of bicontinuous-, sphere-, and cylinder-forming diblock copolymers show that the morphologies found for surfaces selective for different blocks are different from each other. In the case of bicontinuous-forming diblock copolymers the morphological behaviour obtained with a neutral surface is similar to those obtained when the surface is selective for the minority block. In the case of sphere-forming diblock copolymers the morphologies obtained with a neutral surface are similar to those found with surface selective for the majority block. Instead, for cylinder-forming diblock copolymers the morphology obtained under a neutral surface is totally different from those obtained when the surface is selective.

DEDICATION

I would like to dedicate this thesis to my loving parents, and my loving sister.

Contents

Research Publications

Results of the chapter 3 have been published in:

- Dessí, R.; Pinna, M.; Zvelindovsky, A. V.

  The Cell Dynamics Simulations of Cylinder-Forming Diblock Copolymers in Thin Films on Topographical and Chemically Patterned Substrates;

  Macromolecules **2013**, 46, 1923.

Acknowledgments

I would like to use this opportunity to thank many people who have helped and supported me during this period of my study.

First and foremost, special thanks go to my PhD supervisor, Prof. Andrei V. Zvelindovsky for his wise advice, careful guidance, patience, and for the numerous opportunities to attend winter and summer schools, and UK and international conferences.

I would also like to thank my second supervisor, Dr. Marco Pinna, for his invaluable support in carrying out my simulations, technical support, help, and patience.

Many thanks to Dr. Manuela Mura for her helpful comments and support.

I am grateful to Dr. Agur Sevink, Prof. Ignacio Pagonabarraga, and Dr. Bart Vorselaars for the fruitful discussions.

I would like to thank my internal PhD examiners, Dr Martin Greenall, and my external PhD examiners, Allan Mackie (from Universitat Rovira i Virgili in Terragona, Spain), for helpful discussions.

My sincere gratitude also goes to my Laurea thesis supervisors, Prof. Luciano Colombo, Dr. Alessandro Mattoni, and Dr. Claudio Melis for their valuable feedback on the work during my PhD study.

I also wish to acknowledge with gratitude my colleague Fiona Bissett for her support, and her useful advice on my writing; and also Adele Beekem from the Library staff for her guidance and recommendations on my writing.

I am grateful to the faculty administration team, especially Debra Brown, Rachael Kuerten, Jacqueline Gray, Helen Lonsdale and my colleagues and the entire members of the department.

Last, but not least, my special gratitude goes to my parents and my sister for their love, encouragement, and support.

List of Figures

Chapter 1

Aim of the Investigation

1.1 Introduction to block copolymers

A polymer is a macromolecule, which is formed from many repeated subunits called monomers. Polymers can be natural or synthetic, and they are created by the polymerization of many small monomers. Both synthetic and natural polymers play an essential role in everyday life due to their properties. For instance, polymers can be found in synthetic plastics such as polystyrene, and in natural biopolymers such as DNA and proteins that are fundamental to biological structure and function. Regular homopolymers are made from one kind of monomers, but if there are more than one monomer type then the structure is called a copolymer. Copolymer monomers can be arranged in different ways along the chain. For instance, if the monomers are alternate one after the other the structure is called an alternating copolymer. When the monomers are distributed in a random way the morphology is called a random or statistical copolymer. A block copolymer exists when monomers are grouped by type[5], see Figure 1.1. Therefore, block copolymers (BCPs) are long chain molecules

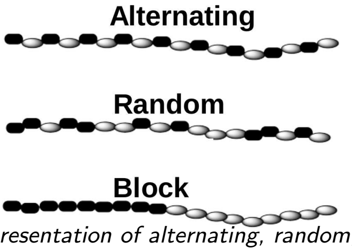

Figure 1.1: *Schematic representation of alternating, random, and block copolymer, respectively.*

consisting of two or more chemically different blocks joined together by covalent bonds. The covalent bond that connects the blocks prevents macroscopic phase separation. In contrast to crystalline solids, BCPs are soft materials which are characterized by fluid-like disorder on the molecular scale and a high degree of order at longer length scales. A stunning array of block copolymer configurations can be constructed using modern synthetic chemistry techniques. Figure 1.2 illustrates a basic classification of these molecular architectures. Depending on the chemical composition of the blocks and the molecular architecture, it is possible to observe structures such as: linear AB diblock, consisting of a long sequence of type A blocks covalently bonded to a chain of type B blocks; ABA triblocks; and A_nB_m multiblocks formed by coupling additional A and B blocks. Various chemical coupling strategies also give rise to more complex molecular topologies such as: star-AB, where blocks are not linear but are joined in the center; Y structures, the constituting molecule of graft copolymers; and linear and star ABC terpolymers. Subtle variations in the molecular topology, for instance ABC or ACB, can generate changes in the morphology and hence in the material's properties.[2]

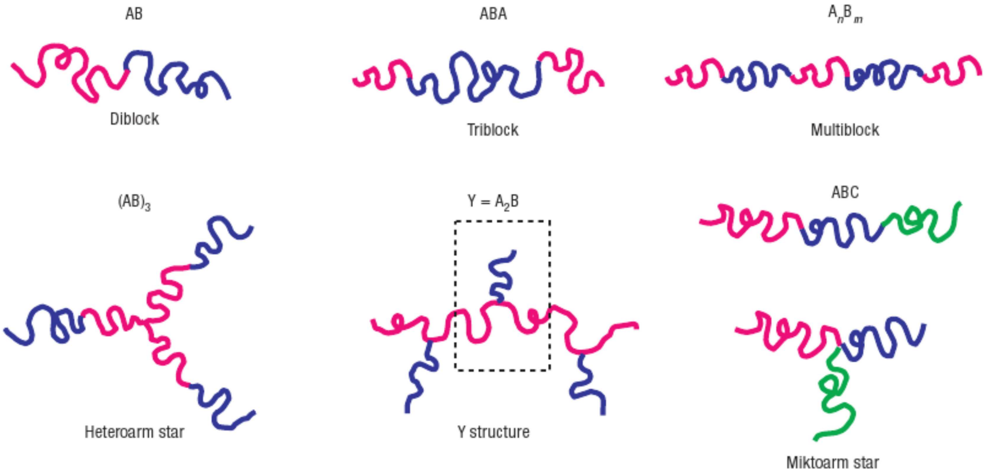

Figure 1.2: *Schematic representation of several block copolymer architectures. Red, blue, and green beads represent A, B, and C blocks, respectively.*[1]

Figure 1.2 is a schematic representation of different block copolymer structures. Such representation is an easy way to describe the chemical structure of each segment. An example of the chemical architecture is depicted in Figure 1.3.

The simplest and most studied architecture is the linear AB diblock copolymers, which spontaneously self-assembles into ordered arrays at the molecular level with a domain dimension of 10-100 nm.

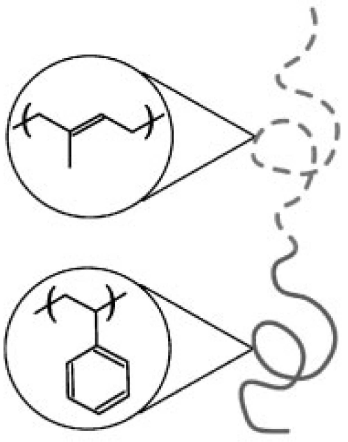

Figure 1.3: *Schematic representation of a linear diblock copolymer of poly(isoprene)–poly(styrene) (PI–PS). Dashed line describes PI monomers. Continuous line describes PS monomers.*

Classical structures in bulk are spheres (S), cylinders (C), gyroid (G) and lamellae (L).[2] Schematic examples of these nanostructures are shown in Figure 1.4 (a). The microphase separation of diblock copolymers depends on two parameters: the volume fraction f_A, where $f_A = N_A/(N_A + N_B)$; and $\chi_{AB} \cdot N$. χ_{AB} is the Flory Huggins parameter (inversely proportional to the temperature), which is the segment-segment interaction: a positive value indicates repulsion between species A and B, and a negative value indicates attraction between the same types of segment. N is the total degree of polymerization ($N = N_A + N_B$) which is the number of monomers of all types per macromolecule. Microphase separation in diblock copolymers is a situation similar to that of oil and water. Oil and water are immiscible, when they are together they phase separate. The same behaviour happens to block copolymers, due to incompatibility between the blocks. However, the blocks are covalently bonded to each other, and they cannot demix macroscopically as water and oil do.

Figures 1.4 (b) and (c) describe the phase diagrams calculated using self-consisted mean field theory and using experimental technique, respectively, that are predicted for AB diblock copolymers. In Figure 1.4 (b), for values of $\chi_{AB} > 10.5$ there are six ordered microphase structures that have been predicted which are thermodynamically stable. The lamellar structure is stable for symmetric diblocks, cylinders in hexagonal packing (C) are stable for asymmetric compositions. With increased compositional asymmetry the structure predicted is a body-centered cubic (BCC) spherical (S) phase. A very narrow region of close-packed spheres (CPS) is also detected. Another narrow region

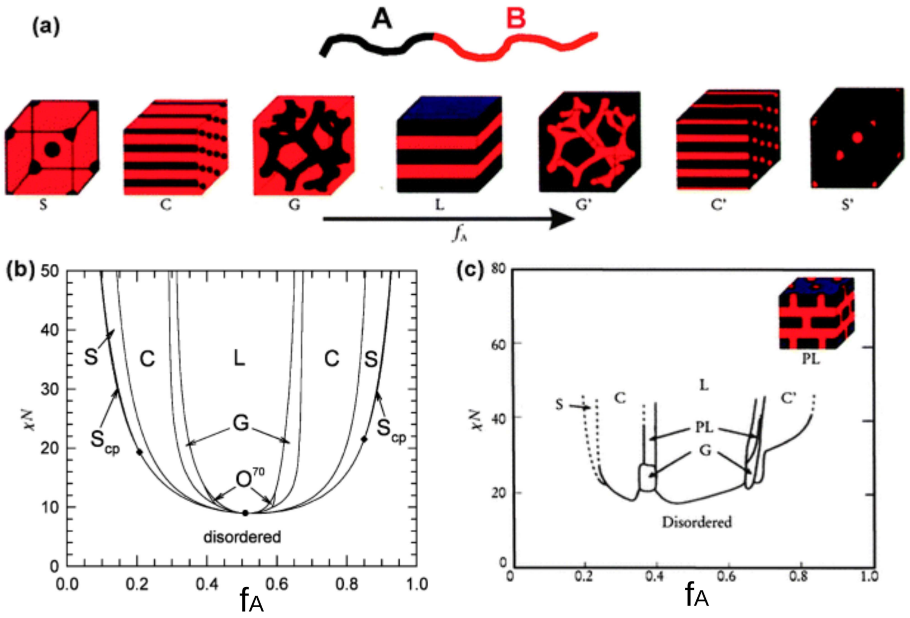

Figure 1.4: *(a) Equilibrium morphologies of AB diblock copolymers in bulk: spherical (S), cylindrical (C), gyroid (G), and lamellar (L). (b) Theoretical phase diagram of AB diblocks predicted by Self-consisted mean-field theory, depending on the composition f_A and combination parameter χN. (c) Experimental phase portrait for poly(isoprene-styrene) in which f_A represents the volume fraction of polyisoprene. PL = perforated lamellae.*[2,3]

of stability is a complex gyroid (G) phase which is predicted close to the order disorder transition (ODT) and between the L and C phases. The phase diagram for diblock copolymer also shows the stability regions of O^{70}. Figure 1.4 (c) shows an experimental phase diagram for a poly(isoprene-styrene) diblock copolymer melt. The experimental diagram is similar to the theoretical one, although there are a few differences. First of all the experimental phase diagram is asymmetric with respect to f_A. This is due to the fact that styrene and isoprene monomers have different sizes and shapes. The experimental phase diagram also exhibits a complex phase called perforated layers (PL). Although this structure has been studied theoretically, it has never been found to be the phase of lowest free energy.[6] Stability of PL comes from finite size of the system. Another difference between the experimental and the theoretical phase is related to the region order-disorder transition. As we can see from Figure 1.4 (c) in the experimental curve the disordered phase is stable beyond $\chi_{AB} = 10.5$ (for $f_A = 1/2$) and transitions between the disordered phase and the various ordered phases are possible. However, the theoretical diagram shows that the order-order curves all converge to a critical point at $\chi_{AB} = 10.5$ for $f_A = 1/2$, and only direct phase transition between the disordered phase and the spherical (BCC and CPS) ordered phases are allowed.

Due to their interesting property of forming regular nanometer-scale patterns, BCPs have attracted great attention from various research groups around the world[7–11]. From a technological point of view, control of the formation and orientation of the nanostructures is important to generate long-range ordered morphologies.[12] Microstructures generated in copolymer melts can be used, for instance, as templets for electronic devices with sizes of less than 30 nm, which are difficult to achieve with traditional methods of photolithography or electron beam lithography.[12] However, BCP nanostructures can not be generated periodically at large scales in the absence of external fields. For this reason, interest has arisen in examining the structure of block copolymer melts under external fields, such as: surface fields, electric fields, and shear flow.[12] Surface fields are, in particular, prominent in confined geometries. Nanoconfinement of block copolymers presents an opportunity to generate scientifically interesting and potentially useful morphologies that are not usually present in the bulk. When block copolymers self-assemble in a physically confined environment, the geometric constraints, imposed by the confinement and the interactions between the blocks and the confinement surface, play important roles in molecular organizations. In fact the domain spacing and the intermaterial dividing surface (IMDS, interface between the domains of each block containing the covalent junction point) shapes are usually perturbed from their bulk values and forms.[13]

The confinement in a thin film is called 1-dimensional (1D) due to one restricted direction. Thin films of BCPs have been used as templates to fabricate nanowires,[14–17] nanopores,[18] quantum dots,[19] magnetic storage media,[20] and silicon capacitors.[21]

When block copolymers self-assemble in cylindrical nanopores the confinement is called 2-dimensional (2D). This kind of confinement can give rise for instance to helices, and concentric lamellae morphologies. Helices are very important for instance for the creation of chiral materials that may have novel mechanical, optical or electronic properties. Also concentric lamellae can have applications in drug delivery or as waveguides and other photonic materials.[13]

When block copolymers self-assemble within sphere or ellipsoid the confinement is called 3-dimensional (3D). Such system can potentially serve as building material for intelligent nanosize bioreactors and vesicles as drug delivery vehicles or self regulating diagnostic devices.[22,23]

1.2 Motivation and outline of the present thesis

The aim of the present thesis is to study the phase behaviour of diblock copolymers (BCPs) under external fields. Most of our studies, which are presented in this thesis, are compared with experiments and numerical work where possible. From an experimental point of view, it still remains very difficult to follow block copolymer phase transitions, and most of the information gathered is on static images. Moreover, block copolymer experiments are difficult and expensive. Computer modelling helps to understand morphological features and the kinetics of ordering of block-copolymer morphologies, which is essential for the prediction of pattern formation in block copolymer structures. Therefore, this thesis aims to contribute to the understanding of and improve the study of the pattern formation processes of block copolymer nanostructures.

In this thesis we used the Cell Dynamics Simulation (CDS) method which is a fluid-based coarse-grained model useful for studying the phase transition of our BCP structures at the mesoscale level. In **Chapter 2**, we present CDS, which is a good compromise between computational speed and physical accuracy.

In **Chapter 3**, we explore the conditions for which self-assembly in hard- and soft-confined thin cylinder-forming diblock copolymer films results in tetragonal square arrays and in hexagonal packing of standing up cylinders. The different effect of confinements are observed on the degree of imperfection in the tetragonal phase.

In **Chapter 4**, the phase behaviour of cylinder-forming diblock copolymers confined between two parallel slits are investigated by changing the surface field and the film thickness. To tailor a desired structure, some of the previously obtained morphologies are manipulated by a steady shear flow. We note that shear flow can improve microdomain order, and when above a certain critical value can induce morphology phase transition. Moreover, we observe that hexagonal packing of the microdomains can be either parallel or perpendicular to the shear flow direction.

In **Chapter 5**, the self-assembly of lamellae-, cylinder-, bicontinuous-, and sphere-forming diblock copolymers under 3-D spherical confinement is studied. We investigate the BCP phase behaviour by changing the selective surface and the confinement space.

The calculation results reveal the different selective surface effects as a function of the block copolymer composition.

In **Chapter 6**, we draw general conclusions from our findings, exhibited in the above chapters.

In **Appendix A**, we describe our Fortran code which we have developed to detect the 2-dimensional coordinates of microdomain center of mass, starting from a 3-dimension structure of BCP cylinders perpendicular to the thin film plane confined within hard and soft walls. The application of our Fortran code is followed by Voronoi Diagram analysis, useful for the microdomain defect identification.

Chapter 2

Mesoscale simulation technique

Synopsis

In this chapter we describe the mesoscale simulation technique which we used to study diblock-copolymers under external influences. Using Cell dynamics Simulation we studied the behaviour of diblock-copolymer thin films: laterally confined, results in Chapter 3; under a steady shear flow, results in Chapter 4, and under three dimensional confinement, results in Chapter 5.

2.1 Introduction

In order to study diblock copolymers different computer modelling techniques have been employed,[24–27] for instance molecular dynamics (MD), Monte Carlo (MC), Cell Dynamics Simulation (CDS), static self-consistent field theory (SCFT) and dynamics SFCT (DSCFT, also known as dynamics density functional theory (DDFT)). Some of them are very accurate but very slow, others are very fast and less accurate but not less useful.[24] Latter ones are typical characteristics of the mesoscopic simulation techniques which are able to describe the behaviour of block copolymers on a large scale. Cell Dynamics Simulation (CDS) is one of these techniques. CDS is a widely used technique to study the micro phase separation of block copolymers.[25,28] The cell dynamics simulation is a fast method compare to SCFT and can be performed in boxes similar to the typical experimental size.[25,28] However, experimental size system and experimental times cannot be achieved even with this method on modern single processor computers. This hurdle has been overcome by Pinna et al., who created a computer algorithm which can run using many processor in parallel.[29,30] The numerical results indicate that the proposed parallel algorithm can provide an efficient way for computer simulation of block copolymers systems of experimental size, for instance $2\mu m$.[31]

The cell dynamic simulation method is a method developed to model interface dynamics in phase-separating systems.[32,33] The time evolution of an order parameter is evaluated on a lattice, according to two mechanisms. The first arises from the local driving force due to the chemical potential gradients. The second allows for the connectivity of the cells and corresponds to diffusive dynamics due to order parameter variations in neighboring cell.[25] Because it is a fluid-based coarse-grained model CDS ignores detailed structural information concerning polymer chains such as bond length, bond angle and chain length. A density potential is used to replace interactions between monomers. In addition, CDS can provide both statistic and dynamical information concerning phase transition.[34] Although in this work we focus on CDS for BCPs, CDS can be used for instance even for polymer-dispersed liquid crystal[35], polymer crystallization[36,37], and biological systems such as binary lipid membranes.[38]

Cell Dynamics Simulation is used to study BCPs under external influences, such as, shear flow[39,40], electric field[39,41,42], confinement[43–45], and polymer-particle composites[46]. Some example are reported below. CDS has been used to study pathways of spheres-to-cylinder transition in a bulk block copolymer melt under applied simple shear flow.[39] Results show that shear flow can induce the transition when the shear rate is above some critical value which is in agreement with earlier result of DSCFT.[40] The spherical phase is preserved at small shear rates, with spheres being deformed into ellipsoids, in agreement with earlier simulations.[40] Moreover the results show sliding of layers of spheres under shear already reported by DSCFT, where the arrangement of the spheres in layers was not perfect due to the relatively small box size.[40] Therefore, CDS findings confirm the importance of large scale simulations in BCPs. A large scale 3D CDS of sphere-to-cylinder transition under electric field has been reported in reference[39]. Results show that the electric field should exceed a certain threshold in order to induce a transition. These results are in agreement with experimental and theoretical results by DSCFT on sphere-to-cylinder transition.[41,42] CDS has been successfully applied for confined morphologies[43]. By using CDS lamellar-, cylinder-, and sphere-forming diblock copolymers melts in cylindrical nanopores has been studied. It was shown that CDS method can predict a rich zoo of diblock copolymer morphologies in cylindrical nanopores. These findings are in good agreement with DDFT simulations.[44,45] Block copolymer-nanoparticle composites is another example of complex block copolymer system studied with CDS. The interaction between diblock copolymer and nanoscopic particle can lead to some morphologies depending on the polymer compositions as well as on shapes, size, and surface treatment of the particles. In reference[46] CDS has been combined with Brownian dynamics of soft particles in 2D. The result is that the presence of the particles can influence block copolymer morphologies. In this thesis CDS is used to study BCPs: confined within soft- and hard-confinement, Chapter 3; confined between two parallel walls without and with shear flow, Chapter 4; and under spherical confinement, Chapter 5.

2.2 The Cell Dynamics Simulation

For an AB diblock copolymer melt the order parameter $\psi(\mathbf{r},t)$ at point $\mathbf{r}$ and at time t is defined as:

$$\psi(\mathbf{r},t) = \phi_A(\mathbf{r},t) - \phi_B(\mathbf{r},t) + (1-2f) \tag{2.1}$$

where $\phi_A(\mathbf{r}, t)$ and $\phi_B(\mathbf{r}, t)$ are the local volume fraction of A and B monomers respectively, and f is the volume fractions of A monomers in the diblock, $f = N_A/(N_A+N_B)$. In the cell dynamics simulation the time evolution of the order parameter is given by a Cahn-Hilliard equation:[47]

$$\frac{\partial \psi(\mathbf{r}, t)}{\partial t} = M\nabla^2 \left(\frac{\delta F\left[\psi\right]}{\delta \psi} \right) \tag{2.2}$$

where M is a phenomenological mobility constant. Here we set M=1 which correspondingly sets the timescale for the diffusive processes (the dimensionless time is tM/a_0^2, where the lattice cell size a_0 is set to 1). In Eq. 2.2 $F\left[\psi\right]$ is the free energy functional divided by kT, which can be written as:[48]

$$\begin{aligned} F[\psi(\mathbf{r})] &= \int d\mathbf{r}[H(\psi) + \frac{D}{2}|\nabla\psi|^2] \\ &+ \frac{B}{2}\int d\mathbf{r}\int d\mathbf{r}' G(\mathbf{r}-\mathbf{r}')\psi(\mathbf{r})\psi(\mathbf{r}') - \sum_i \int s_i(\mathbf{r})\psi(\mathbf{r})d\mathbf{r} \end{aligned} \tag{2.3}$$

where the first term, $H(\psi)$, contains the local contributions to the free energy and the second term, $\frac{D}{2}|\nabla\psi|^2$ gives the free energy involved in creating an interface between the A and B polymers. The third term is derived from the Hamiltonian of a diblock copolymer melt[49] and contains the information about the connectivity of the polymer chains. The Green's function $G(\mathbf{r}-\mathbf{r}')$ for the Laplace equation that appears in this term satisfies $\nabla^2 G(\mathbf{r}-\mathbf{r}') = -\delta(\mathbf{r}-\mathbf{r}')$.[12] The chain conformations are described by the Green's function. The final term, where i denotes either the A or B block copolymer component, accounts for the interaction of the block copolymer with the surfaces of confinement. The full form of $H(\psi)$ is[25]:

$$H(\psi) = [-\frac{\tau}{2} + \frac{A}{2}(1-2f)^2]\psi^2 + \frac{v}{3}(1-2f)\psi^3 + \frac{u}{4}\psi^4 \tag{2.4}$$

Here, τ is a temperature parameter and A, v, u, B, and D are constants.[50] Since our intention is to model the broad phenomenology of block copolymer self-assembly, and not the structures formed by a specific polymer, we allow the freedom of choosing the values of these constants so that the copolymers form the bulk structure (for example, cylinders) whose modification by confinement we wish to study. In principle, all these parameters can be related to molecular characteristics, but we will not use this approach here. According to Ohta and Kawasaki $\tau' = -\tau + A(1-2f)^2$, D, and B can be expressed in terms of degree of polymerization N, the segment length b and the Flory-Huggins parameter χ (which is inversely proportional to temperature)[49]. Positive values of χ-parameter indicates net repulsion between species A and B, whereas a negative value indicates a free-energy drive towards mixing. The expressions are:

$$\tau' = -\frac{1}{2N}(N\chi - \frac{s(f)}{4f^2(1-f)^2}) \qquad D = \frac{b^2}{48f(1-f)}, \qquad B = \frac{9}{4N^2b^2f^2(1-f)^2} \tag{2.5}$$

where $s(f)$ is an empirical fitting function of the order of 1 (*e.g.* $s(0.5)$=0.9, $s(0.3)$= 1.0).[49] In simulation we use dimensionless parameters $\tilde{D} = D/a_0^2$ and $\tilde{B} = Ba_0^2$ (for simplicity we keep notations D and B instead of $\tilde{D}$ and $\tilde{B}$). The parameters u and v do not allow for a compact representation and can be computed by evaluating the appropriate vertex function given by Leibler.[51] These are very complex functions that can be only approximately replaced by constants.

In Cell Dynamics Simulation the time is dimensionless. The expression that describes the duration of a simulation is time = time-steps $\cdot\Delta t$, where Δt is the dimensionless numerical time step. The dimensionless numerical time step Δt is connected to the physical time step $\Delta t'$ by the relation $\Delta t = Dd^2a^{-2}\Delta t'$. D is the diffusion coefficient, d is the stencil coefficient, and a is the bond length.[52]

2.2.1 Surface field applied in chapter 3

In Chapter 3, the expression of the third term in Eq. 2.3 for the case of BCPs within topographical wall confinements, computationally emulated, is:

$$s_i(x, y, z) = h_i \cdot \phi_i \cdot (\tilde{\delta}_x + \tilde{\delta}_z - \tilde{\delta}_x \cdot \tilde{\delta}_z) \tag{2.6}$$

where h_i is the strength of the interaction between the walls and the segments i, where i denotes A or B block copolymer components. The expression of the local volume fraction of A and B monomers are, respectively, $\phi_A = f + \psi/2$, and $\phi_B = 1 - f - \psi/2$, which are obtained using Eq. 2.1 and the incompressibility condition $\phi_A + \phi_B = 1$. In addition:

$$\tilde{\delta}_j = \begin{cases} 1, & j = \{1, N_j\}, j = x, z \\ 0, & \text{otherwise} \end{cases} \tag{2.7}$$

where N_j is the size of the wall in the j-direction. In the case of BCPs in chemically patterned surfaces, computationally emulated, the third term in the Eq. 2.3 is:

$$s_i(x, y, z) = h_i \cdot \phi_i \cdot (\tilde{\delta}_x + \tilde{\delta}_z - \tilde{\delta}_x \cdot \tilde{\delta}_z) \cdot \delta_{y1} \tag{2.8}$$

In addition:

$$\tilde{\delta}_j = \begin{cases} 1, & 1 \leqslant j \leqslant w \text{ or } N_j - w \leqslant j \leqslant N_j, j = x, z \\ 0, & \text{otherwise} \end{cases} \tag{2.9}$$

where w is the width of the chemical stripe and δ_{ab} is the Kronecker delta.
In both case, topographical and chemical wall confinements, reflective boundary conditions are applied in x- and z-direction, and periodic boundary conditions are applied in y-direction.

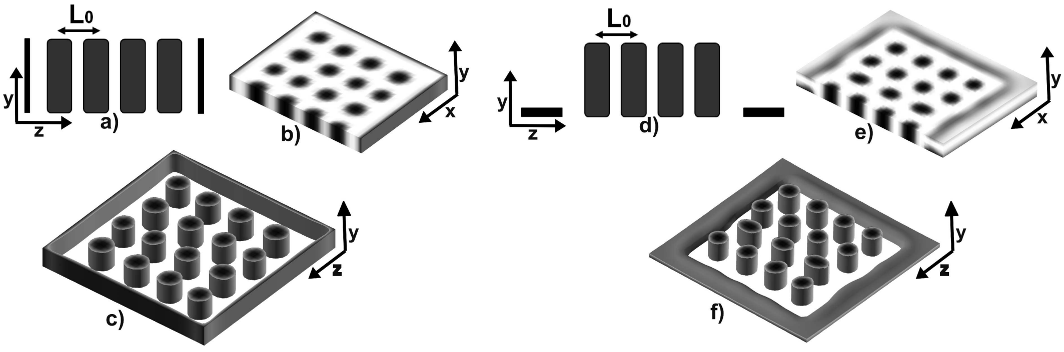

Figure 2.1: *Simulation setups: hard walls confinement (a-c); (a) BCP cylinders confined by hard walls, which are depicted as black vertical bars in the cartoon, (b): volume representation of typical simulation with a cut through, (c): iso-surface representation ($\psi_{\text{iso}} = -0.18$). Soft walls confinement (d-f); (d): BCP cylinders confined by a chemical pattern on a substrate, which is depicted as black horizontal bars in the cartoon, (e): volume representation of typical simulation with a cut through, (f): iso-surface representation ($\psi_{\text{iso}} = -0.18$) with the top layer of the chemical square pattern removed for visualization purposes (compare with the image e).*

2.2.2 Surface field applied in chapter 4

In Chapter 4, we study BCPs thin film confined between two surface field parallel walls under a steady shear flow defined by:

$$v_x = \dot{\gamma} y, v_y = v_z = 0 \tag{2.10}$$

where we take the x-axis in the flow direction, y-axis in the velocity gradient direction. Dimensionless shear rate is $\tilde{\dot{\gamma}} = \dot{\gamma}\ a_0^2/M$ The Cahn-Hilliard equation, introduced in Eq. 2.2, with the shear flow contributions becomes:

$$\frac{\partial \psi(\mathbf{r}, t)}{\partial t} + \nabla \cdot (\mathbf{v}\psi) = M\nabla^2 \left(\frac{\delta F\left[\psi\right]}{\delta \psi} \right) \tag{2.11}$$

where $\mathbf{v} = (v_x, v_y, v_z)$ is the flow. In this case the third term, accountable for the interaction between block copolymers and the surfaces[12], equation 2.3, is:

$$s_i(x, y, z) = h_i \cdot \phi_i \cdot (\delta_{y1} + \delta_{yL_y}) \tag{2.12}$$

where i denotes A or B block copolymer component. If i=A or i=B, the local volume fraction of A and B monomers are, respectively, $\phi_A = \frac{\psi}{2} + f$ and $\phi_B = -\frac{\psi}{2} + 1 - f$, obtained by combining $\phi_A + \phi_B = 1$ for the incompressibility of the system, and equation 2.1; h_i is the strength of the interaction between the walls and the segments; δ_{ab} is the Kronecker delta; and L_y is the distance between the parallel walls. Reflective boundary conditions are applied in y-direction and periodic boundary conditions are applied in the x- and z-directions.

2.2.3 Selective surface applied in chapter 5

In Chapter 5, we study self-assembly of BCPs within spherical confinement, by changing the selective surface and confinement dimension. The Cahn-Hilliard equation, introduced in Eq. 2.2, with noise contributions applied at each time step for only one system becomes:

$$\frac{\partial \psi(\mathbf{r}, t)}{\partial t} = M\nabla^2 \left(\frac{\delta F\left[\psi\right]}{\delta \psi} \right) + \eta \xi(\mathbf{r}, t) \tag{2.13}$$

The last term in Eq. 2.13 is a noise term where η is the amplitude of the noise and $\xi(\mathbf{r}, t)$ is a normalized Gaussian random noise, which satisfies the fluctuation-dissipation theorem. Moreover, in this case the expression of the third term in Eq. 2.3 is:

$$\psi(R_0) = \psi_0 \tag{2.14}$$

it has been chosen the most simple model for the boundary condition, in which the preference of copolymer blocks to the surface is described by Dirichlet boundary conditions $\psi(R_0) = \psi_0$. Therefore, varying ψ_0 we effectively model the affinity of the surface towards one or another block copolymer component. R_0 is the radius of the spherical confinement.

2.3 Conclusion

Cell Dynamics Simulation is a fluid-based coarse grained model which provides an efficient way to simulate microphase separation. In this thesis the focus is on the application of the CDS method to simulate microphase-separated structures in block copolymers (BCPs) and the kinetics of microphase separation. CDS can describe the behaviour of BCPs on a large scale, where molecular details can be neglected. CDS is a fast method compare to SCFT[25] and can be performed in a large box comparable with real experimental system size.[25,28] Additional surface field functions have been inserted in the CDS code in order to describe the interaction between block copolymers and the surface.

Chapter 3

The Cell Dynamics Simulations of Cylinder-Forming Diblock Copolymers in Thin Films on Topographical and Chemically Patterned Substrates

Synopsis

Using 3-dimensional Cell Dynamics Simulation, described in Chapter 2, it has been demonstrated that the tetragonal phase of cylinder forming diblock copolymers can be induced on both topographical and chemical patterned substrates. The results quantitatively describe the different effect of both substrates on the degree of imperfection in the tetragonal phase observed in recent experiments [Xu, J. et al, Soft Matter **2011**, *7, 3915]. Comparative analysis of the structural evolution for different thermal noise level in square, rectangular and diamond-shape lateral confinements is performed.*

3.1 Introduction

The present study is motivated by the need to understand the complex behaviour of cylinder-forming block copolymers confined in thin films within lateral square geometries observed in recent experiments.[53] The square geometry is incompatible with the bulk packing symmetry of the cylinder microdomains, however, it represents a convenient geometry for circuit design in nano-electronics.[4] Study of BCPs on patterned substrates has a long history. Topographical trenches and hexagon wells were used to improve lateral ordering in sphere-forming BCPs in Refs.[54,55]. Such topographic templates can be fabricated, for instance, by electron-beam lithography.[56,57] The topographical features can have intricate shapes, for example, saw-teeth.[58] Use of chemical patterns to direct orientation of lamellae microdomains was originally demonstrated in Ref.[59]. Later it was shown that chemical patterns can direct self-assembly of lamellar domains into parallel lines of arbitrary length.[60] Recently a large scale hexagonal ordering of BCP cylinders was investigated using a set of chemical patterns, such as hexagonal, triangular, diamonds and stripes.[61]

A related approach is to use pinning point-like objects instead of topographical edges or chemical continuous patterns. For instance, hexagonal arrays of posts or chemical "dots" were used in Refs.[62,63] in order to guide BCP self-assembly into large scale patterns. In a similar approach, square array of chemical dots was used to induce square symmetry in BCP thin films.[64]

On the theoretical side, Fredrickson and co-workers have investigated BCPs confined in hexagonal and square boundaries by means of two-dimensional self-consistent-field theory (SCFT).[4,65] The sides of the hexagons were about five cylindrical domain spacings[65] and tree and four domain spacings for the squares,[4] which restricts comparison with the experiments only to small systems. Moreover, two-dimensional simulation can not distinguish between topographical and chemical pattern of the same geometry. To fully describe such systems it was suggested to conduct three-dimensional simulations.[4] SCFT remains one of the best available tools to study complex BCP systems,[66] however it is computationally expensive even with modern computational power. Therefore, in the current work we choose a more coarse grained method based on a Ginzburg-Landau type phenomenology, the cell dynamics simulation (CDS).[32] It is a relatively fast method (see the review[25] for a comparative estimate of CDS and

DDFT run times) and has a good record of describing rather complex experimental phenomena in BCPs.[25,28] CDS uses a real space diffusion dynamics to minimize the free energy of BCP systems in the spirit of Cahn-Hilliard-Cook theory.[67,68] Followed by the success of CDS type models in polymer phase separation kinetics the diffusion minimization dynamics was also introduced into the dynamic SCFT, also know as Dynamic Density Functional Theory (DDFT).[69] More recently other flavours of dynamic SCFT have incorporated artificial kinetics for the free energy minimisation.[4,70] Although very simple, the diffusion dynamics with a constant mobility coefficient was proven to quantitatively describe an order-order transition kinetics in block copolymer morphologies within the framework of DDFT by direct comparison with the dynamic Atom Force Microscopy.[71] This diffusion dynamics with constant mobility coefficient was also able to describe experiments in non-equilibrium block copolymer systems (diffusion-convection model for BCP under shear).[72] Recently CDS approach was validated against SCFT in a considerable detail. For instance, transition kinetics of spherical morphology under shear and electric field was investigated by both methods as well compared with the experiments.[39,40,42] Similar studies were conducted for gyroid morphology under shear and electric field using CDS and dynamic SCFT.[73–75] Most recently CDS and DDFT were validated against each other for the intricate transition dynamics of lamellae under electric field.[76–78] CDS method was also validated against DDFT for complex confined system such as a block copolymers in pores.[43,45] Using CDS we investigate square and oblique cell confinement of various sizes and compare the effect of topographical and chemical patterns on the BCP ordering. Our results answer some open questions put forward by the recent experiments.[53]

3.2 Results and discussion

3.2.1 Model system

The system of interest is a cylinder-forming BCP with $f = 0.4$. For such a system the parameters entering in Eq. 2.2 are $A = 1.5$, $B = 0.02$, $D = 0.5$, $v = 1.5$, $u = 0.5$, $\tau = 0.3$, as has been used in earlier works on BCP cylinders confined within spherical enclosure or in cylindrical pores.[43,79] First we perform a simulation in a laterally large box L_x=200, L_y=5, L_z =200 grid points and determined the natural bulk spacing of the cylindrical morphology being $L_0 \sim 7.4$ grid points. Figure 2.1 shows two simulation setups. The images 2.1 a-c illustrate the BCP system confined inside solid square walls while the images d-f represent the system where the structure is restricted by the chemical patterned square of side width $w = 6$ (see Eq.2.8). The confinement in the second setup, images 2.1d-f is due to so called soft walls formed by a thin lamellar layer, images 2.1f. In all simulations the interactions with the surfaces are set to $h_A = 0.4$, $h_B = 0$ and the value of the film thickness to $L_y = 0.7L_0 = 5$ grid points, which is close to the thickness of the experimental BCP films in Ref.[53]. In all simulations the random was applied only at the initial timestep.

3.2.1.1 Hard walls confinement

Figure 3.1a-d shows the time evolution of several BCPs patterns in topographical confinement, using setup shown in Figure 2.1a-c. Figures 3.1a and b show evolution within squares accommodating three cylinder domain spacings for an initial noise level $\psi_0 = \pm 0.05$ and $\psi_0 = \pm 0.5$, respectively. The time evolution of the system with the smaller initial noise level is dominated by the walls as the microphase separation initially starts near to the walls and then proceeds into the middle of the square. As a result the system retains square symmetry at every stage of its development and the final configuration is a rather stable square array of nine cylinders (see Figure 3.1a). However, the microphase separation for the system with higher noise starts everywhere in the sample with only mild influence of the walls. As a result, the development proceeds via a series of highly defected structures and finishes with a very slightly “twisted cubic” morphology (see Figure 3.1b). Behaviour of the patterns confined in the larger square (accommodating four cylinders domain spacings) is shown in Figure 3.1c-d for two values of the initial noise. Again at the lower noise level the structure development is dominated by the presence of the walls and consists of a series of highly symmetric morphologies (see Figure 3.1c). However, the relative influence of the wall in the larger square is weaker compared to the smaller squares. As a result after arriving first at a perfect cubic array (Figure 3.1c, $t = 2\,000$ TMS) the system with the lower noise transforms into a clearly twisted cubic array or twisted hexagonal array in terminology of Ref.[4] (see Figure Figure 3.1c, $t = 100\,000$ TMS). For the system with higher noise the time evolution is similar to the case with smaller square (see Figure 3.1b):

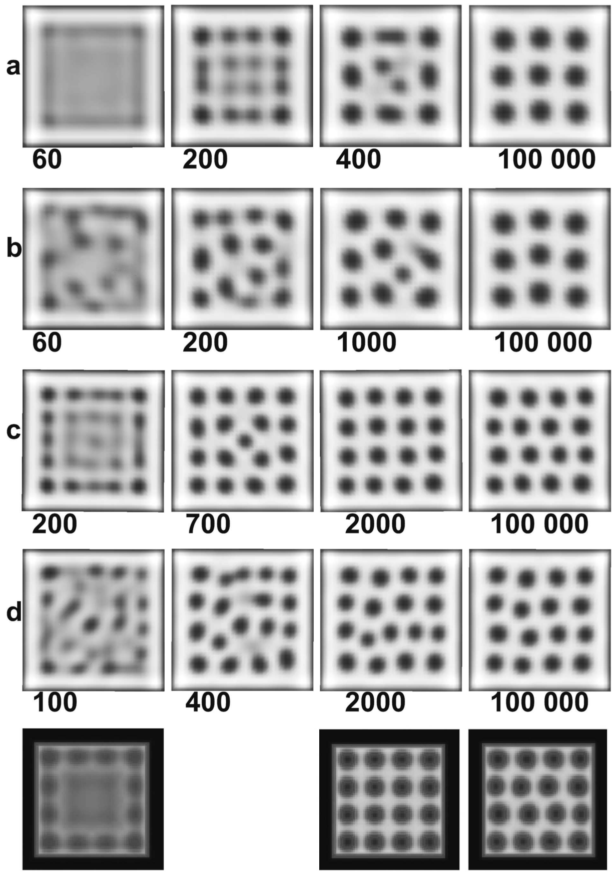

Figure 3.1: *BCP confined in squares with hard walls as a function of timesteps (TMS). (a-d): top view on the 3D CDS results. Initial noise level (a,c):* $\psi_0 = \pm 0.05$*, (b,d):* $\psi_0 = \pm 0.5$*. Box sizes are: (a-b):* $L_x = L_z = 30$ *and* $L_y = 5$ *grid points, (c-d):* $L_x = L_z = 37$ *and* $L_y = 5$ *grid points. Bottom row: 2D SCFT simulations from Ref.*[4]*: the sequence shows different snapshots of the numerical iteration procedure towards the minimum energy configuration.*

the microphase separation starts everywhere in the sample and the structure development proceeds via series highly defected morphologies directly to a twisted hexagonal array (see Figure 3.1d). Therefore, the ultimate morphologies for this square size is the twisted hexagonal array regardless the noise level, however the pathways toward these morphologies are different depending on the initial noise level. These pathways are found to be of two types: either ones which initiate at the walls or everywhere in the sample. We performed the same simulations with an even higher noise level ($\psi_0 = \pm 1$, the same random seed as before) and found that the time evolution for the noise level $\psi_0 = \pm 0.5$ and $\psi_0 = \pm 1$ is practically the same and follows the morphology sequence shown in Figure 3.1b and d. Our 3D simulations qualitatively agree with the earlier SCFT calculations[4] (due to the absence of noise in the numerical scheme[4] the comparison should be done with our results for a lower noise level). In the case of square of three domain spacings both methods produce cubic array of 9 cylinders (Figure 3.1a, corresponding results in Ref.[4] is only described but not shown). In the case of four cylinder domain spacing there is a striking similarity between our images: 2D SCFT calculations yield initial microphase separation at the walls, then developing in a perfect cubic array of 16 cylinders and finally ending up in a twisted hexagonal morphology (see Figure 3.1 bottom).

3.2.1.2 Soft walls confinement

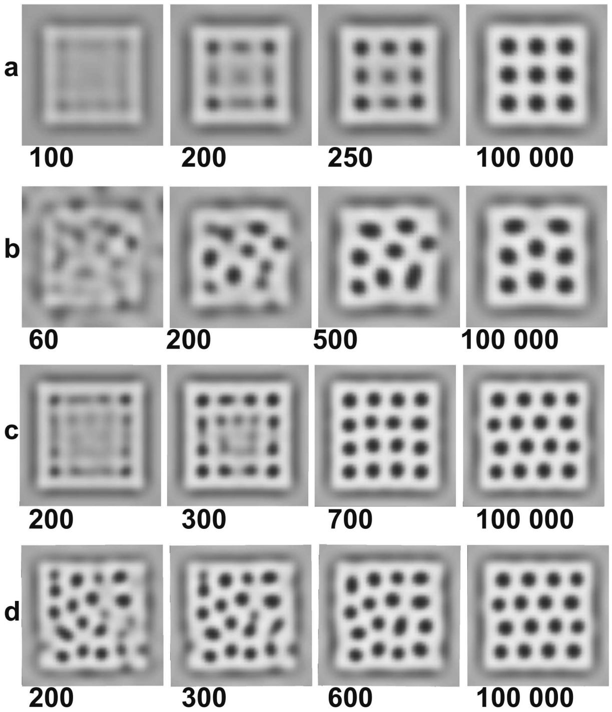

Figure 3.2: *BCP confined in squares with soft wall as function of timesteps (TMS).(a-d): top view on the 3D CDS results. Initial noise level (a,c):* $\psi_0 = \pm 0.05$*, (b,d):* $\psi_0 = \pm 0.5$*. Box sizes are: (a-b)* $L_x = L_z = 26$ *and* $L_y = 5$ *grid points. (c-d)* $L_x = L_z = 39$ *and* $L_y = 5$ *grid points.*

In this subsection the previous analysis is extended to the case of BCPs confined by a chemical pattern as shown in Figure 2.1d-f. Figure 3.2 shows the time evolution of square accommodating three and four cylinder domain spacings for two noise levels $\psi_0 = \pm 0.05$ and $\psi_0 = \pm 0.5$. General features of the time evolution are similar to the case of hard walls. At the lower level of the initial noise the microphase separation starts at the walls and proceeds via the set of highly ordered structures, Figure 3.2a,c. The influence of the walls is weaker for the larger system which develops into the twisted hexagonal morphology preceded by almost perfect square array of 16 cylinders,

Figure 3.2c. For the larger noise level the microphase separation starts everywhere in the sample and proceeds via a series of highly defected morphologies ending up in a twisted hexagonal structure for the larger system, Figure 3.2d. However, for the smaller system and for the larger noise level the system gets trapped in a defected though symmetric morphology, Figure 3.2, $t = 100\,000$ TMS. That result is somewhat

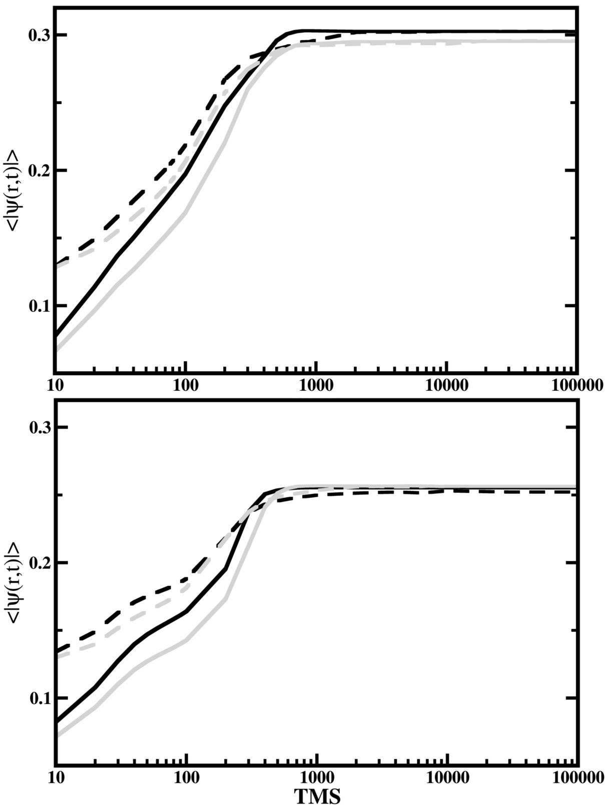

Figure 3.3: *Time evolution of the average order parameter. Top: hard walls confinement, bottom: soft walls confinements. Black lines: boxes accommodating* 3×3 *cylinders, gray lines: boxes accommodating* 4×4 *cylinders. Solid lines: initial noise* ± 0.05, *dashed lines: initial noise* ± 0.5

different from the hard wall case, (Figure 3.1b) which indicates weaker influences of soft walls on the structure formation compare to the hard walls case. Figure 3.3 provides detailed view on the kinetics of the macrophase separation in the above systems. For both hard and soft walls confinement we find that the microphase separation proceeds faster in smaller boxes (compare the gray and black lines in Figure 3.3). We also observe that the noise speeds up the microphase separation at the initial stages in both types of confinement while at the latest stages, when the structures are well developed, the stronger noise slightly suppresses the microphase separation (compare lines of the same shades of gray). At the end microphase separation reaches the same level for the systems of the same size regardless the noise level.

3.2.1.3 Confinement in larger squares

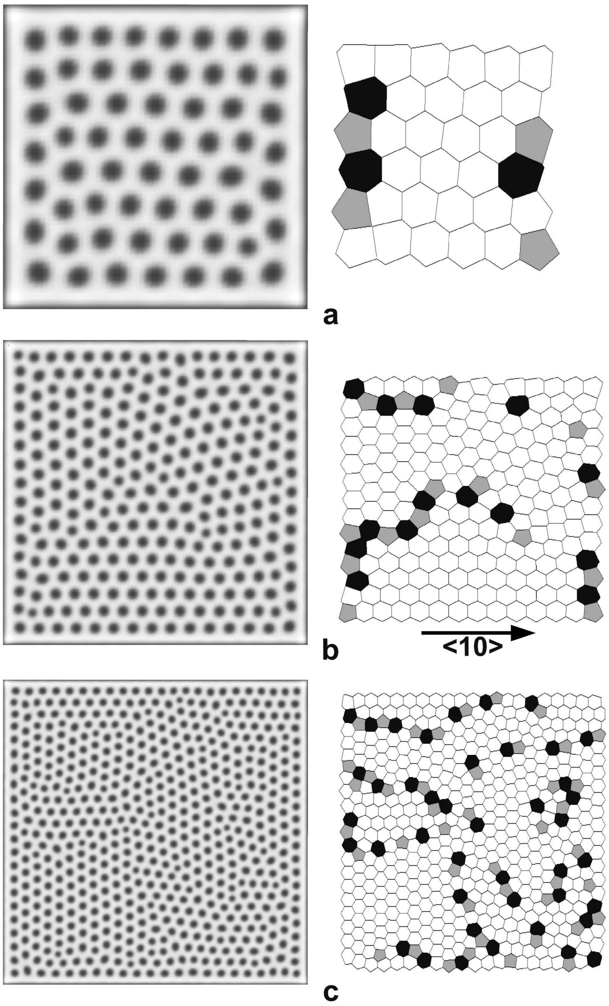

Figure 3.4: *BCP confined by hard walls: top view on 3D CDS simulations after* 10^6 *time steps (left) and corresponding Voronoi diagrams (right). Black and gray polygons depict 7-5 neighbors defects. The initial noise level is* $\psi_0 = \pm 0.5$, *the square sides are* $L_x = L_z = 64 \sim 9L_0$ *(a),* $L_x = L_z = 124 \sim 17L_0$ *(b),* $L_x = L_z = 182 \sim 25L_0$ *(c) and* $L_y = 5$ *grid points in all cases.*

Here we perform simulations in square boxes of the same size as the experimental samples shown in the Figure 3 of Ref.[53]. Figure 3.4 shows the final configurations after 10^6 time steps. In these larger boxes the influence of the boundary becomes smaller compared to the case in Figure 3.1: the cylinders are predominantly packed in hexagonal arrays, the natural bulk morphology.

Typical defects in the packing are 5 and 7 neighbors, which usually occur in pairs and form grain boundaries. The relative number of defects (the ratio of the defects number to the total number of cylinders) is almost the same for the modest box sizes $\sim 9L_0$ and $17L_0$: 11.86% and 11.32% respectively. However for the large box sizes $\sim 25L_0$ the relative influence of walls decreases which manifests a slightly increase in defect fraction: 14.93%. As the defects tend to cluster either in pairs or in short lanes of 2-3 pairs (see Voronoi diagrams in Figure 3.4), the total number of grains increases with the box size, which is in qualitative agreement with the experiments, Tab. 1 in Ref.[53]. Similarly to the experimental findings, we observe that the hexagonal lattice orientation has its (10) direction parallel to the pattern edges, whereas randomly oriented grains are observed in the centre of the pattern, Figures 3.4b,c.

3.2.1.4 Analysis of the square packing

To quantify the occurrence of square packing as a function of pattern size, we measured the centre-to-centre distances between the microdomains in patterns sized from $\sim 2L_0$ to $9L_0$. In Figure 3.5, for a pattern size $\sim 9L_0$, the distance histogram has a Gaussian shape with a main peak at $\sim L_0$ corresponding to the natural BCP period. A very small secondary peak at $1.3L_0$ is observed representing about 3.2% of the microdomain population. This distance is associated with the presence of defects caused by the confinement induced by the square pattern. In the experimental histogram these three values are $1.1L_0$, $1.3L_0$ and 3.0% respectively,[53] in a very good agreement with our simulations. Structures in the larger boxes are therefore dominated by the natural bulk morphology. In the opposite case of very small squares, $\sim 2L_0$, the situation is different, Figure 3.5c. The main peak at $0.9L_0$ corresponds to (10) spacing of the square lattice whereas the secondary peak at $1.4L_0$ corresponds to the (11) spacing of the square lattice ($1.4/0.9 \approx 1.5$, while for a perfect square the ratio should be $\sqrt{2} \approx 1.4$). Experimentally these numbers are $1.0L_0$, $1.4L_0$ ($1.4/1.0 \approx 1.4$) correspondingly. The secondary peak area is 17.2% in our simulations, again in a very good agreement with the experiments (17.8%).[53] For a perfect square the secondary peak area should be 33% (see Figure 3.7a); the deviation from this number indicates the presence of defects as can be seen in Figure 3.6a. While the larger boxes are dominated by the bulk structure and very small boxes are dominated by the walls, the most interesting situation is observed for the intermediate sizes, $\sim 3L_0$, where both effects clearly compete. Figure 3.5b shows the histogram for the solid wall squares of size $\sim 3L_0$. The main peak is

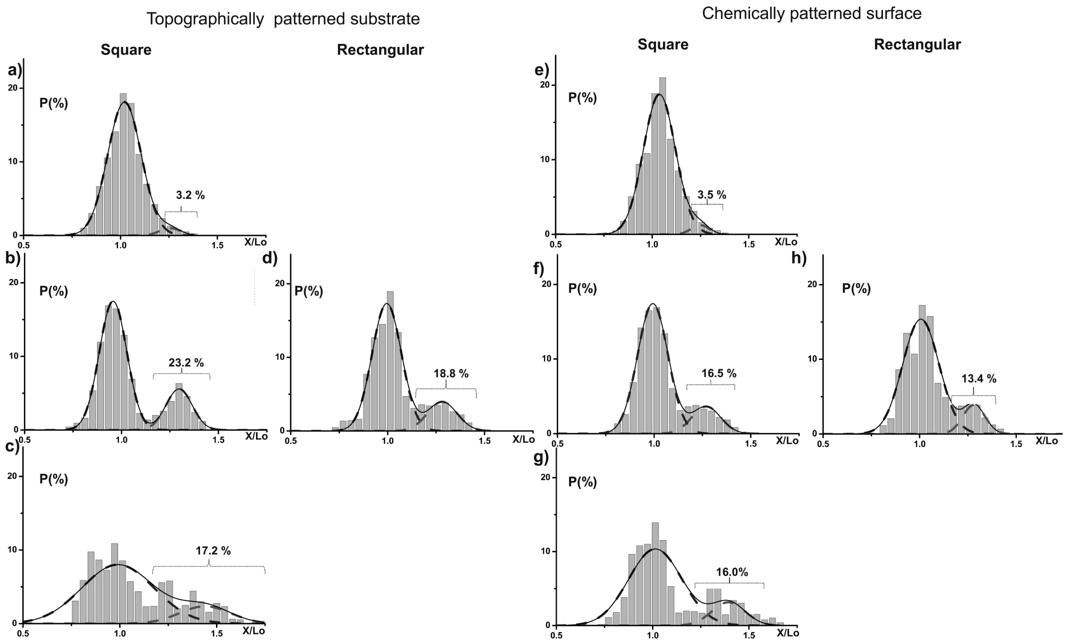

Figure 3.5: *BCP cylinder nearest-neighbor distance distribution for* $\sim 9L_0$ *(top row),* $\sim 3L_0$ *(middle row),* $\sim 2L_0$ *(bottom row) square (first and third columns) and rectangular (second and fourth columns) confinements. (a-d): hard wall confinement, (e-h): soft wall confinement. All histograms are averages over a large number of individual patterns with initial noise level* $\psi_0 = \pm 1$ *and slightly different side sizes. (a): 216 square samples with side sizes in the range* $64 \div 70$ *grid points; (b): 288 square samples with side sizes in the range* $27 \div 31$ *grid points; (c): 432 square samples with side sizes in the range* $20 \div 25$ *grid points; (d): 288 rectangular samples with side sizes in the range* $28 \div 31$ *grid points; (e): 216 square samples with side sizes in the range* $62 \div 67$ *grid points; (f): 288 square samples with side sizes in the range* $25 \div 29$ *grid points; (g): 432 square samples with side sizes in the range* $18 \div 22$ *grid points; (h): 288 rectangular samples with side sizes in the range* $25 \div 30$ *grid points.*

observed at $0.9L_0$ and the secondary peak at $1.3L_0$, with the ratio of the two peak positions ($1.3/0.9 \approx 1.4$) being close to $\sqrt{2} \approx 1.4$, Experimentally these numbers are $1.14L_0$, $1.4L_0$ with the ratio $1.4/1.14 \approx 1.2$. However, the area of the secondary peak is rather different: 23.2% (simulations, Figure, 3.5b) versus $\sim 9.1\%$ (experiments).[53] For a perfect square of 3×3 cylinders the secondary peak occurrence should be 40% (Figure 3.7b). Therefore, the simulated patterns are more "square" compared to the experimental ones. Figure 3.6b shows some of the simulation samples $\sim 3L_0$ with typical defects in the packing. To clarify the discrepancy obtained in the case of Figure 3.5b with the experimental case,[53] we simulated boxes which slightly deviate from square (rectangles with $1 \div 2$ grid points difference between the sides). The results shown in Figure 3.5d indeed confirm that the secondary peak decreases in area till 18.8%. The position of the peaks and their ratio are: $1L_0$, $1.3L_0$, 1.3, correspondingly, similar to the case of the square pattern in Figure 3.5b.

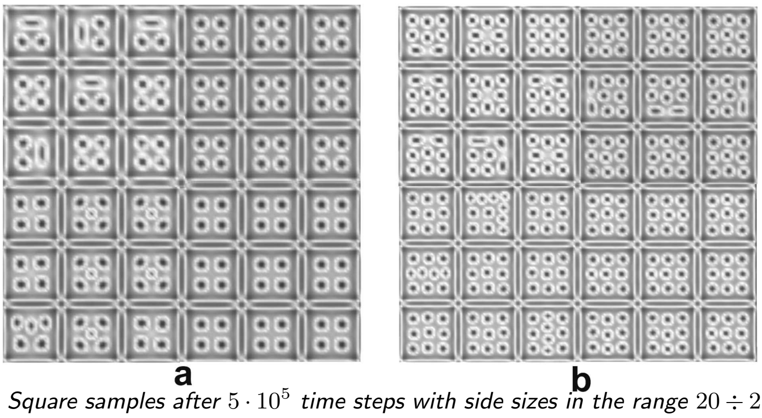

Figure 3.6: *Square samples after* $5 \cdot 10^5$ *time steps with side sizes in the range* $20 \div 25$ *grid points (a) and* $27 \div 31$ *grid points (b). Initial noise* ± 1.

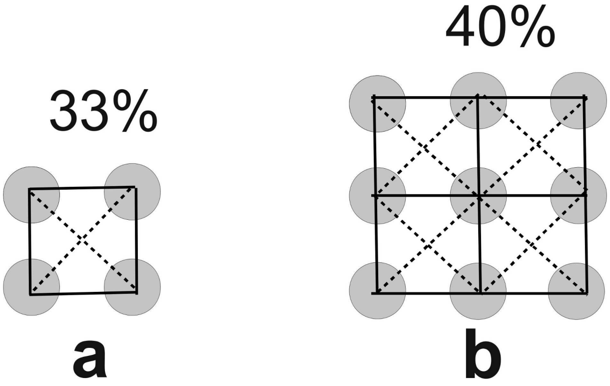

Figure 3.7: *Schematic representation of* 2×2 *(a) and* 3×3 *(b) square lattices of cylinders. Solid lines are (10) planes and dashed lines are (11) planes of the square lattice. Percentages are the ratio of nearest neighbors connections along the dashed lines to the total number of nearest neighbor connections.*

We performed a similar analysis for the soft walls confinement. For the case of the box size $\sim 9L_0$ the main peak is at $1.0L_0$, the secondary peak at $1.3L_0$, which represents 3.5% of the microdomains population, which confirms, that the packing is mostly hexagonal with some defects due to the square boundary. In the case of the box size $\sim 3L_0$ the main and the secondary peaks are at $0.9L_0$ and $1.3L_0$ respectively and their positions ratio is 1.4. Soft walls have an effect of reducing the secondary peak occurrence even in perfect squares, Figure 3.5f. The area of the secondary peak is 16.5%, almost exactly the same as in the case of slight rectangles with solid walls (compare Figures 3.5d and f). If we take into account a deviation from the square shape, the area of the peak can be reduced even further till 13.4%, Figure 3.5h, which is closer to the 9.1% in the experiments of Ref.[53]. In this case, the position of the peaks and their ratio are: $1L_0$, $1.3L_0$, 1.3. The soft wall confinement with size $\sim 2L_0$

has a main peak at $1.0L_0$, and a secondary peak at $1.4L_0$, which represents 16.0% of the microdomain population, Figure 3.5g, a bit less compared to the case of the hard walls, Figure 3.5c. Our results confirm, that there is a difference between hard and soft wall walls confinement, and that the experimental situation in Ref.[53] is better modelled by a chemical patterning on a substrate (soft walls) taking into account small imperfections in square shapes. The difference between chemical and topographical patterns would not be possible to observe in 2D simulations,[4] as it is an intrinsically 3D phenomenon. Indeed, the fabrication method in Ref.[53] was chemical patterning and the pattern sizes had an error bar of $\pm 5nm$ ($0.2L_0$), which corresponds to $1 \div 2$ grid points in our simulations and makes our assumption of deviation of squares into rectangles plausible.

3.2.1.5 Diamond-shape confinement

Here we perform simulations in diamond-shape hard walls confinements, which can comfortably accommodate hexagonal lattice, Figure 3.8. Such a pattern has been recently fabricated experimentally, see Figure 3 in Ref.[61].

In the small to medium box sizes the defect density is very small: 0 (Figure 3.8a,b), 3% (Figure 3.8c). Our results show that defects are sensitive to the frustrations in the lattice caused by the confinement, as a small change in the box size can either heal or favour defects survival (compare Figures 3.8c,b). As the box size increases so does the number of defects: $\sim 16.73\%$ and $\sim 14.59\%$ for the boxes $\sim 17L_0$ and $\sim 25L_0$ in Figure 3.8d,e, indicating that at these sizes the defect density is dominated by the bulk behaviour rather than by the walls. The time evolution of the BCP structure for the box from the Figure 3.8a is shown in the Figure 3.9 for two values of the initial noise level $\psi_0 = \pm 0.5$, and $\psi_0 = \pm 0.05$.

Similar to the case of square confinement the microphase separation starts everywhere in the sample in the case of stronger noise, Figure 3.9a, and it is induced by the presence of the walls in the case of the weaker noise, Figure 3.9b. We find that the noise can facilitate defects annihilation: the final configuration is a perfect hexagonal packing for the stronger noise while for the weaker noise the system remains trapped in a defected state even if the simulation is performed for a very long time, (compare Figure 3.9a and b, bottom). We compare the time evolution of the defect density in

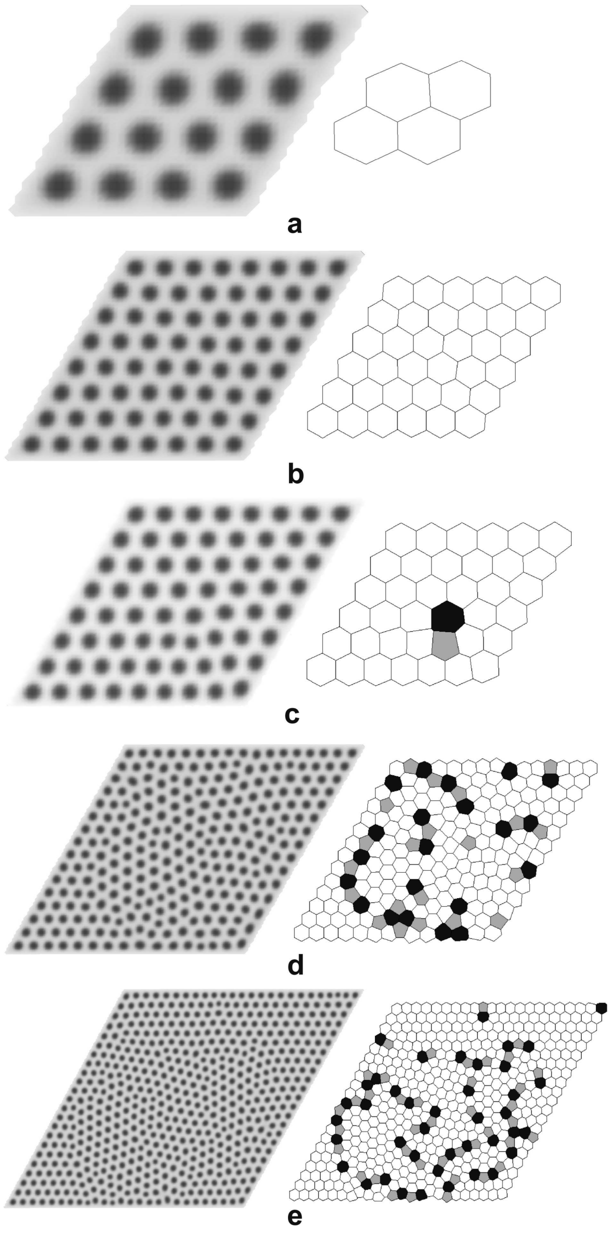

Figure 3.8: *Top view on the 3D CDS hard wall confinements of different side lengths (left) and their Voronoi diagrams (right):* $35 \times 5 \times 35$ *grid points* $\sim 4.7L_0$ *(a),* $65 \times 5 \times 65$ *grid points* $\sim 8.8L_0$ *(b),* $66 \times 5 \times 66$ *grid points* $\sim 8.8L_0$ *(c),* $126 \times 5 \times 126$ *grid points* $\sim 17L_0$ *(d),* $185 \times 5 \times 185$ *grid points* $\sim 25L_0$ *(e). Each snapshot is taken after* 10^5 *time steps. Initial noise level is* ± 0.5

larger boxes $\sim 17L_0$ for diamond and square hard wall confinement, Figure 3.10.

The defect density for the diamond pattern is $\sim 31.8\%$ (a), $\sim 20.54\%$ (b), $\sim 17.89\%$ (c), whereas for the square pattern at the same times it is: $\sim 34\%$ (d), $\sim 18.67\%$ (e), $\sim 13.67\%$ (f), which are not significantly different in both cases confirming that in the larger boxes the defects kinetics is dominated by the bulk behaviour.

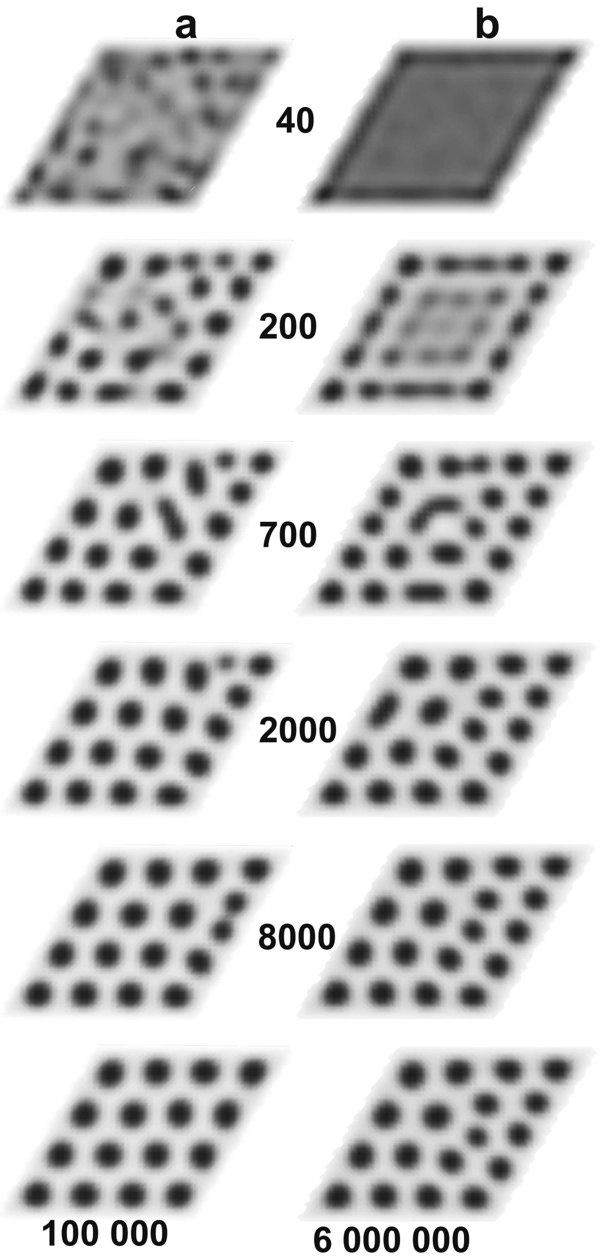

Figure 3.9: *Top view on 3D of diamond confinements. Time evolution of an AB diblock copolymer within diamond-like hard walls of side length* $\sim 4.7L_0$*. Initial noise level* $\psi_0 = \pm 0.5$ *(a), and* $\psi_0 = \pm 0.05$ *(b).*

3.2.1.6 Rectangular hard wall confinement

Figure 3.11 shows the morphology of microdomains confined in topographical rectangular patterns. We find that for all the rectangles of every aspect ratio the hexagonal packing favours orientation with (10) direction along the longer side. As a result, the cylinders along the longer side form nice straight rows whereas alignment along the short side of the rectangles has 'zig-zag' style and has therefore more defects. In the

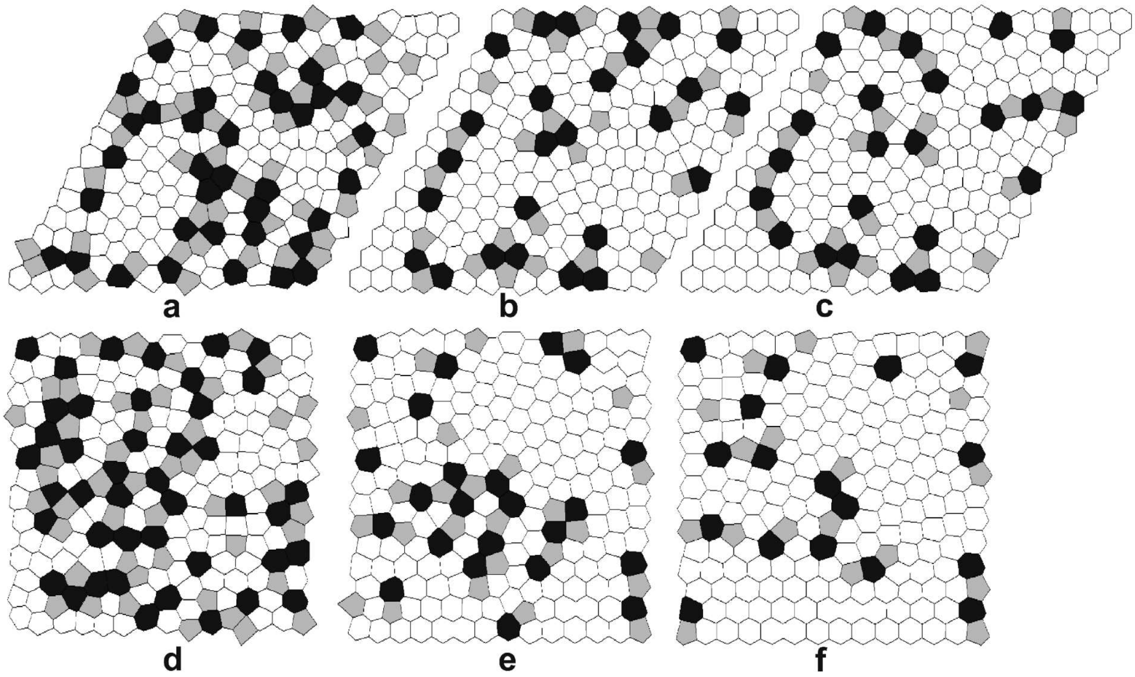

Figure 3.10: *Time evolution of Voronoi diagrams for square and diamond hard wall confinements. Top view on 3D CDS boxes with the size length of* $L_x = 126$*,* $L_y = 5$ $L_z = 126$ *grid points* $a \div c$*, and* $L_x = 124$*,* $L_y = 5$ *and* $L_z = 124$ *grid points* $d \div f$*. Time steps (TMS):* 10^3 *(left column),* 10^4 *(middle column),* $3 \cdot 10^4$ *(right column).*

experiments of Ref.[53], one can observe the same orientation of the hexagons in their Figure 4 (although is not explicitly emphasize in the text). The Ref.[53] suggests a kinetic mechanism for the higher defect density along the short rectangle side: the pattern growth is nucleated by the edges and the grains originated from the longer sides merge faster into a single grain. To verify this mechanism we performed two simulations with different initial noise which in one case the pattern growth is nucleated by the edges while in another case the nucleation occurs everywhere in the sample, Figure 3.12. In both cases the final morphology is the same, with (10) direction of the hexagons being along the longer side. They confirm that the difference between the longer and shorter sides alignment is not caused by kinetics but is a pure geometrical phenomenon of more 'comfortable' fitting of hexagons into the rectangles.

3.3 Conclusion

The present chapter provides a 3D computer simulation of block copolymers standing up cylinders in two different type of confinements: topographical and chemical pat-

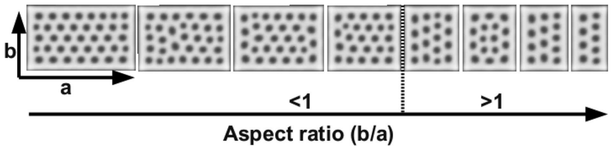

Figure 3.11: *Top view on 3D CDS of hard walls confinement of rectangular cross-section for different aspect ratios. Size from left to right:* $a = L_x = 66$, 56, 55, 45, 34, 33, 30, 29 *grid points,* $b = L_z = 40$ *and* $L_y = 5$ *grid points. Initial noise is* $\psi_0 = \pm 0.5$. *Each simulation was performed for* 10^6 *time steps.*

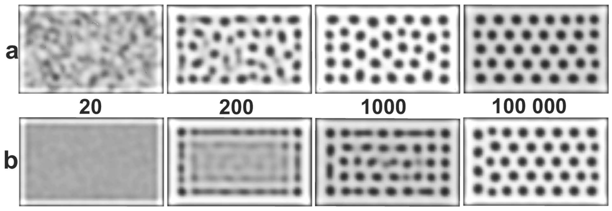

Figure 3.12: *Top view in 3D CDS in rectangular hard walls confinement for different timesteps (TMS) and noise levels:* $\psi_0 = \pm 0.5$ *(a),* $\psi_0 = \pm 0.05$ *(b). Size* $L_x = 66$, $L_y = 5$ *and* $L_z = 40$ *grid points*

terns. The necessity of such analysis was first suggested in two dimensional study, Ref.[4] albeit for a different computational method (SCFT). In the present work we employed cell dynamics simulation which allowed a 3 dimensional study of boxes of different sizes. The paper provides computational explanation of recent experimental results in a square confinement.[53] We find for the square wells of small sizes that the structure is dominated by the walls inducing 2 × 2 square lattice of cylinders while in the large boxes the structure is dominated by the bulk hexagonal morphology. For the intermediate sizes where boundary and bulk effects compete we find a different effect of the topographical confinement and the chemical pattern confinement: topographical confinement has a stronger influence and can induce better structures of 3 × 3 square lattice cylinders. For the square confinement compatible with 4 × 4 square lattice of 16 cylinders the tetragonal phase is found to be a transient structure leading towards a twisted hexagonal morphology in agreement with 2D SCFT results.[4] We also investigate the role of size imperfections such as a slightly deviations from square wells and found that it has an effect at intermediate sizes (3 × 3 square lattice of cylinders). We also perform simulations in rectangular boxes and found orientation of the hexagonal lattice with its (10) direction parallel to the long size in agreement with the experiment,[53] although our results suggest an alternative explanation due to more favorable fitting of hexagons into a rectangle. We also performed simulations in a diamond lattice which can naturally accommodate hexagonal lattice.

Chapter 4

Block Copolymer Cylinder-Forming Thin Films under Shear Flow

Synopsis

In this chapter computer simulation are reported on cylinder-forming diblock copolymer in thin films and under a simple steady shear flow. Using Cell Dynamics Simulation, the effect of different intensity of the surface field and different film thickness is investigated. Different morphologies have been observed, i.e. wetting layer, parallel cylinders, perpendicular cylinders, perforated lamellae, parallel lamellae, coexistence of perpendicular and parallel cylinders, and coexistence of parallel cylinders and perforated lamellae, etc. Upon application of a simple steady shear flow to perpendicular cylinders or perforated lamellae, the morphologies improve their hexagonal packing, while parallel cylinders align perfectly in the shear direction. Increasing the shear rate above a threshold value induces transition from perpendicular into the parallel cylinders, and from perforated lamellae to lamellae, or parallel cylinders depending on the film thickness.

4.1 Introduction

The orientation of the microdomains in block copolymer thin films is very important in nanolithography in order to generate nano-pattern.[80] The phase behaviour of the block copolymer (BCP) self-assembly in thin films is different from the bulk, due to the interfacial interaction (with substrate and/or free surface) of block components, i.e., the energetic preference of the substrate or the free surface for one of the two blocks and confined geometry. These consequences are emphasized with decreasing of the film thickness.[81] Symmetric diblock copolymers in confined thin film, as a function of the interaction with the substrate, can generated lamellae alignment parallel or perpendicular to the film.[82–86] A sphere forming diblock copolymers show a packing transition as a function of the film thickness. In the bulk a body-centered (bcc) packing has been observed, in a monolayer a hexagonal packing has instead been found.[87] Cylinder-forming diblock copolymers have a more complicated phase behaviour.[88–93] Different morphologies have been observed, i.e.: wetting layer, lamellae, perforated lamellae, cylinders with necks.[94] However, for their self-assembly nature, the lateral long range ordering of the nanodomains is very complicated to achieve. A manipulation by an external field, such as electric field[95] or shear flow[96], can be used.

Using Monte Carlo simulation Arya et al.[97] studied the behaviour of the self-assembling cylinder forming diblock copolymer under shear flow. They applied shear flow to a prealigned system in a direction perpendicular to the original alignment of the cylindrical system. They observed that the cylinders align rapidly with shear direction through a mechanism where the cylinders perpendicular to the shearing direction (but parallel to the thin film plane) break up into smaller aggregates. These smaller aggregates align and grow in the direction of shear via their recombination. They also observed that thicker films give rise to multi-layered cylinders aligned perfectly parallel to the shearing direction, with hexagonal packing in the plane perpendicular to the shear direction.[97]

Register and coworkers[98] were the pioneers of the experimental study of shearing a single-layer of cylindrical microdomains block copolymers. They obtained long range order of cylindrical microdomains parallel to the shear direction. Their findings were also further confirmed by their two-dimensional computational work, by using Cell Dynamics Simulation.[98]

Ly et al.[99] by using self-consistent-field simulation investigated a perforated lamellae, obtained by confining a cylinder forming diblock copolymer in a thin film with thickness of one bulk interdomain spacing. Upon application of an electric field, the perforated lamellae transforms to laying or standing cylinders depending on the direction of the electric field.[99]

Hongo et al.[100] demonstrated that shear can induce a sphere-to-cylinder (aligned in plane) transition for a sphere-forming polystyrene-polyisoprene diblock copolymer single and bilayer films. This result was subsequently confirmed from computational work by Pinna et al.[72]

Chremos et al.[94], by using a coarse grained Langevin dynamics simulations, studied the behaviour of thin films of diblock copolymers as a function of composition, segregation strength, and the strength of the shear field, keeping the film's thickness and the strength of the wall-film interaction fixed. The phase diagram as function of the segregation strength and the composition under shear flow give rise to several morphologies: cylinders parallel to the direction of the flow; cylinders perpendicular to the direction of the flow; mixture of spheres and cylinders parallel to the direction of the flow; mixture of the spheres and cylinders perpendicular to the direction of the flow. Their simulations confirmed that sphere-forming films exhibit a shear induced transformation to cylinders parallel to the sheared direction. They also found that at higher segregation strengths, the cylinders formed by symmetric and near symmetric diblock copolymers chains experience a transition from parallel to perpendicular orientation to the shear direction.[94]

Pinna et al.[72], by using Cell Dynamics simulations, studied sphere-forming diblock copolymer under shear. They obtained several phase behaviour by changing the temperature and the shear rate. In two layer films the spheres align in various arrangements: multiple and mono-cluster square packing; multiple and mono-cluster hexagonal packing; cylinders perpendicular to the shear direction; transition from spheres to cylinders (observed also in Ref.[100]); coexistence of elongated spheres and short cylinders (observed also in Ref.[94]); defected hexagonal packing with short parallel and perpendicular cylinders; and disordered spheres with randomly oriented short cylinders. In a single layer of spheres they found spheres that can transform to cylinders (like in the case of two layer system), transition from spheres into ellipsoids which occasionally merge into short cylinders, disordered spheres and hexagonal packing of sphere (similar to the two layer system), and mono-cluster of hexagonally packed ellipsoids.

Using coarse-grained Langevin dynamics simulations Chremos et al.[101] investigated the shear alignment of lamellae-forming diblock copolymers in thin films as a function of the shear rate, the interactions between polymer segments and the confining surfaces. For neutral confining surface they found that, above a critical stress, lamellae melt and reform in the direction of the shear (perpendicular to the walls). When the confining surfaces becomes non-neutral, then the block favored by the non-neutral surface creates a wetting layer, while the film at the neutral surface remains unaffected (the lamellar structure remains perpendicular). If both surfaces become non-neutral, then they found parallel lamellae.[101]

Recently, Kim et al.[102] demonstrated experimentally that square, rectangular, and rhombic arrays can be created via shear-alignment of distinct layers of cylinder-forming polystyrene-poly(ferrocenylisopropylmethylsilane), PS-PFiPMS, diblock copolymer.[102]

Nikoubashman et al.[103] studied experimentally thin films of homopolymer (poly (styrene)) and a monolayer of cylinder-forming diblock copolymers (poly(styrene)-b-poly(n-hexyl methacrylate)) under shear. They observed that the shear induced long range order.

Davis et al.[104] experimentally studied thin films of cylinder-forming polystyrene-poly(n-hexyl methacry-late) diblock copolymers. They investigated the thin-film structure as a function of film thickness and the composition of block copolymers with and without shear. Without shear the cylinders change from perpendicular to parallel to the thin film plane as the thickness increases. With shear, it is possible to observe the highest quality of alignment when the composition of the diblock copolymer is a middle value.[104]

In this Chapter, the Cell Dynamics Simulation (CDS) is applied to study thin films of perforated lamellae, lying-down cylinders and standing-up cylinders on the substrate under a simple steady shear. Thin films of perforated lamellae, standing-up cylinders, and lying-down cylinders are important from technological point of view in order to create, respectively, ordered nanoporous polymer films[105], pattern mask or nanoporous membrane[106], and striped patterns which could serve as precursors to arrays of metal nanowires.[107] The current analysis has been performed by using a coarse graining technique, CDS, because the goal is to study how the morphology transforms in time under an applied shear flow. CDS is a relatively fast method (see review[25] for a comparative estimate of CDS and DDFT runtimes) and has a good record of describing rather complex experimental phenomena in BCPs.[25,28] Therefore, CDS is an adequate methodology to perform large-scale simulations which are useful when the purpose is to observe the morphology transition. In this study an asymmetric AB-diblock copolymer confined between two parallel walls has been investigated as a function of the film thickness and the strength of the wall homogeneous film interaction. Several morphologies have been observed. Subsequently, it has been studied the effect of a steady shear flow on perforated lamellae, lying-down cylinders, and standing-up cylinders, previous obtained, with film thickness ranging from $\sim L_0$ to $\sim 3L_0$. Upon application of shear flow, an improvement of the hexagonal packing in both perforated lamellae and standing-up cylinders thin film has been found. Phase transition has been observed only when the shear field is stronger than a certain critical value.

4.2 Results and discussion

4.2.1 Model system

The system of interest is a cylinder-forming of AB-diblock copolymers (BCPs) 1-dimensional (1D) confined between two parallel homogeneous selective surfaces. Figure 4.1 shows the schematic illustration of 1D confinement box. The other parameters entering in Eq. 2.2 are $A = 1.5$, $B = 0.02$, $D = 0.5$, $v = 1.5$, $u = 0.5$, $\tau = 0.3$, $f = 0.4$, as has been used in earlier works on BCP cylinders confined within spherical enclosure or cylindrical pores.[43,79] The bulk period of cylinder-forming diblock copolymer ordered structure is $L_0 \sim 7.4$.[108] Under different surface fields h, see eq.(2.12), the self-assembled structures are obtained as a function of the confinement dimension L_y. The results are summarized in Figure 4.2, for boxes dimension $L_x = L_z = 128$ grid points. The dark regions correspond to the minority block-phase. The slit surfaces were represented as planes with a thickness of 1 grid point and positioned parallel to the $x - z$ planes of the box. Periodic boundary condition are applied in the $x-$ and $z-$ direction.

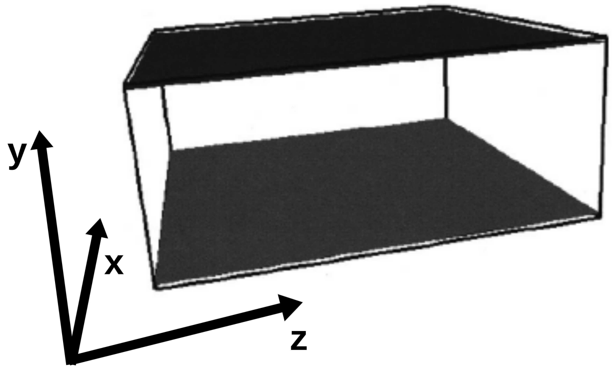

Figure 4.1: *The simulation box for thin films. The dark faces, placed at the top and bottom of the box, in* y *direction, are the homogeneous selective surfaces. Periodic boundary conditions are applied in the other two directions.*

In this section, the results in Figure 4.2 are presented for three typical cases in which the surface is neutral to both A (minority component) and B (majority component) blocks ($h = 0$), selective to A but repulsive to B ($h > 0$), and selective to B but repulsive to A ($h < 0$). Four more types of confinement surfaces attraction are considered for the case of A- or B-attractive surface, wherein the confinement surface strength varies from weak to strong, $0.1 \leq h \leq 0.6$ and $-0.1 \leq h \leq -0.6$, respectively. Fascinating morphologies have been observed. However, to tailor a desired structure, a manipulation by external field can be used. In this work, the attention has been focused on the study of the application of a steady shear flow, see eq. 2.11, on some of the morphologies induced by the presence of surfaces in a diblock copolymer melt for certain separation distances L_y between the surfaces and the strengths h of surface-polymer interaction. The morphology of interest under shear flow in this chapter are: monolayer layer of perpendicular cylinders found at $h = 0$ and $L_y = 6$; monolayer layer of perforated lamellae obtained at $h = -0.1$ and $L_y = 8$; monolayer layer of parallel cylinders at $-0.4 \leq h \leq -0.2$ and $L_y = 10$; double layer of perforate lamellae found at $h = -0.1$ and 14, and at $h = -0.2$ and 16; double layer of perforate lamellae at $h = -0.6$ and $L_y = 10$; double layer of coexistence of parallel cylinders and perforated lamellae at $h = -0.1$ and $L_y = 12$; double layer of coexistence of perforated lamellae and lamellae at $h = -0.2$ and $L_y = 14$; a layer of perpendicular cylinders surrounded between two layers of perforated lamellae at $h = -0.2$ and $L_y = 18$; and coexistence of perpendicular and parallel cylinders obtained at $h = 0$ and $8 \leq L_y \leq 20$. All simulations were started from an initial random disordered state (ψ was a random number within the range ± 1), with $\Delta t = 1$. Unsheared structures have been simulated for 1 000 000 time steps; and sheared structures have been simulated for 5 000 000 time steps. Since our Cell Dynamics methods do not contain the information about the small-scale chain dynamics that would be necessary to model transient flow effects, we focus on the case of steady shear.

4.2.2 Morphologies in a slit

Figure 4.2 exhibits the structures which summarizes the results that have been obtained for cylinder-forming AB-diblock copolymers confined within 1D confinement cavity as a function of the surface field h and the confinement dimension L_y, with square sizes $L_z = L_x = 128$. Simulations with square size $L_z = L_x = 512$ have also been performed, and it has been found that the size cannot affect the resulting morphologies. Most of the pictures, which represent the morphologies indicated in the structure diagram, are depicted in Figure 4.2. For the description of simple structures the following notation has been used, in agreement with Lyakhova et al.'s computational work[89]: $C_\perp$ perpendicular cylinders to the surface; $C_{||}$ parallel cylinders to the surface; W wetting layer; L lamellae; PL perforated lamellae. A comma (,) describes two equal layers of A-structure, for instance, $PL,_2$. For the description of hybrid structure the following notation has been used: two or more A-rich layers separated by one or more B-rich layers are denoted by a hyphen (-) between the corresponding A structures, for instance, $PL - C_\perp - PL$; lateral coexistence of A-structures in one horizontal layer is denoted by a slash (/), for instance, $C_\perp/C_{||}$; in case one of these structures form more than one layer we use a comma (,), for instance, $C_{||,2}/C_\perp$; but in case of two equal layer with lateral coexistence of A-structures in one horizontal layer the brackets () have been used, for instance, $(PL/L),_2$; no separating symbol is used for connected structures, for instance, $C_\perp\ C_{||}$, which denotes cylinders with necks. All these morphologies are embedded in a B-rich matrix.

In Figure 4.3 it has been depicted the full structure of two layers of the coexistence of parallel cylinders and perforated lamellae with size $L_z = L_x = 512$, $L_y = 16$, and h=-0.1.

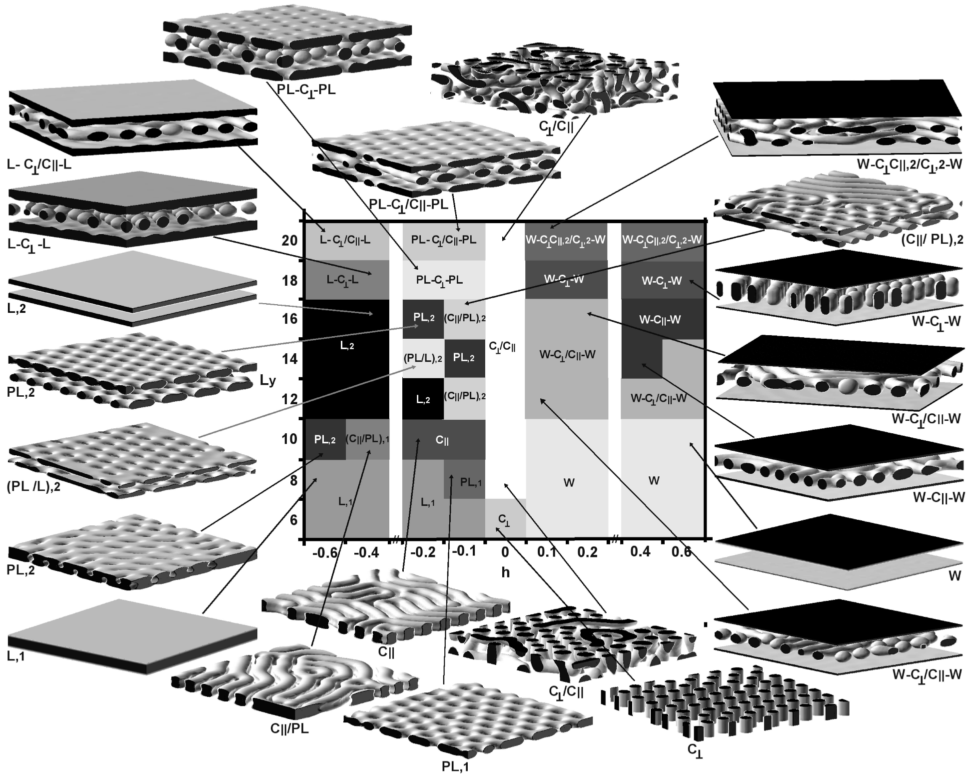

Figure 4.2: *Structure diagram of cylinder-forming diblock copolymer under different surface fields (h) as a function of the film thickness L_y, and $L_z = L_x = 128$. $C_\perp$ (perpendicular cylinders); $C_{||}$ (parallel cylinders); W (wetting layer); L (lamellae), PL (perforated lamellae). Morphologies are shown as crops, of $L_z = L_x = 64$, of larger simulation boxes.*

4.2.2.1 Neutral surface ($h = 0$).

In this case the neutral surface is equally selective for either of the two blocks of the copolymers. Typical morphologies obtained at $h = 0$ are shown in Figure 4.2. When the confinement space $L_y = 6$ is smaller than one period polymer $L_0 \sim 7.4$ it has been found A-blocks forming a single layer of cylinders perpendicular, $C_\perp$, to the plane xz. In this case the width of the cylinder in the vicinity of the walls and in the middle of the cylinder is the same. This is because at $h = 0$ the A- or B-component are equally selected from the surfaces. In Huinink's study, they also found a stable perpendicular cylindrical phase when neither the A nor B block preferentially wets the surfaces and when the slit width is around one polymer period, Table 1 at surface interaction $\xi = 0$ and slit width $L_y = 8$ (their original notation is $H = 8$ grid points).[90] With the confined space volume increasing to $L_y = 8$ the morphology drastically changes. In fact, a coexistence

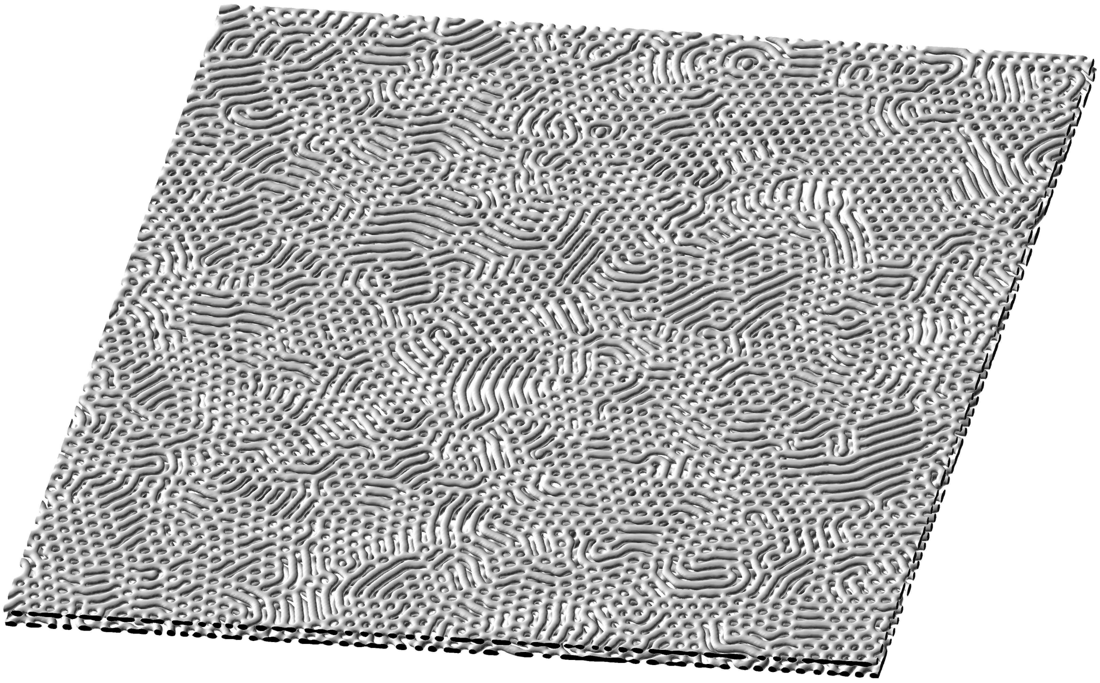

Figure 4.3: *Morphology of $(C_{||}/PL)_2$ at $L_z = L_x = 512$ and $L_y = 16$, and h=-0.1.*

of parallel $C_{||}$ and perpendicular $C_{\perp}$ cylinders, respect to the $xz-$plane, are adjusted to fit the confined space volume. The coexistence of parallel and perpendicular cylinders dominates the structure diagram at larger values of the confinement $10 \leq L_y \leq 20$. As seen, at $h = 0$ the phase behaviour is very simple. The picture at $L_y = 20$ shows the random distribution of long and short cylinders (sometimes half cylinder) due to the confinement frustration.

4.2.2.2 Minority block selective surface ($h > 0$).

When the confinement surface attracts minority-blocks (A-block) $h > 0$, a totally different behaviour compare to that observed in the neutral surface cases is obtained. At first sight, Figure 4.2 shows complex phase behaviour of multilayer structures at $h > 0$. In fact, when the film surfaces are preferentially wet by the A-blocks, but even B-blocks as it is possible to see in the structure diagram $h < 0$, parallel oriented microdomains are preferred near to the slit surfaces located at the top and bottom faces of the simulation box. In the case of weaker surface field $h = 0.1$ and small confinement $L_y = 6$ it is found a morphology called wetting layers, W, which is a structure complementary to the microdomain structure next to it in the middle of the film. W structure aligns parallel with the film because a difference between the surface energies of the two blocks exists (selective surfaces). The picture of W phase behaviour, Figure 4.2, makes clear that at $h = 0.1$ and $L_y = 6$ A-enriched layers are formed at the slit surfaces. When the confinement increases $8 \leq L_y \leq 10$ the resulting phase behaviour is still a W. At $L_y = 12$ the morphology becomes more complicated, it is found a coexistence of parallel cylinders $C_{||}$ and perpendicular cylinders $C_{\perp}$ forming one layer confined between two W. The $C_{\perp}$ has a pill-shape, Figure 4.2. As the thickness increases $L_y = 18$ the $C_{\perp}$ has an elongated shape, Figure 4.2, and top and bottom of the cylinder is not truncated like the $C_{\perp}$ found at $h = 0$ and $L_y = 6$. The different shape is due to the presence of the W at $L_y = 12$ and $L_y = 20$. At larger confinement space $L_y = 20$ the structure diagram exhibits a more elaborated phase behaviour. Two layers of parallel cylinders with necks (protuberance which is perpendicular and attached to the final part of the parallel cylinder) coexisting with perpendicular cylinders placed in both layers are observed. These two A-rich layers are surrounded by W. In this case the perpendicular cylinder is similar to a pill, and its shape differs from the others observed at $L_y = 6$ and $h = 0$. When the surface field increases the phase behaviour is pretty similar. The only new morphology that appear is a layer of parallel cylinders $C_{||}$, which have random direction, surrounded by two W layers, for $L_y = 16$ $0.2 \leq h \leq 0.4$, and $L_y = 14$ $h = 0.4$.

4.2.2.3 Majority block selective surface ($h < 0$).

When the confinement surface attract majority-block (B-block), $h < 0$, it has been obtained a different behaviour from that observed in the case of neutral surface $h = 0$ and in the case of A-attractive surface field, $h > 0$, Figure 4.2. Also the B-attractive surface case exhibits the influence of the confinement on the structures. As shown in the column at $h = -0.1$ of Figure 4.2, the self-assembled structures for this case are very different. It is noted that when the confinement value $L_y = 6$ is less then one polymer period L_0 the structure is a single layer of lamellae L. By increasing the confinement value $L_y = 8$ around one polymer period the morphology changes in one layer of perforated lamellae PL. A different phase behaviour is present at $L_y = 10$, parallel cylinders $C_{||}$ with a random orientation. It is possible to note that in the B-attractive surface case the structures are not surrounded by the wetting layers, as in the A-attractive surface case. Even in the B-attractive surface case the structures become more complicated when the thickness L_y increases. With the confined space volume increasing to $L_y = 12$, almost two times the polymer period, two layers with lateral coexistence of parallel cylinders $C_{||}$ and perforated lamellae PL have been found. Such structure is present also for $L_y = 16$. Two layers of perforated lamellae PL_2 have been found at $L_y = 14$. Increasing the confinament dimension, also the number of the layer increases. For $L_y = 18$ one layer of perpendicular cylinders $C_\perp$ are surrounded by two layers of PL. The $C_\perp$ exhibits a pill-shape at $L_y = 18$, which is different from the elongated shape of the $C_\perp$ at the same thickness, $L_y = 18$, but different surface field $h > 0$. This is probably due to the fact that perforated lamellae occupies more space than wetting layer, such fact reduces the available space for the cylinders which can not elongate. When $L_y = 20$ one layer with the lateral coexistence of perpendicular and parallel cylinders to the thin film plain are surrounded by two layers of PL. Even in this latter case, the $C_\perp$ has a pill-shape. When the B-attractive surface is slightly stronger than $h = -0.2$ new morphologies have been observed. Two lamellae layers $L_{,2}$ for $L_y = 12$ and two layers of lateral coexistence of perforated lamellae and lamellae $(PL/L)_2$ at $L_y = 14$. At stronger B-attractive surface field $h = -0.4$ the phase behaviour is pretty similar to those at $h = -0.6$. For $L_y = 10$ and $h = -0.4$ one layer with coexistence of parallel cylinders and perforated lamellae has been found. For $L_y = 18$ and $-0.4 \leq h \leq -0.6$ one inner layer of perpendicular cylinders with two outer layer of lamellae has been found. At larger confinement $L_y = 20$ and $-0.6 \leq h \leq -0.4$ it has been found $L - C_{||}/C_\perp - L$, where $C_\perp$ have also pill-shape. Similar morphologies have been predicted in Huinink's study. Huinink et al.,[90] by using dynamic density functional theory (DDFT), studied asymmetric block copolymers confined in a thin film by varying both the slit width and surface-polymer interactions. They constructed a phase diagram with various phases, Table 1 and Figure 6: parallel cylinders at surface field $\xi = 0$ and slit width $L_y = 13$ (their original notation is $H = 13$ grid points) compared with $h = 0.4$ and $L_y = 14$ in Figure 4.2; perpendicular cylinders at $\xi = 0$ and $L_y = 8$ (their original notation is $H = 8$ grid points) compared with $h = 0$ and $L_y = 6$ in Figure 4.2; and parallel perforated lamellae at $\xi = 1.75$ and $L_y = 7$ (their original notation is $H = 7$ grid points) compared with $h = -0.1$ and $L_y = 8$ in Figure 4.2. In this chapter the findings are also consistent with some experiments conducted by Kim et al.

They studied the development of microphase-separated morphology in solvent-cast thin films of triblock copolymer polystyrene (PS)-polybutadiene (PB)- polystyrene (SBS) as a function of solvent evaporation rate. By decreasing the evaporation conditions, they found microstructures varying from cylinders with their axis perpendicular to the plane of the polymer thin film Figure 1b arranged in their hexagonal symmetry Figure 4a, to a duplex morphology containing perpendicular cylinders and in-plane cylinder morphology where their axes lie in the film plane Figure 1c, to a morphology made up entirely of in-plane cylinders Figure 1d arranged in a distorted hexagonal array Figure 4b.[109] In the next sections, it will be discussed the application of the shear flow and it will be exhibited that it has also be found such hexagonal symmetry in the plane perpendicular or in the plane parallel to the shear field.

4.2.3 Monolayer of perpendicular cylinders in thin film

In the previous section in Figure 4.2 it has been found that a monolayer of cylinders $C_\perp$ perpendicular to the surface can be induced by the presence of neutral surfaces in a cylinder-forming diblock copolymer for a separation distance $L_y = 6$. Here, the order of these diblock copolymer microdomains and their packing symmetries are investigated. Specifically, the results obtained by using smaller and larger square side, $L_x = L_z = 128$ and $L_x = L_z = 512$ are compared. To better visualize defects, Voronoi diagrams (see Chapter 3) for both cases are constructed. Figure 4.4, on the left, is the top view of the perpendicular cylinder phase at $L_y = 6$ and $L_x = L_z = 128$, and $h = 0$; Figure 4.4, on the right, is its corresponding Voronoi diagram. The pictures reveal that the perpendicular cylinders are arranged with hexagonal symmetry, with the presence of some defects. Black and gray polygons depict 7-5 neighbors defects (the number of sides of polygons is equal to the number of neighbors of the central microdomains). The Voronoi diagram shows clearly that the location of the grain boundary, composed mostly of 5-7 pairs, are inside of the structure. It is observed that the number of defects, the ratio of the defects number to the total number of cylinders, is: 5.72% for 5-defect and 5.05% for 7-defect. As it is possible to see from Figure 4.4 the microdomains have random orientation, highlighted from the different orientation of the sides between the several hexagons.

The case of larger square side is depicted in Figure 4.5. On the left, it is possible

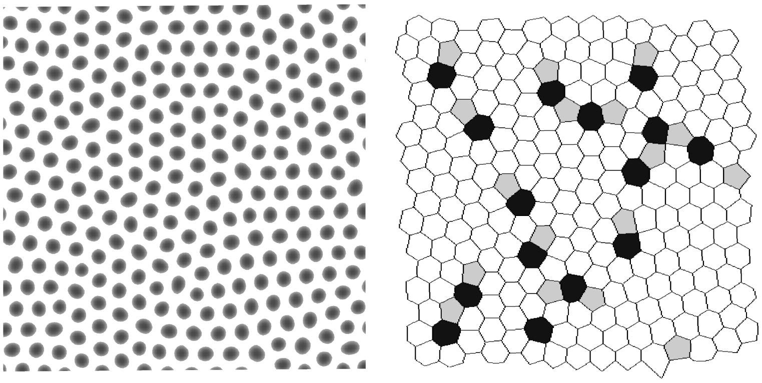

Figure 4.4: *Left: Top view on 3D CDS simulations of perpendicular cylindrical morphologies with neutral surface h=0 and $L_y = 6$, $L_x = L_z = 128$. Right: corresponding Voronoi diagram. Black and gray polygons depict 7-5 neighbors defects.*

to see the top view of the perpendicular cylinders, for $L_y = 6$ and $L_x = L_z = 512$. On the right, there is the corresponding Voronoi diagram. The Voronoi diagram in this second case, Figure 4.5, exhibits larger formation of grains compared to the first case, Figure 4.4. However, the percentage of the 5- and 7-defect is 6.56% and 6.29%, respectively. Therefore, the percentage of the defects in the smaller and larger square side confinement are very similar.

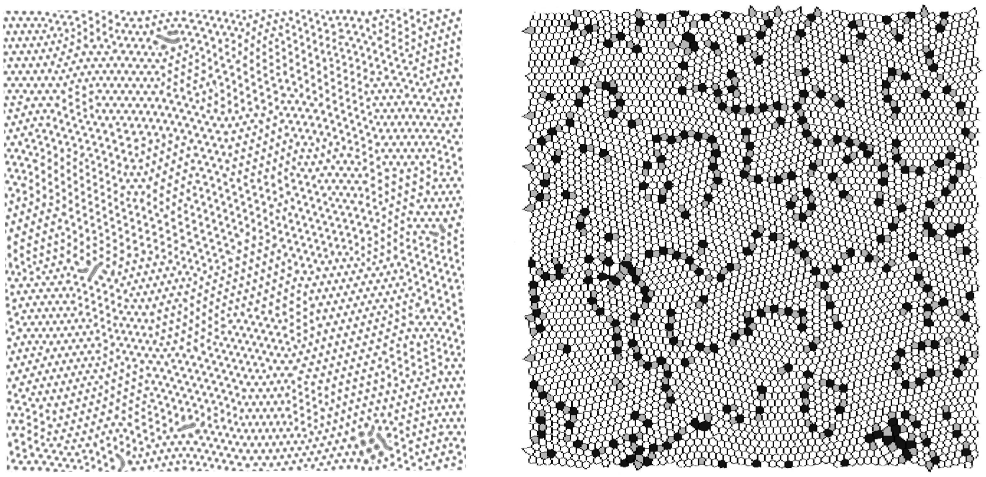

Figure 4.5: *Left:Top view on 3D CDS simulations of perpendicular cylindrical morphologies with neutral surface h=0 and $L_y = 6$, $L_x = L_z = 512$. Right: corresponding Voronoi diagram. Black and gray polygons depict 7-5 neighbors defects.*

4.2.3.1 Monolayer of perpendicular cylinders under shear flow

To tailor a desired structure, a manipulation by external field can be used. The perpendicular cylinder phase described in the previous section, induced by two parallel neutral slits $h = 0$ with thickness $L_y = 6$, and square side $L_x = L_z = 128$, have been submitted under a steady shear flow. Here, the effect of different strength of the shear flow $\tilde{\dot{\gamma}}$ are analyzed on the multi-grain packing observed in $C_\perp$. Prevented that the two cases at $L_x = L_z = 128$ and $L_x = L_z = 512$ have shown a similar phase behaviour, see previous section regarding the symmetry packing of the $C_\perp$ microdomains, for computational reasons we choose to submit the smaller square side's structure under shear flow. Figure 4.6, on the left, describes the top view of the perpendicular cylinders of figure 4.4 under the effect of different strengths of shear flow, $\tilde{\dot{\gamma}}$, which is applied from left to right; on the right the corresponding Voronoi diagrams.

In Figure 4.6, it is possible to see that when the shear flow strength is small, $\tilde{\dot{\gamma}} = 1 \cdot 10^{-5}$ and $\tilde{\dot{\gamma}} = 7 \cdot 10^{-4}$, the resulting morphology is weakly affected. In fact, the resulting morphologies exhibit a multi grain hexagonal packing with different orientations and with some defects, which is quite similar to the zero shear case, Figure 4.4. The percentages of defects detected in the Voronoi diagram are: 6.37% 5-defects and 6.71% 7-defects in case of $\tilde{\dot{\gamma}} = 1 \cdot 10^{-5}$; and 7.01% 5-defects and 6.66% 7-defects in case of $\tilde{\dot{\gamma}} = 7 \cdot 10^{-4}$. In both cases the cylinders are still perfectly perpendicular to the thin film plane. With the shear flow strength increasing to $\tilde{\dot{\gamma}}$ =0.005 a perfect single grain with hexagonal packing is obtained, with only 1.37% 5-defects and 0% 7-defects on the hedges. In this case the hexagonal packing is in the plane parallel to the shear flow direction, and the cylinders are tilted in the direction of the shear flow (from left to right). Some defects on the edge of the structure on Voronoi Diagram are due to the periodic boundary conditions, as example Figure 4.6 for $\tilde{\dot{\gamma}}$ =0.005. When the shear flow is above a certain threshold, $\tilde{\dot{\gamma}}$ =0.05, a phase transition from perpendicular to parallel cylinders is observed. The perpendicular cylinders turn into two alternated layers of half parallel cylinders, Figure 4.8. The two half layers of parallel cylinders, obtained for $\Delta t = 0.1$, show the half part turned in the direction of the walls. In this case it has been necessary to decrease the value of the time step, Δt, compare with the previous simulations, because the value of $\Delta t = 1$ gives rise to two layers of parallel crossed cylinders 4.7.

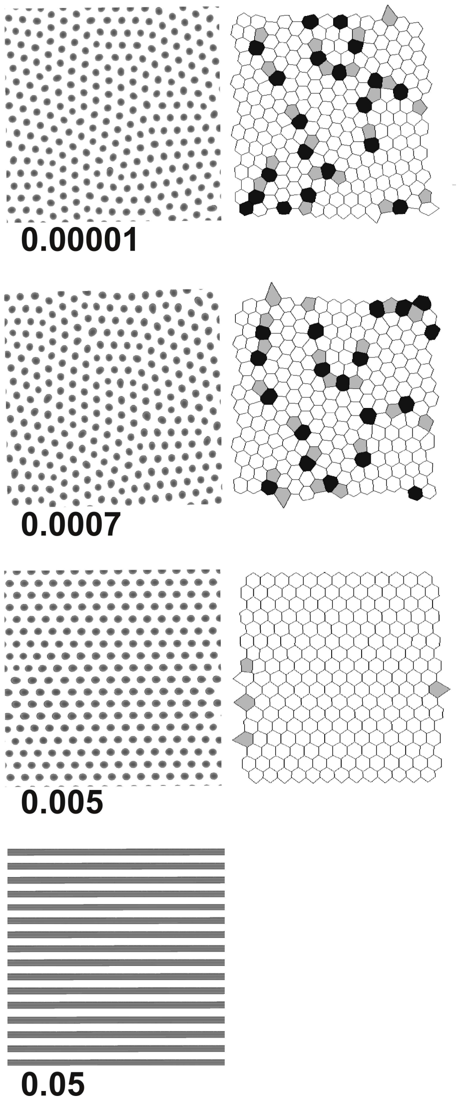

Figure 4.6: *Left column: Top view on 3D CDS simulations of cylinders, with neutral surfaces h=0 and $L_y = 6$, $L_x = L_z = 128$, under shear flow. Right column: corresponding Voronoi diagram. The shear flow from left to right, and numbers indicate the shear rate $\tilde{\dot{\gamma}}$.*

As seen in Figure 4.8, the shift of the two half parallel cylinder layers form a hexagonal symmetry in the yz-plane perpendicular to the shear direction, $x-$axis. In the side view picture in Figure 4.8, on the left, an half hexagon has been drawn to guide the eye.

Next, the kinetics of $C_{\perp}$ multy grain packing-to-$C_{\perp}$ single grain packing, observed in Figure 4.6 at $\tilde{\dot{\gamma}}$ =0.005 is discussed. Figure 4.9 shows the time evolution of the system depicted in the Figure 4.6 at $\tilde{\dot{\gamma}}$=0.005. At time step 0 the cylinders, perpendicular to the surface, show a multi-grain packing with random orientation, different direction of the sides between the several hexagons, and the defect density is 5.72% for 5-defect and

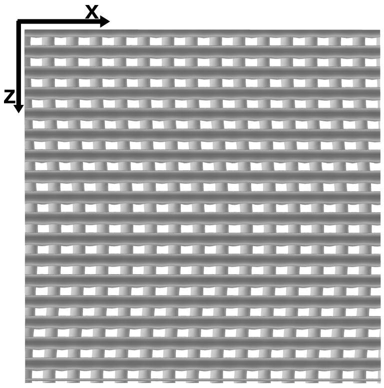

Figure 4.7: *Top view of the system for $L_y = 6$, $L_x = L_z = 128$, h=0 under shear flow with $\tilde{\dot{\gamma}}$=0.05. The shear flow is applied from left to right.*

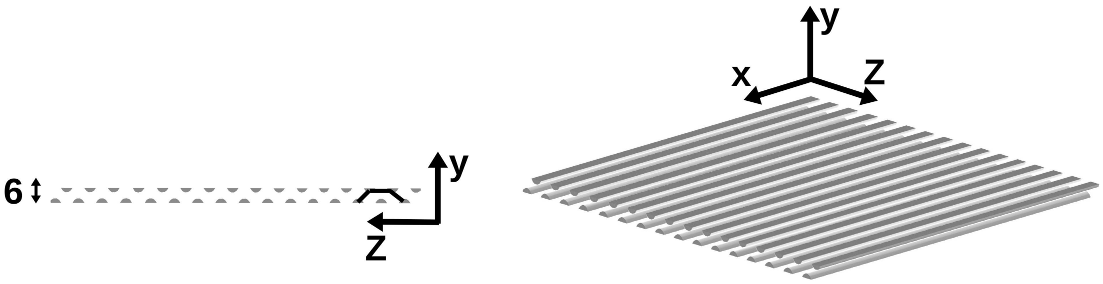

Figure 4.8: *Side view (left) and 3D view (right) of the system for $L_y = 6$, $L_x = L_z = 128$, h=0 under shear flow with $\tilde{\dot{\gamma}}$=0.05, applied in $x-$direction. The half hexagon on the left panel is shown to guide the eye.*

5.05% for 7-defect. The defects are located inside of the structure, forming the edge of the multigrain microdomains. When the time increases, time step 3000, we obtained 5.88% 5-defects and 7.84% 7-defects, and the cylinders start being tilted in the direction of the shear flow (from left to right). Even with a further increase of the time, time step 10 000, the defect density is 6.86% 5-defects and 9.15% 7-defects, similar to the previous time step, 3000. Multi-grain packing and random orientation are exhibited in both cases, time step 3000 and time step 10 000. To observe an important decrease of the defect density we have to reach time step 5 000 000 where it is found 1.37% 5-defects and 0% 7-defects. A few defects are along the hedge of the structure, and the microdomains form an almost single-crystal with hexagonal symmetry and orientation pinned by the shear flow direction.

To conclude this section, the kinetic of the system under $\tilde{\dot{\gamma}}$=0.05 is described, Figure 4.6. Figure 4.10 shows the time evolution from the top and side view of the system under

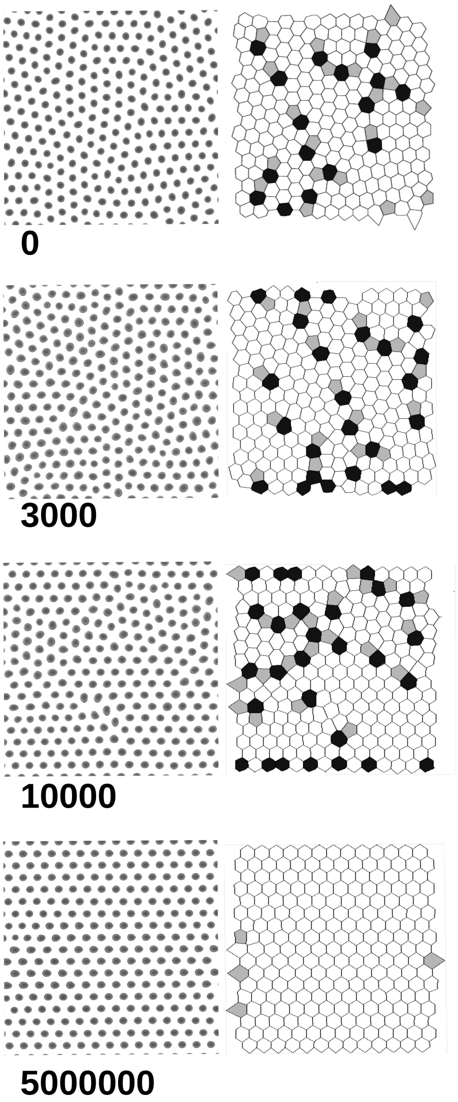

Figure 4.9: *Left column: Top view on 3D CDS simulations of the time evolution of cylinder with neutral parallel surface $h = 0$ and $L_y = 6$, $L_x = L_z = 128$, under shear rate $\dot{\gamma}$ =0.005. The numbers indicate the time steps. The shear flow $\tilde{\dot{\gamma}}$ direction is from left to right. Right column: corresponding Voronoi diagram.*

a steady shear $\tilde{\dot{\gamma}}$=0.05, depicted in Figure 4.6. As it is possible to see a stronger shear causes a breaking of perpendicular cylinders, whose morphology changes in cylinders parallel to the surface in the direction of the shear flow, from left to right.

As seen, at time 0 (time = time-steps $\cdot\Delta t$, where Δt=0.1) the cylinders are perpendicular arranged in a multi grain packing. The side views in Figure 4.10 exhibit both A- and B-blocks. On Figure 4.11, 3D view structures of A-blocks at different time are shown, which will be used in the next discussion. During the time evolution the perpendicular cylinders start tilting in the direction of the shear flow, from left to

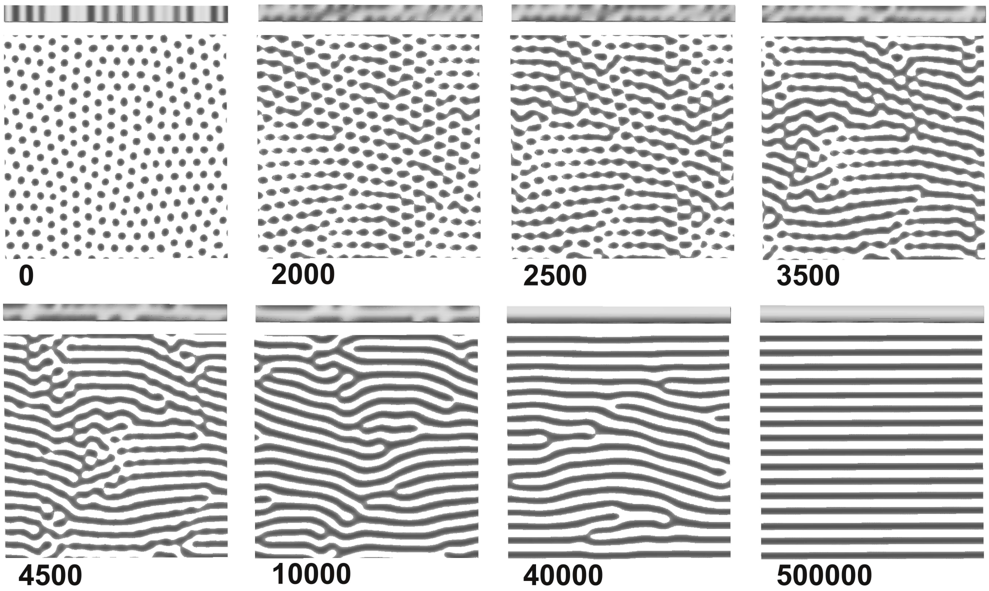

Figure 4.10: *Top view on the 3D CDS of the time evolution of cylinders (A-blocks) with neutral surface* $h = 0$ *and* $L_y = 6$, $L_x = L_z = 128$, *with shear rate* $\tilde{\dot{\gamma}}$*=0.05. The numbers indicate the time. The shear flow* $\tilde{\dot{\gamma}}$ *direction is from left to right. Side view of AB-blocks is shown above the top view structure.*

right. They become thinner until they break, time 2000. Half small parallel cylinders start appearing at time 2500 and at time 3500, which merge forming long half parallel cylinders in the shear flow direction, time 4500. Block copolymer defects are evident at time 10000, where isolated cylindrical dislocations are formed. Time 40000 shows long half parallel cylinders with reduced dislocations, which converge in straight half parallel cylinders perfectly aligned in the shear direction, from left to right, at time 500000. Figure 4.8 shows the 3D view of the two half parallel cylinder layers at $\tilde{\dot{\gamma}}$=0.05 and at time 500000. As already ascertained, the two layers are shifted, and form a hexagonal packing in the $yz-$plane perpendicular to the shear flow direction, $x-$axis.

4.2.3.2 Minkowski functional study for the perpendicular-to-parallel cylinders transition under shear flow

In the previous section, by using Cell Dynamics Simulation method, it has been presented the phase behaviour of perpendicular-to-parallel cylinders transition for $h = 0$ and $L_y = 6$ under applied shear flow $\tilde{\dot{\gamma}}$=0.05 by describing real-space pictures. To analyze such qualitative pictures in case of very complex interconnected structures is not trivial. In the modern theoretical physics the quantitatively analyze changes in topology and shapes of structures can be realized by using Minkowski functionals.[110] For 3D structures there are four Minkowski functionals: volume (V), surface area (S), integral mean curvature (2H) and Euler characteristic (χ). In this section, Minkowski functional is used to study transformations of perpendicular cylindrical BCP phase under shear flow in more details. Figure 4.11 shows Minkowski functionals for the system characterized by the transition from perpendicular-to-parallel cylinders under a steady shear flow $\tilde{\dot{\gamma}}$=0.05 illustrated in Figure 4.10. Crops of simulation snapshots are showed in the figure to highlight the kinetic pathway of the perpendicular-to-parallel cylinders transition. Figure 4.11 (a) shows the total volume V occupied by perpendicular-to-parallel cylinders transition for a given iso-surface level under a steady shear flow $\tilde{\dot{\gamma}}$=0.05.

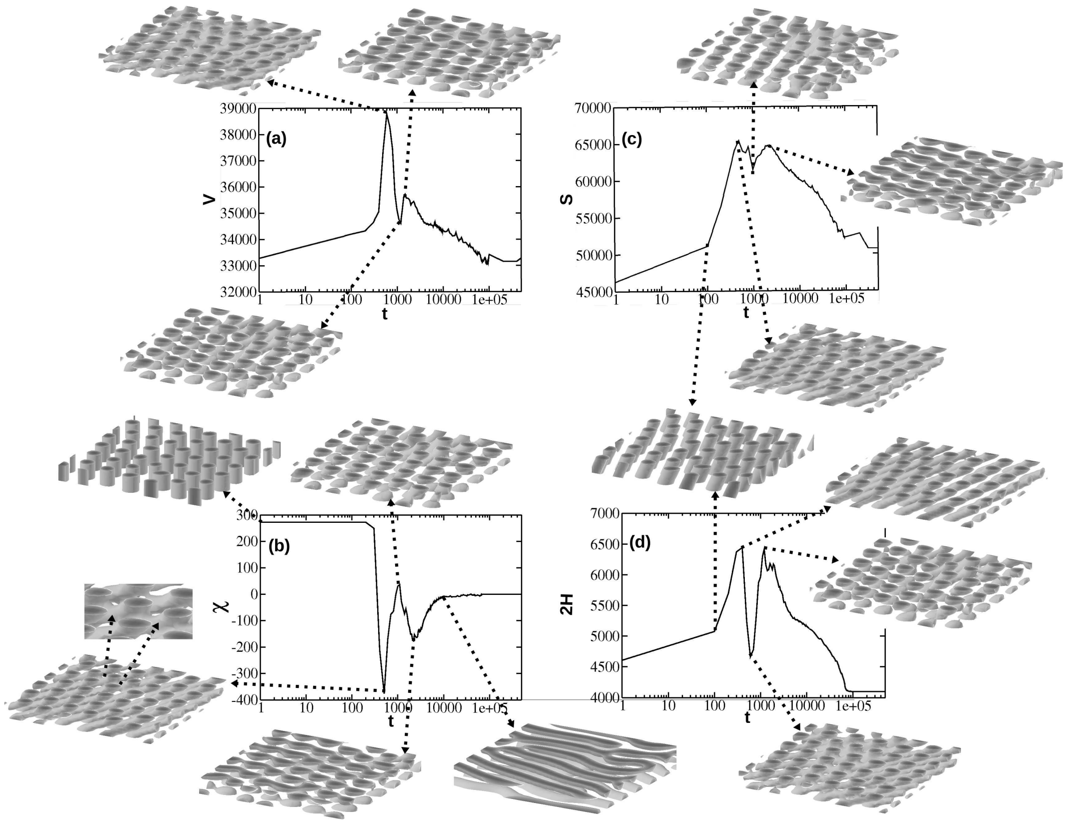

Figure 4.11: *Minkowski functionals as function of the time for system depicted on Figure 4.10 with shear flow* $\tilde{\dot{\gamma}}$*=0.05: (a): volume; (b): Euler characteristic; (c): surface area; (d): mean curvature. Morphologies as shown as crops of* $L_x = L_z = 50$ *of larger simulation boxes. Shear flow is applied from left to right.*

At the very first stage (time 300) of the application of the external field the volume V and the surface S increase, Figure 4.11 (a) and (c), respectively, which means that the system responds to the external perturbation by melting of the structures, and a consequent structure stretching by shear. At the same time the cylinders becomes thinner which is reflected in the increase of the mean curvature 2H. In fact, partial melting of the structure with a consequent slope of the cylinders causes an increase in the curvature at time 100, 2H Figure 4.11 (d), due to decrease of local radii of curvature. Increase of the volume does not contradict to the total mass conservation. The total volume of the block copolymer melt remains the same. The volume shown in the Figure 4.11 (a) is the volume occupied by one of the block component inside of a chosen iso-surface. The volume curve and the surface curve (Figure 4.11 (a) and (c), respectively) exhibit a main peak at time 600 and time 500, respectively, which corresponds a partial slope of the perpendicular cylinders in the shear flow direction, which has been applied from left to right. From the related snapshots it is possible to see how the slanted cylinders tend to melt and join with their neighbors. Moreover, the cylinders become thinner compared to the structure before the shear was applied (snapshot at time 1 in Figure 4.11 (b)). Also, the surface S and the mean curvature 2H have the first maximum very close, at time 500 and time 400 respectively. As seen from the corresponding snapshots the cylinders become thinner (small radii). The Euler characteristic, Figure 4.11 (b), is related to the topology of the structure. The Euler curve starts from a positive value regarding the number of the perpendicular cylinders, time 1. The topology of the structure remains unchanged until at time 200: the Euler characteristic χ remains the same, (Figure 4.11 (b)). As time proceeds the Euler curve reaches a minimum (time 500), and its negative value corresponds to an interconnected structure. Interconnections cause even a decrease of the mean curvature highlighted from the minimum at time 600 in Figure 4.11 (d). Then the Euler characteristic χ starts to increase and reaches a peak at about time 1100: connections perpendicular to the shear flow start to break. After that stage the volume V starts to recover reflecting the network connections break and reconnect in the shear flow direction, time 1500, forming two separated parallel layers. The second phenomenon which contributes in the increase and a consequent reaching of a second maximum of the mean curvature 2H is due to the cylinders which become more and more thinner until they break at time 1200, in Figure 4.11 (d). Also the surface curve S exhibits a second maximum at time 2000 describing a consequent evolution of the formation of the two parallel layers formed by independent block copolymer islands. After the interconnections are broken, the two ends of the cylinder become more and more straight and flat, and these block copolymer islands will merge between them in the respective layer until they form two layer of half parallel cylinders, which is reflected in the fall of both surface S and mean curvature 2H. Both of these values are lower than the corresponding ones for the highly interconnected cylinder. At the end, the Euler characteristic becomes zero, time 10000, which corresponds to the case of the cylinders with no interconnections. Due to the periodic boundary condition each cylinder is topologically seen as a torus, contributing zero to the total Euler characteristics. At the final stage (time 500 000) the volume V becomes almost the same compared to its starting stage, time 1. The latter can be attributed to the fact that the initial perpendicular cylindrical morphologies, at time 1, have global ordering as the two half parallel cylindrical layers are perfectly oriented in by the shear flow.

4.2.4 Monolayer of parallel cylinder thin film

A monolayer of parallel cylinder and a monolayer of parallel cylinder with perforated lamellae have been induced by 1D confinement at confinement space $L_y = 10$ and at B-attractive surface field $h = -0.2$ and $h = -0.4$, respectively, Figure 4.2. Figure 4.12 and Figure 4.13 show the top view and the 3D view of $L_y = 10$ at $h = -0.2$ and $h = -0.4$, respectively. As seen, with increasing the strength of the B-attractive surface field we observed a phase transition from $C_{||}$ to $C_{||}$-PL.

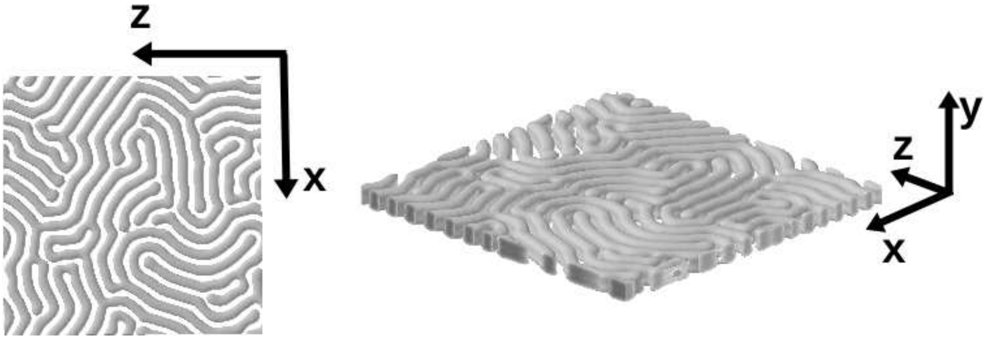

Figure 4.12: *Top view (left) and 3D view (right) of the system for* $L_y = 10$, $L_x = L_z = 128$, $h = -0.2$.

4.2.5 Monolayer of parallel cylinder thin film under shear flow

As it has been done for the monolayer of $C_\perp$ at $h = 0$ and $L_y = 6$, in this section the order of cylindrical diblock copolymer microdomains is investigated for $L_y = 10$ and for $h = -0.2$ and $h = -0.4$ under a steady shear flow. Figure 4.14 shows the top view of

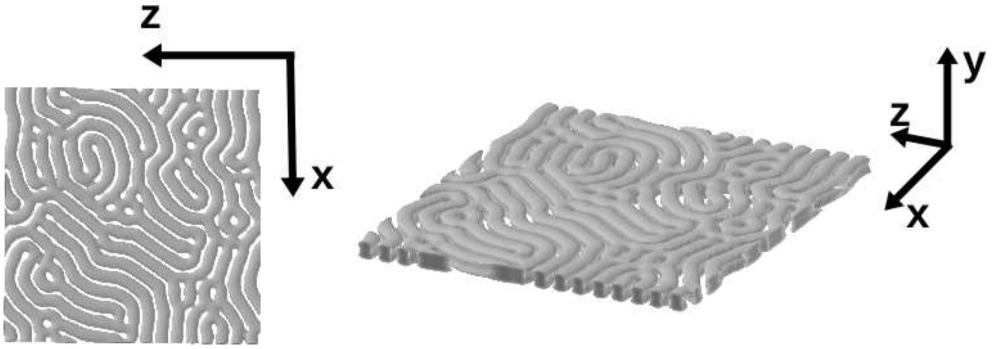

Figure 4.13: *Top view (left) and 3D view (right) of the system for* $L_y = 10$, $L_x = L_z = 128$, $h = -0.4$.

the resulting morphologies for the system depicted in Figure 4.12 under different shear flow strength applied from left to right.

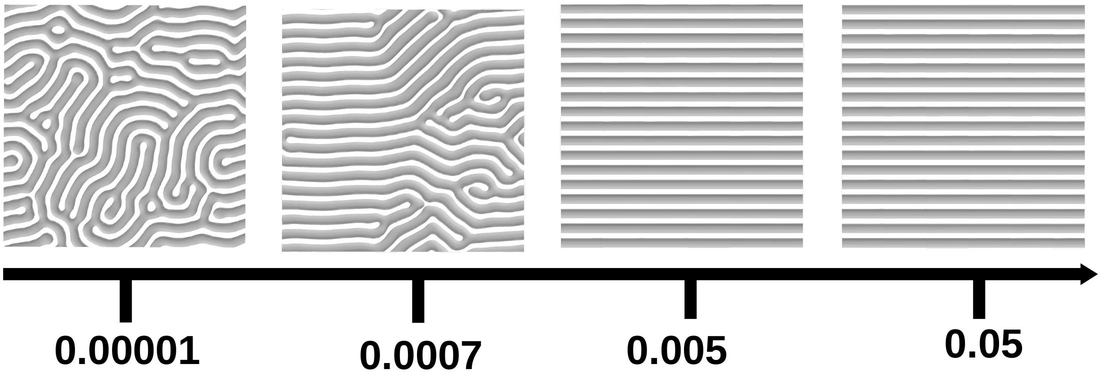

Figure 4.14: *Top view on 3D CDS simulations of* $C_{||}$ *morphology confined between two parallel walls with* $h = -0.2$ *for* $L_y = 10$ *and* $L_x = L_z = 128$ *under different shear rate* $\tilde{\dot{\gamma}}$ *applied from left to right.*

At a weaker shear flow $\tilde{\dot{\gamma}} = 1 \cdot 10^{-5}$ it has been noted a $C_{||}$ to $C_{||}/PL$ transition. With increasing the shear flow $\tilde{\dot{\gamma}} = 7 \cdot 10^{-4}$ the structure shows two behavior: half structure has cylinders with random orientation; and half structure has cylinders aligned in the shear direction. Higher shear flow $\tilde{\dot{\gamma}}$=0.005 exhibits cylinders aligned in the shear flow direction. At $\tilde{\dot{\gamma}}$=0.05 it has been used $\Delta t = 0.1$. Experimentally, Register and coworkers successfully applied a shearing force to thin film cylinder-forming diblock copolymer, polystyrene-poly(ethyl-ene-alt-propylene) (PS-PEP). They used a thick sacrificial layer of poly(dimethyl siloxane) (PDMS) to prevent rupture (or breakage) of the thin film during shearing, and obtained the long range ordering of cylindrical nanodomains aligned to the flow direction in the thin film, with thickness 30 nm, Figure 2a. Their experimental findings were also confirmed by their 2D simulations by using Cell Dynamics Simulation, Figure 4a.[98] In this section 3D CDS on parallel cylindrical phase, decreasing the shear rate from right to left Figure 4.14, confirm Register's 2D CDS findings, decreasing the shear rate from Figure 4a to Figure 4d. In Figure 4.15 it is possible to see the side view, on the left, and the 3D view, on the right, of the structure at $L_y = 10$ and $h = -0.2$ under $\dot{\gamma} = 0.05$. The section of the cylinders has a bottle-shape.

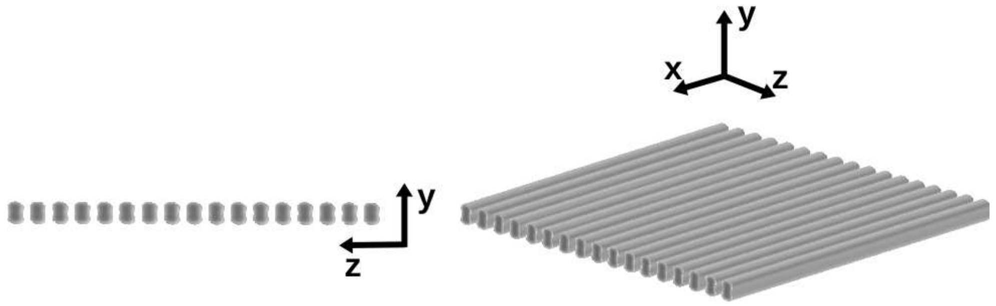

Figure 4.15: *Side view (left) and 3D view (right) of the system for $L_y = 10$, $L_x = L_z = 128$, $h = -0.2$, under shear flow with $\tilde{\dot{\gamma}} = 0.05$ applied in $x-$ direction.*

The phase behaviours observed for $L_y = 10$ and $h = -0.2$ under different shear strength are similar to those obtained for the system $L_y = 10$ and $h = -0.4$ in Figure 4.16. In this second case the initial morphology is $C_{||}/PL$ morphology, Figure 4.13. Figure 4.16 at $\tilde{\dot{\gamma}} = 1 \cdot 10^{-5}$ and $\tilde{\dot{\gamma}} = 7 \cdot 10^{-4}$ still shows coexistence of $C_{||}$ and PL morphologies. However, at $\tilde{\dot{\gamma}}$=0.005 and $\tilde{\dot{\gamma}}$=0.05, as seen in the previous case $L_y = 10$ and $h = -0.2$, the phase transition to parallel cylinder in the shear direction is completed. Even in this case, $\Delta t = 0.1$ is used for $\tilde{\dot{\gamma}}$=0.05.

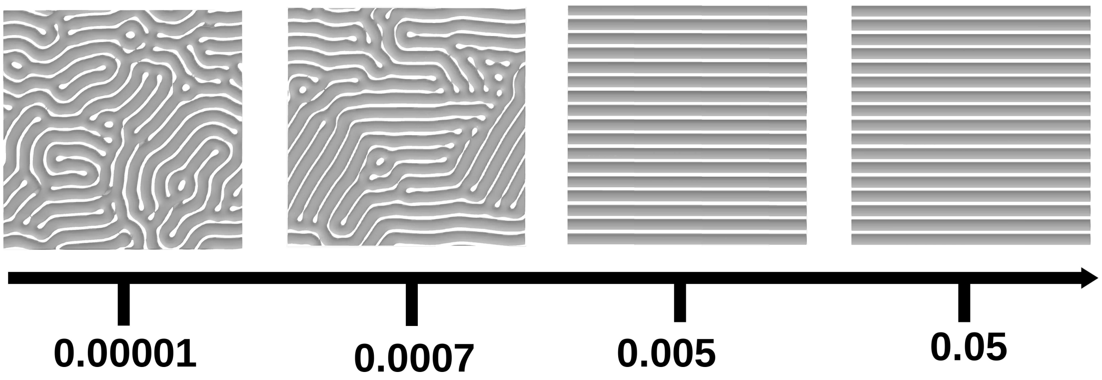

Figure 4.16: *Top view on 3D CDS simulations of $C_{||}/PL$ morphology confined between two parallel walls with $h = -0.4$ and for $L_y = 10$ and $L_x = L_z = 128$ under different shear rate $\tilde{\dot{\gamma}}$ applied from left to right.*

Finally, Figure 4.17 exhibits side view, on the left, and 3D view, on the right, of the system $L_y = 10$ and $h = -0.4$ under shear flow $\tilde{\dot{\gamma}} = 0.05$, where is clearly visible even in this case the bottle-shape of the cylinder section.

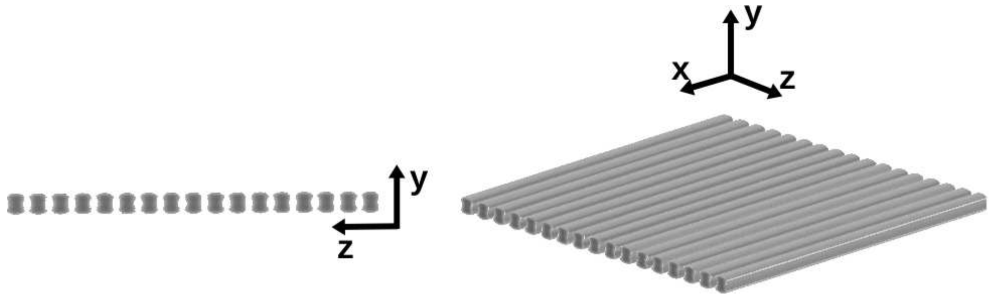

Figure 4.17: *Side view (left) and 3D view (right) of the system for* $L_y = 10$, $L_x = L_z = 128$, $h = -0.4$ *under shear flow with* $\tilde{\dot{\gamma}} = 0.05$ *applied in* $x-$*direction.*

Therefore, even if the initial conditions of the systems for $L_y = 10$ and $h = -0.4$ and for $L_y = 10$ and $h = -0.2$ at zero shear are different, the resulting morphologies of these two systems are similar under shear flow $\tilde{\dot{\gamma}} = 0.05$.

4.2.6 Monolayer of perforated lamellae thin film

In the structure diagram in Figure 4.2 it has been found a monolayer of perforated lamellae PL structure induced by the presence of a weaker B-attractive surface field $h = -0.1$ for confinement space $L_y = 8$. As it has been done for the monolayer of $C_\perp$ at $h = 0$ and $L_y = 6$, the order of these diblock copolymer microdomains and their packing symmetries is investigated. Specifically, the results obtained in the case of smaller and larger square sides, $L_x = L_z = 128$ and $L_x = L_z = 512$, respectively, are compared. Figure 4.18, on the left, is the top view of the perforated lamellae phase for $L_y = 8$ and $L_x = L_z = 128$, and for $h = -0.1$; on the right, its corresponding Voronoi diagram.

The pictures reveal that the PL are arranged with hexagonal symmetry with the presence of some defects. The Voronoi diagram shows clearly that the location of the grain boundary, composed mostly of 5-7 pairs, is inside of the structure. The defect density is 7.84% 5-defects and 4.71% 7-defects. As it is possible to see from Figure 4.18 the microdomains have random orientation, highlighted from the different orientation of the sides between the several hexagons.

The case of larger square side is depicted in Figure 4.19, where on the left it is possible to see the top view of the PL for $h = -0.1$ and $L_y = 8$ and $L_x = L_z = 512$, and on the right the corresponding Voronoi diagram. Even in the case of PL, as the

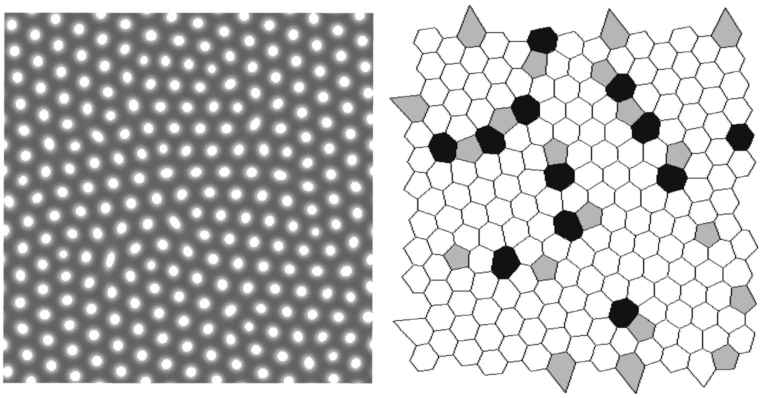

Figure 4.18: *Left: Top view on 3D CDS simulations of perforated lamellae morphologies with surface* $h = -0.1$ *and* $L_y = 8$, $L_x = L_z = 128$. *Right: corresponding Voronoi diagram.*

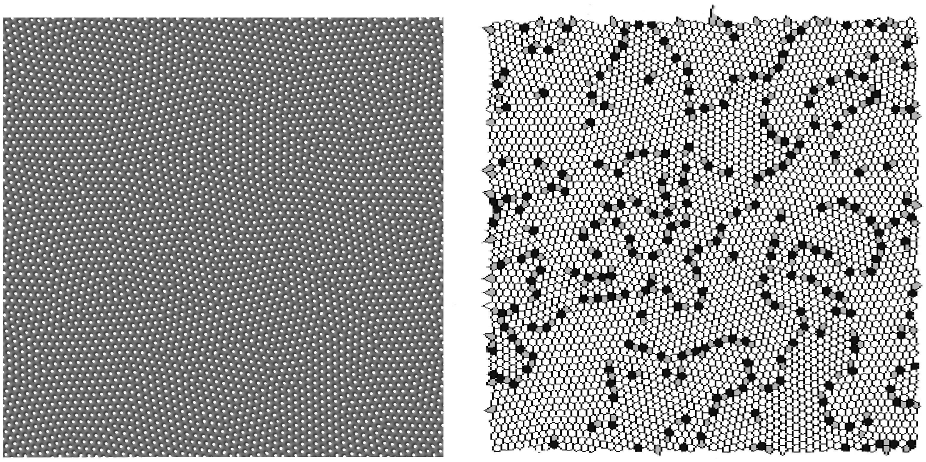

Figure 4.19: *Left: Top view on 3D CDS simulations of perforated lamellae morphologies with surface* $h = -0.1$ *and* $L_y = 8$, $L_x = L_z = 512$. *Right: corresponding Voronoi diagram.*

larger square side case of a monolayer of $C_{\perp}$, the Voronoi diagram in Figure 4.19 exhibits wider formation of grains compared to the case in Figure 4.18. The defect density in the case of PL with larger square side is 6.54% 5-defects and 6.02% 7-defects, quite similar to the smaller square side case.

4.2.6.1 Monolayer of perforated lamellae under shear flow

As seen in previous sections for a monolayer of perpendicular cylinders, here, the effect of different strength of the shear flow, $\tilde{\dot{\gamma}}$, on the multi-grain packing observed in one perforated lamellae layer are analyzed. A PL obtained by two parallel slits for $h = -0.1$

and for $L_y = 8$, $L_x = L_z = 128$ is used. Prevented the similarity between the two cases for $L_x = L_z = 128$ and $L_x = L_z = 512$, as $C_\perp$ case, square side $L_x = L_z = 128$ is used for computational reason. Figure 4.20, on the left, describes the top view of perforated lamellae of figure 4.18 under the effect of different strengths of shear flow, $\tilde{\dot{\gamma}}$, which is applied from left to right, on the right the corresponding Voronoi diagrams.

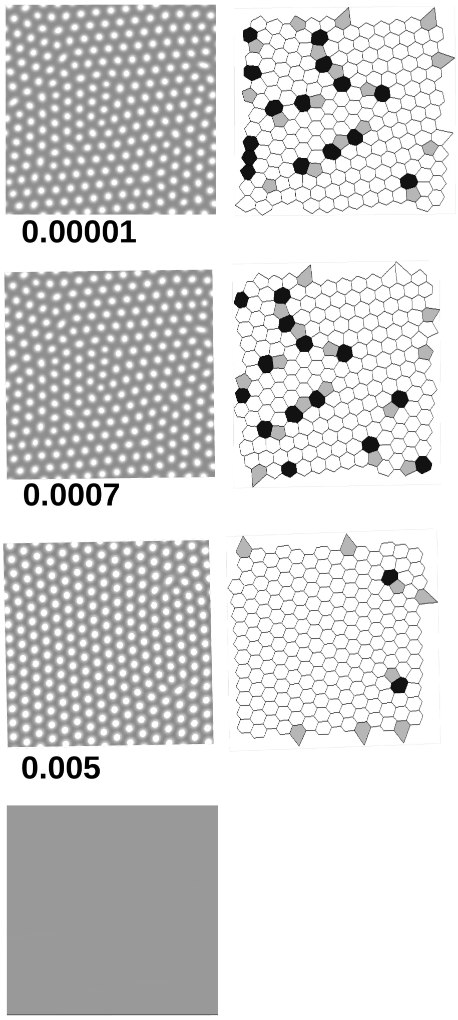
0.00001

0.0007

0.005

0.05

Figure 4.20: *Left column: Top view on 3D CDS simulations of lamellae with surface $h = -0.1$ and $L_y = 8$, $L_x = L_z = 128$, under shear flow. Right column: corresponding Voronoi diagrams. The shear flow direction is from left to right, and the numbers indicate the shear rate $\tilde{\dot{\gamma}}$.*

The resulting shear effect for $\tilde{\dot{\gamma}} = 1 \cdot 10^{-5}$ and $\tilde{\dot{\gamma}} = 7 \cdot 10^{-4}$, Figure 4.20 is very weak. In fact, the structure does not seem perturbed. The defect density is 6.51% 5-defects and 5.74% 7-defects at $\tilde{\dot{\gamma}} = 1 \cdot 10^{-5}$, and 5.79% 5-defects and 5.40% 7-defects at $\tilde{\dot{\gamma}} = 7 \cdot 10^{-4}$, which are slightly different from the case at zero shear, Figure 4.18.

The Voronoi diagram shows that the grain boundary, composed mostly of 5-7 pairs, is inside of the structure, and the microdomains have random orientation, different directions of the sides between the several hexagons. Only when the shear increases to $\tilde{\dot{\gamma}}$=0.005 we obtained an almost perfect single hexagonal packing. In this case, the defect density is 3.21% 5-defects and 0.80% 7-defects. As it is possible to see from the Voronoi diagram the microdomains with hexagonal symmetry have orientation improved by the application of the shear, from left to right. With the shear flow increasing to $\tilde{\dot{\gamma}}$=0.05 and $\Delta t = 0.1$, the perforated lamellae morphology is destroyed. Figure 4.20 $\tilde{\dot{\gamma}}$=0.05 exhibits as resulting morphology a single layer of lamellae. Figure 4.21 shows a 3D view of the lamellae morphology.

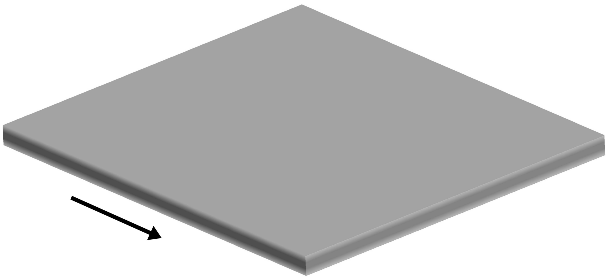

Figure 4.21: *3D view of lamellae morphology depicted in Figure 4.20 under $\tilde{\dot{\gamma}}$=0.05. The arrow indicates the shear flow $\tilde{\dot{\gamma}}$ direction.*

Next, the time evolution of the PL system depicted on Figure 4.20 at $\tilde{\dot{\gamma}}$=0.005 is studied. As it is possible see from Figure 4.22 at time step 0 and time step 90 000 Voronoi diagrams reveals a multi grain structure. At time step 90 000 the density defect is 6.25% 5-defects and 6.25% 7-defects. With the time step increasing to time step 2 200 000, we can observe a significant decrease of the density defect, 3.48% 5-defects and 2.71% 7-defects. Finally, at last stage, 5 000 000 time step, the structure has only a few defects but with a well-hexagonal order.

To conclude, the perforated lamellae-to-lamellae phase transition for $\tilde{\dot{\gamma}}$=0.05 is studied. The time evolution is depicted in Figure 4.23.

At time 10 the resulting phase is still a multi grain packing. However, it is noted that a stronger shear show, $\tilde{\dot{\gamma}}$=0.05, does not help the holes of the PL phase to improve their arrangement. In fact, at time 40 the picture shows that the holes tend to become smaller, until they are almost closed at time step 60. At time 90 the phase behaviour

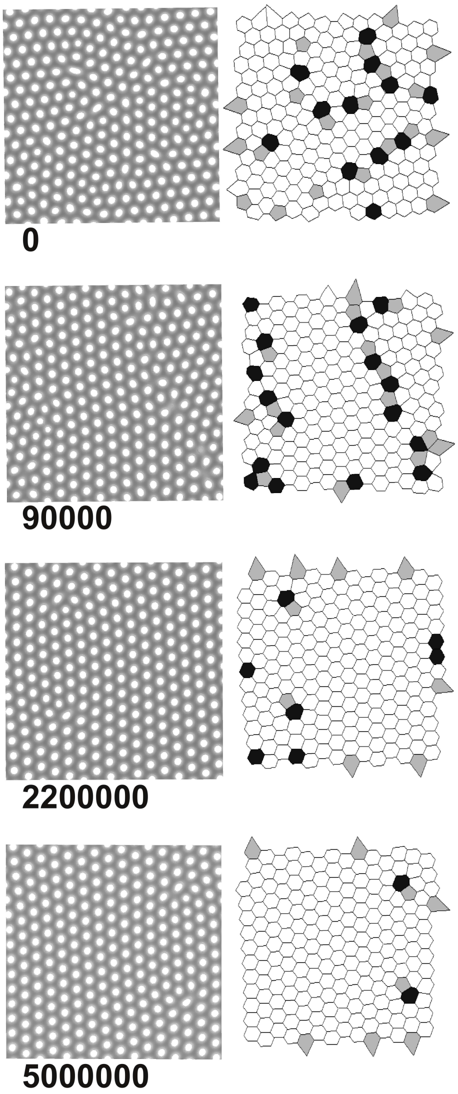

Figure 4.22: *Left column: Top view on the 3D CDS of the time evolution of perforated lamellae with surface* h*=-0.1 and* $L_y = 8$, $L_x = L_z = 128$, *under shear flow* $\tilde{\dot{\gamma}}$*=0.005. Right column: corresponding Voronoi diagram. The shear flow direction is from left to right, and the numbers indicate the time steps.*

of the system is a corrugated lamellae (see also on the bottom the 3D view of the corresponding picture). During the time evolution the corrugated lamellae tends to be less emphasized and the system becomes more flat, until time 500 000 as seen 4.20 at $\tilde{\dot{\gamma}}$=0.05.

4.2.6.2 Double layer thin film

In the previous section 4.2.2 in Figure 4.2, it has been observed that the number of the layers increases when the confinement dimension is near two polymer period $\sim 2L_0$. Double layers of coexistence of parallel cylinders with perforated lamellae and double

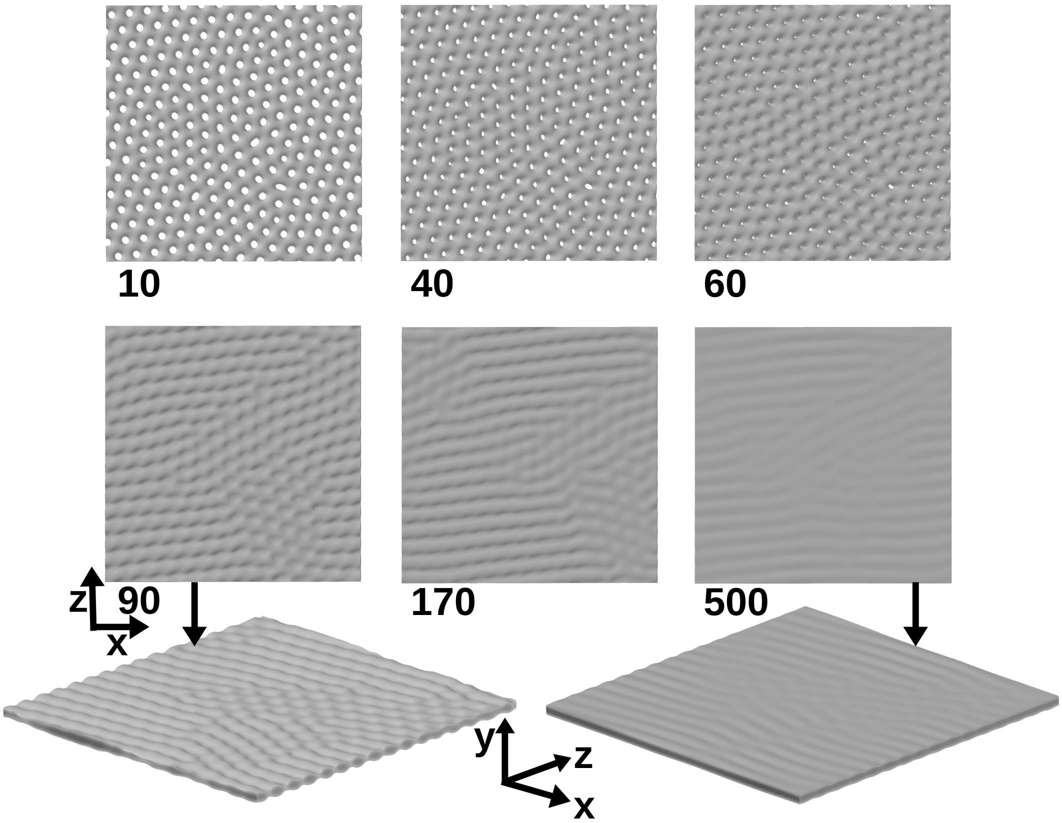

Figure 4.23: *Top view on the 3D CDS of the time evolution of perforated lamellae with surface h=-0.1 and L_y = 8, L_x = L_z = 128, under shear flow $\tilde{\dot{\gamma}}$=0.05. The shear flow direction is from left to right ($x-$direction), and the numbers indicate the time. Some 3D views are depicted on the bottom.*

layer of perforated parallel have been observed when the confined space is $L_y = 12$, $Ly = 14$, respectively, confined between two parallel walls when the confinement surface attracts long-blocks with strength $h = -0.1$. Figure 4.24 exhibits the top view of these morphologies. As it is possible to observe when the confinement dimension increases the morphology changes. The case of $Ly = 12$ for $h = -0.1$ is an intermediate morphology from the case $Ly = 10$ for $h = -0.1$, where only parallel cylinders to the thin film plane have been observed, and the case $Ly = 14$ for $h = -0.1$, where only perforated lamellae occurred.

In the case of $L_y = 14$ an hexagon has been drawn to guide the eye, and emphasize the hexagonal packing of the structure, although it is not perfect.

When the surface field and the confinement dimension increase the morphologies that have been observed are double layer of perforated lamellae. for $L_y = 14$ and h=-0.2, and for $L_y = 16$ and h=-0.2. These morphologies are depicted in Figure 4.25. An examination of these structure shows that the L_y influences the details of the resulting

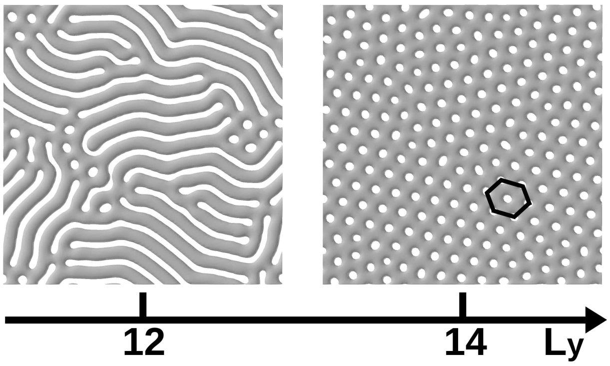

Figure 4.24: *Top view on 3D CDS simulations of the system for $L_y = 12$, $L_y = 14$ confined between a pair of parallel walls with h=-0.1, and $L_x = L_z = 128$.*

morphologies. In the case $L_y = 14$ it is possible to observe that between the holes of the perforated lamellae there are some small islands of lamellae. However, with the confined space volume increasing to $L_y = 16$ the whole surface is fitted with the holes, and the small part of lamellae are no longer present as in the previous case $L_y = 14$. Even in this case some microdomains are arranged in hexagonal symmetry.

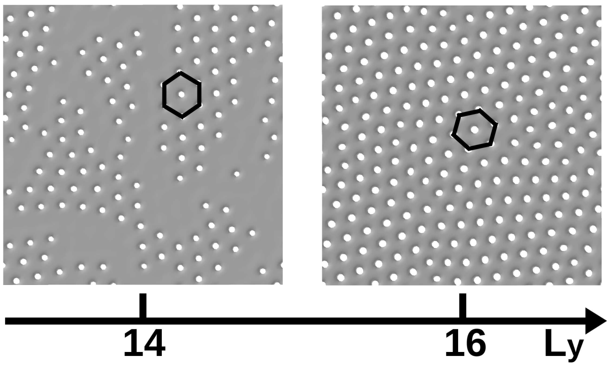

Figure 4.25: *Top view on 3D CDS simulations of for $L_y = 14$, $L_y = 16$ confined between a pair of parallel walls with h=-0.2, and is $L_x = L_z = 128$.*

4.2.6.3 Double layer thin films under shear flow

In this subsection the effect of a simple steady shear flow on two layers depicted in Figure 4.24 and in Figure 4.25 are studied. The effect of different strength of shear flow $\tilde{\dot{\gamma}}$ has been analyzed at different L_y, and different h.

The Figure 4.26 shows results for the system $L_y = 12$ and h=-0.1 under different strength of shear flow. The simulations in Figure 4.26 reveal that the parallel cylinder and perforated lamellae layers respond to an external stimulus at very small value of the strength shear flow $\tilde{\dot{\gamma}} = 1 \cdot 10^{-5}$, applied from left to right.

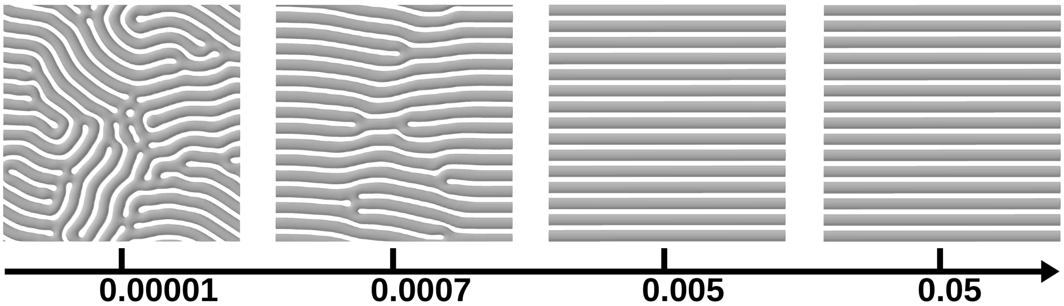

Figure 4.26: *Top view on 3D CDS simulations of the system with h=-0.1 under shear flow of different rate* $\tilde{\dot{\gamma}}$*. The box sizes is* $L_x = L_z = 128$ *and* $L_y = 12$*, The shear flow direction is from left to right.*

Although there is still coexistence of two different phase, parallel cylinders to the thin film plane and PL, the number of the holes is decreased. In fact, when $\tilde{\dot{\gamma}} = 1 \cdot 10^{-5}$, only one hole appears in the middle of the structure. The bent cylinders are not elongated along the shear flow direction, which is from left to right. When the shear flow increases, $\tilde{\dot{\gamma}} = 7 \cdot 10^{-4}$, the hole disappears and the morphology is formed by two double layer of parallel cylinders. This time the cylinders are slightly elongated along the shear direction (from left to right), but some defects are present. With the shear flow increasing to $\tilde{\dot{\gamma}} = 0.005$ the result of the simulation is two layers of parallel cylinders perfectly aligned in the shear direction. In addition, the top and the bottom layers are slightly shifted between them forming hexagonal packing in the plane perpendicular to the shear direction.

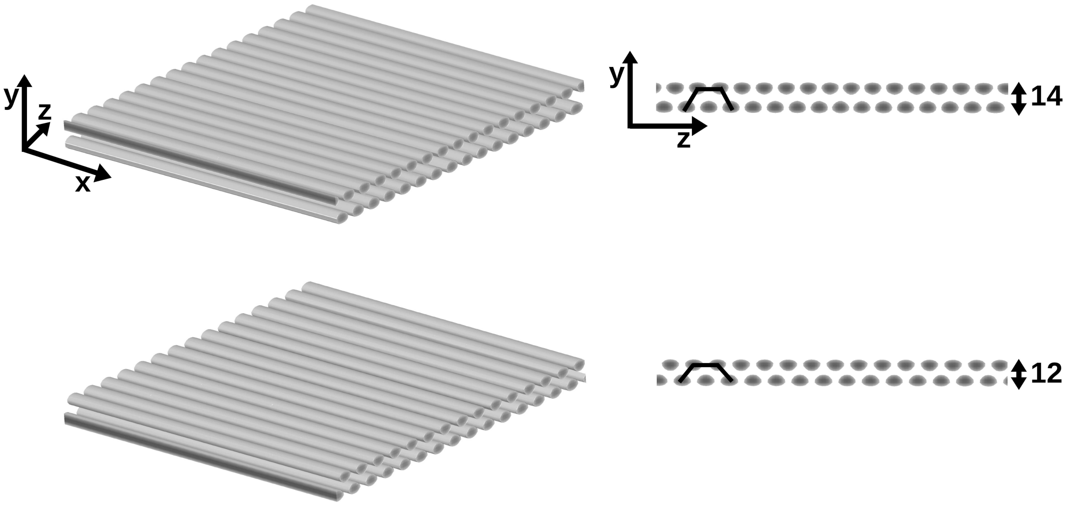

Figure 4.27: *3D view (left), and side view (right), of the system for* $L_y = 12$*,and* $L_y = 14$*,* $L_x = L_z = 128$*, h=-0.1 under shear flow with* $\tilde{\dot{\gamma}} = 0.05$ *applied in* $x-$*direction.*

The phase behaviour observed at $\tilde{\dot{\gamma}} = 0.005$ has been noted even for $\tilde{\dot{\gamma}} = 0.05$. However, in the latter case, $\tilde{\dot{\gamma}} = 0.05$, the time step has been decreased $\Delta t = 0.1$. The Figure 4.27 shows an hexagonal symmetry in the $yz-$plane, for $L_y = 12$ and $\tilde{\dot{\gamma}} = 0.05$, which is perpendicular to the shear direction, $x-$axis. Hexagonal packing of spheres perpendicular to the shear direction, Figure 9a at $\tilde{\dot{\gamma}} = 0.0001$, has been detected even in the computational study of Pinna et al.[39], and in the experimental work of Hamley et al.[111].

For a slightly higher confinement surface $L_y = 14$, Figure 4.28, at very small value of the shear flow $\tilde{\dot{\gamma}} = 1 \cdot 10^{-5}$ we did not observed any phase transition. Figure 4.28 still shows two perforated lamellae layers for $\tilde{\dot{\gamma}} = 1 \cdot 10^{-5}$. Therefore, it seems that thinner layers are more affected by a weak shear flow, in fact at $L_y = 12$ and $\tilde{\dot{\gamma}} = 1 \cdot 10^{-5}$ we observed a phase transition, Figure 4.26. As we can see from the Figure 4.28 some microdomains form hexagonal packing. When the shear flow strength slightly increase to $\tilde{\dot{\gamma}} = 7 \cdot 10^{-4}$ the phase behaviour is pretty similar to the case $\tilde{\dot{\gamma}} = 0.005$. In fact, the increase of the strenght of the shear flow gives rise to a more well hexagonal packing of the holes of the perforated lamellae.

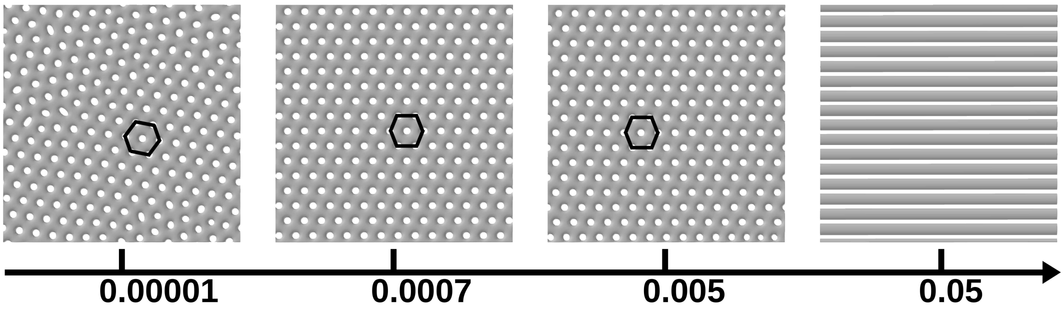

Figure 4.28: *Top view on 3D CDS simulations of the system with h=-0.1 under shear flow of different rate $\tilde{\dot{\gamma}}$. The box sizes is $L_x = L_z = 128$ and $L_y = 14$. The shear flow is from left to right.*

When the shear flow is equal to $\tilde{\dot{\gamma}} = 0.05$, the Figure 4.28 shows a phase transition from double layer of PL to double layer of parallel cylinders. The cylinders are aligned in the shear direction with the top and bottom layer shifted. Figure 4.27 shows that the simulation result for $\tilde{\dot{\gamma}} = 0.05$ and $L_y = 14$ forms hexagonal packing in $yz-$plane perpendicular to the shear direction, $x-$axis. Even in this case, the time step has been decreased $\Delta t = 0.1$. The systems for $L_y = 12$ and $L_y = 14$ for h=-0.1 show that if even the initial structures are different, Figure 4.24, the behaviour under a stronger shear flow $\tilde{\dot{\gamma}} = 0.05$ is the same, Figure 4.27.

When the surface field increases h=-0.2 for $L_y = 14$ and $L_y = 16$ the morphology obtained are two perforated lamellae, see Figure 4.25. First, the system for $L_y = 14$ and h=-0.2 have been study at different value of shear flow $\tilde{\dot{\gamma}}$, Figure 4.29.

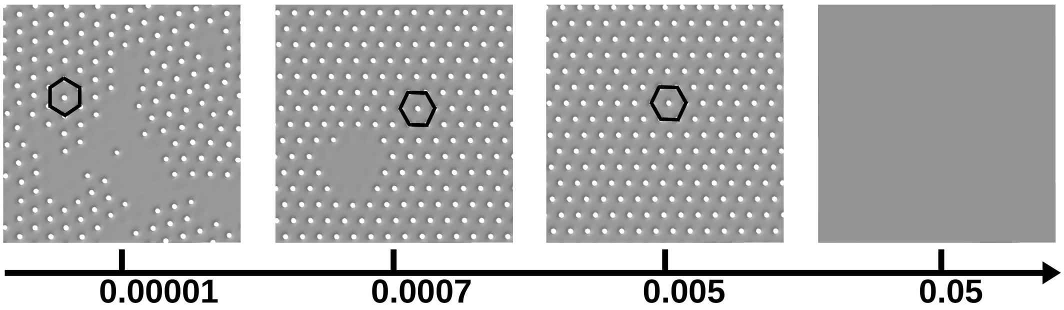

Figure 4.29: *Top view on 3D CDS simulations of system with h=-0.2 under shear flow of different rate $\tilde{\dot{\gamma}}$. The box sizes is $L_x = L_z = 128$ and $L_y = 14$. Shear flow direction is from left to right.*

For $\tilde{\dot{\gamma}} = 1{\cdot}10^{-5}$ the system is still pretty similar to the case at zero shear, Figure 4.25. The morphology is still a coexistence of lamellae and perforated lamellae. However, when $\tilde{\dot{\gamma}}7 \cdot 10^{-4}$ only one small island of lamellae is present, but the hexagonal packing of the holes of the perforated lamellae is improved. Phase transition appears for $\tilde{\dot{\gamma}}$=0.005, in fact the structure changes into only two perforated lamellae, with a good hexagonal packing. For a stronger shear flow $\tilde{\dot{\gamma}}$=0.05 and $\Delta t = 0.1$ a new morphology is observed, two layers of lamellae.

Similar behaviour is observed for $L_y = 16$ and h=-0.2, where different values of shear flow $\tilde{\dot{\gamma}} = 1 \cdot 10^{-5}$, $\tilde{\dot{\gamma}} = 7 \cdot 10^{-4}$, and $\tilde{\dot{\gamma}}$=0.005 improve the hexagonal packing. Only for $\tilde{\dot{\gamma}}$=0.05 and $\Delta t = 0.1$ there is a phase transition from two layers perforated lamellae to two layers of lamellae. Even in this case, although the initial configuration is not exactly the same, see Figure 4.25, the systems under a stronger shear flow $\tilde{\dot{\gamma}}$=0.05 show the same morphology, two parallel of lamellae.

In the phase diagram in Figure 4.2, the phase behaviour at $h = -0.6$ and at $L_y = 10$ has been defined as two BCPs layers of perforated lamellae. However, the case at $h = -0.6$ and at $L_y = 10$ does not show two well separated PL layers, see Figure 4.31 a), but they seem to be connected.

The connected PL at $h = -0.6$ and for $L_y = 10$ is probably due to the influence of the space confinement $L_y = 10$, which is a little bit larger than a polymer period $L_0 \approx 7.4$. Therefore, the confinement space for $h = -0.6$ and for $L_y = 10$ could be not enough to support two well-separated layers. In Figure 4.31 b) it is exhibited the

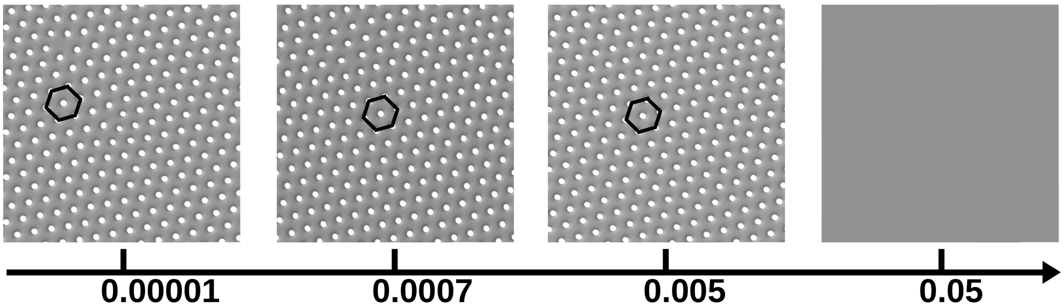

Figure 4.30: *Top view of 3D CDS simulations of the system with h=-0.2 under shear flow of different rate $\tilde{\dot{\gamma}}$. The box sizes is $L_x = L_z = 128$ and $L_y = 16$. The shear flow direction is from left to right.*

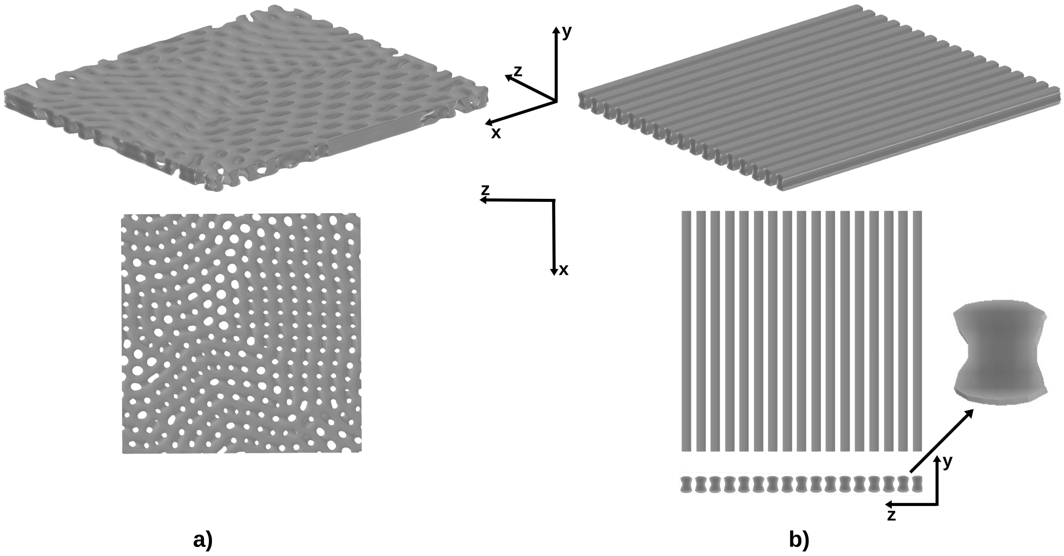

Figure 4.31: *Top view on 3D CDS simulations for the system with h=-0.6 and $L_y = 10$, $L_x = L_z = 128$, at zero shear a); and under shear along $x-$axis $\tilde{\dot{\gamma}}$=0.05 b).*

resulting morphology of the phase behaviour for $h = -0.6$ and for $L_y = 10$ under a steady shear flow $\tilde{\dot{\gamma}}$=0.05 after $5 \cdot 10^6$ time with $\Delta t = 0.1$. As it is possible to see in Figure 4.31 the application of a shear $\tilde{\dot{\gamma}}$=0.05 causes a phase transition from two connected PL layers, for zero shear Figure 4.31 a), to a sheared system of a parallel cylinders layer along $x-$axis, Figure 4.31 b). From the section of the lying cylinders in the thin film plane, side view on the bottom of Figure 4.31 b), it is possible to notice that they have a bottle-like shape.

4.2.6.4 Triple layer thin films

In the section 4.2.2 in Figure 4.2, triple layer of $PL - C_\perp - PL$ have been found for $L_y = 18$ and h=-0.1, and h=-0.2. Figure 4.32 shows the 3D view, and top and middle layer for $L_y = 18$ and h=-0.2. Bottom layer is not shown because is similar to the top layer. Top and bottom layer are PL with some holes arranged in hexagonal packing. Instead, the middle layer is made by perpendicular cylinders, where some of them are also arranged in hexagonal packing.

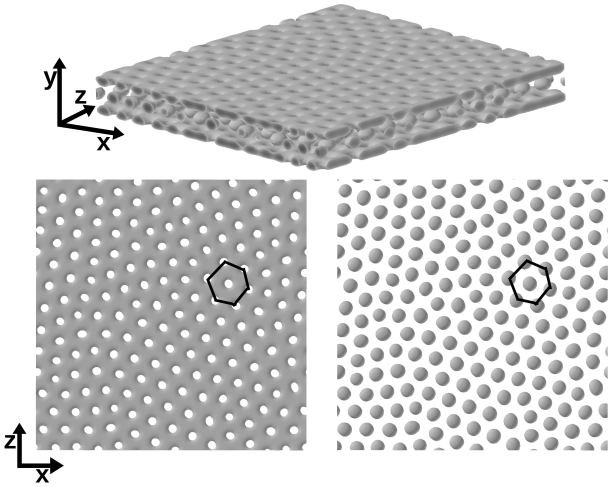

Figure 4.32: *Top: 3D view of 3D CDS simulations h=-0.2 and $L_y = 18$, $L_x = L_z = 128$. Bottom, top (left) and middle layers (right).*

4.2.6.5 Triple layer thin films under shear flow

The system described in the previous section 4.2.6.4, h=-0.2 and $L_y = 18$, $L_x = L_z = 128$, has then been studied under the effect of different strength of shear flow $\tilde{\dot{\gamma}}$, applied from left to right. Figure 4.33 shows on the left the top layer and on the right the middle layer. The bottom layer is not shown because is similar to the top layer.

For $\tilde{\dot{\gamma}} = 1 \cdot 10^{-5}$ both top and middle layer show hexagonal packing, which improve for $\tilde{\dot{\gamma}} = 7 \cdot 10^{-4}$. When the value of the shear flow increases, $\tilde{\dot{\gamma}}$=0.005, the top layer still show hexagonal packing. Instead the middle layer show a phase transition from perpendicular cylinders arranged in hexagonal packing to a coexistence of perpendicular cylinders, still in hexagonal packing, and parallel cylinders elongated in the direction of the shear, from left to right. For $\tilde{\dot{\gamma}}$=0.05 and $\Delta t = 0.1$ the phase transition affect both outer and inner layer. In fact the outer layers became lamellae, instead the inner layer became parallel cylinders to the thin film plane, elongated alg the shear flow direction from left to right.

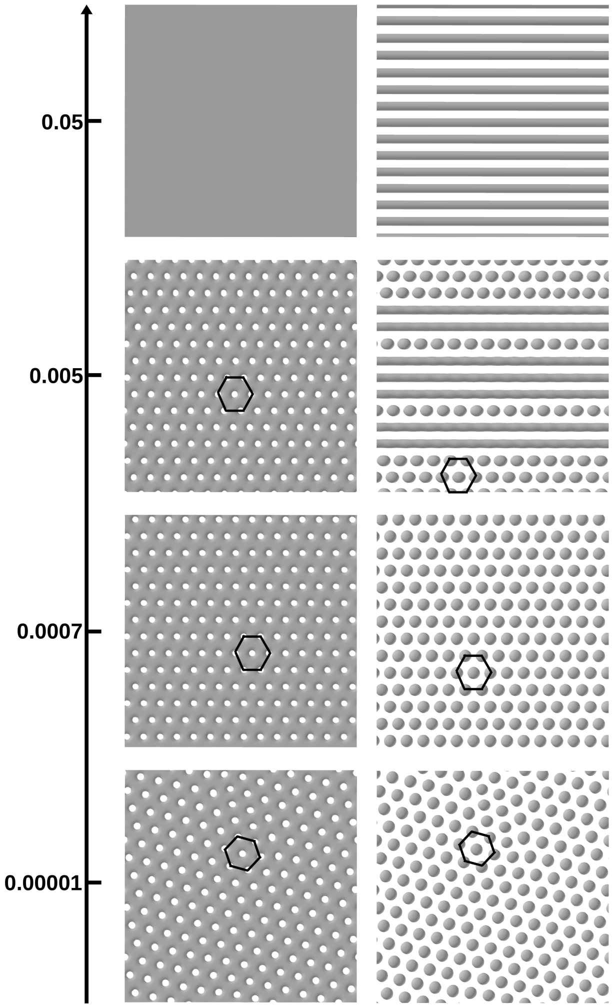

Figure 4.33: *Top view on 3D CDS simulations for h=-0.2 and $L_y = 18$, $L_x = L_z = 128$, under different of shear rates $\tilde{\dot{\gamma}}$. Shear flow is applied from left to right. Left column top layer, right column middle layer.*

4.2.7 Parallel and perpendicular-to-parallel cylinders transition under a steady shear flow

In the previous section 4.2.2 it has been described the structure diagram of BCPs confined between two parallel walls as a function of the surface field and the distance between the walls, resulting morphologies in Figure 4.2. In the case of neutral surface h=0 exhibits the poor influence of the confinement on the resulting structures. As shown in the central column of Figure 4.2, for h=0 and for $8 \leq L_y \leq 20$, the self-assembled structure is a chaotic coexistence of perpendicular and parallel cylinders It is noted that such morphology having the same type of microstructure may occur at different thickness values L_y. In fact, the confinement does not change the essential feature of the structure. However, an examination of these morphologies shows that the confinement value influence the details of the resulting morphology. The morphologies with thickness $L_y = 8$, $L_y = 14$, $L_y = 20$ and square side $L_x = L_z = 128$ depicted in Figure 4.34 , show that the number, the orientation, the position, and the length of the perpendicular and parallel cylinders can vary.

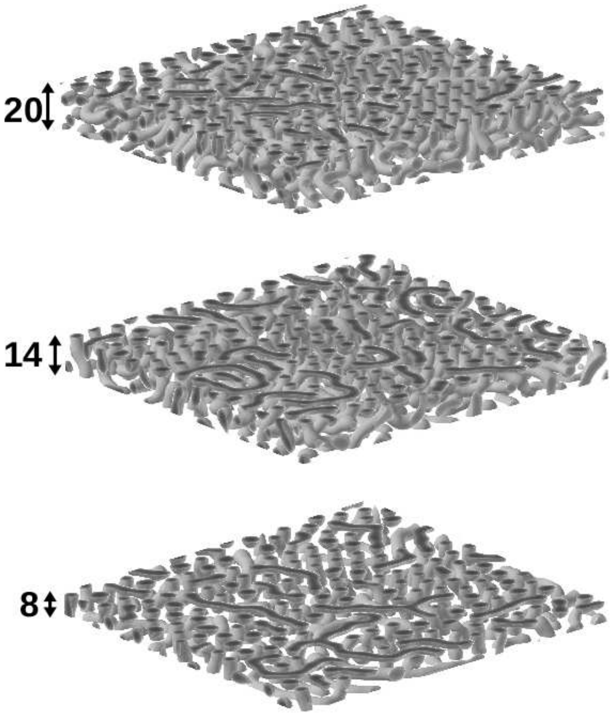

Figure 4.34: *3D CDS simulations of cylinder-forming diblock copolymer confined between two parallel neutral walls, h=0, as a function of the confinement dimension L_y with $L_x = L_z = 128$.*

In order to observe how such morphology can react under the effect of an external force, a steady shear flow with strength $\tilde{\dot{\gamma}}$=0.005 has been applied. The simulation results for the three different confinement values, $L_y = 8$, $L_y = 14$, $L_y = 20$, are shown in Figure 4.35 at 5 000 000 time steps and $\Delta t = 0.1$. As seen in Figure 4.35, top and side view are displayed on the left, 3D view is on the right. At first sight it is possible to note that the resulting effect is the same: layers of parallel cylinders are aligned in the shear flow direction, $x-$axis. However, a carefully examination of these morphologies show that L_y value does influence the details of the resulting morphology. When the confinement space is $L_y = 8$, near a polymer period $L_0 = 7.4$, two layers of half parallel cylinders shifted between them, and some full cylinders placed in the middle of these two layers are found arranged between the two confinement surfaces. However, the structure exhibits some defects in the middle of the system, see Figure 4.35. With the confined space volume increasing to $L_y = 14$, approximately $\sim 2L_0$, an increase of the number of the parallel cylinder layers has been obtained. As seen in Figure 4.35 one layer of cylinders is surrounded by two layers of half parallel cylinders. The two layers of half parallel cylinders are symmetrically arranged, instead the middle layer of cylinders is shifted compare to the outer layers. However, the half-and full parallel cylinders are perfectly aligned in the shear direction, along $x-$axis. It has been half and full parallel cylinders which are completely elongated along the shear direction $x-$axis, and have hexagonal order in the plane perpendicular to the shear direction $yz-$plane, schematic representation in Figure 4.35. Such hexagonal packing is partially visible in the case of $L_y = 8$.

The final case shows that when the thickness increases $L_y = 20$, approximately $\sim 3L_0$, it has been observed four layers perfectly aligned in the shear flow direction, Figure 4.35. Two shifted layers of parallel cylinders are surrounded by two shifted layers of half parallel cylinders. Moreover, the outer layer is symmetrically arranged respect to the farest inner layer. Even in this case it is possible to observe the hexagonal arrangement is in the plane $yz-$plane perpendicular to the shear direction $x-$axis.

4.3 Conclusion

Using Cell Dynamics Simulations a systematic investigation of cylinder-forming diblock copolymers melt confined between a pair of parallel hard walls has been performed. The morphologies of the confined copolymer melt sensitively depends on the surface field as well as the film thickness. Using different values of the film thickness and different surface fields, different phases have been obtained, i.e. wetting layer, parallel cylinder, perpendicular cylinder, perforated lamellae, lamellae, coexistence of perpendicular and parallel cylinder, and coexistence of parallel cylinder and perforated lamellae. Using dynamic density functional theory Huinink's et al. found perpendicular cylinders to the thin film plane at space confinement around the natural bulk period and neutral walls, and parallel cylinders in films with surfaces having a preferences for one of the blocks of the copolymer (selective surface).[90] In the present work, it has been found that the self-assembled structures, confined between neutral walls, are different from those confined

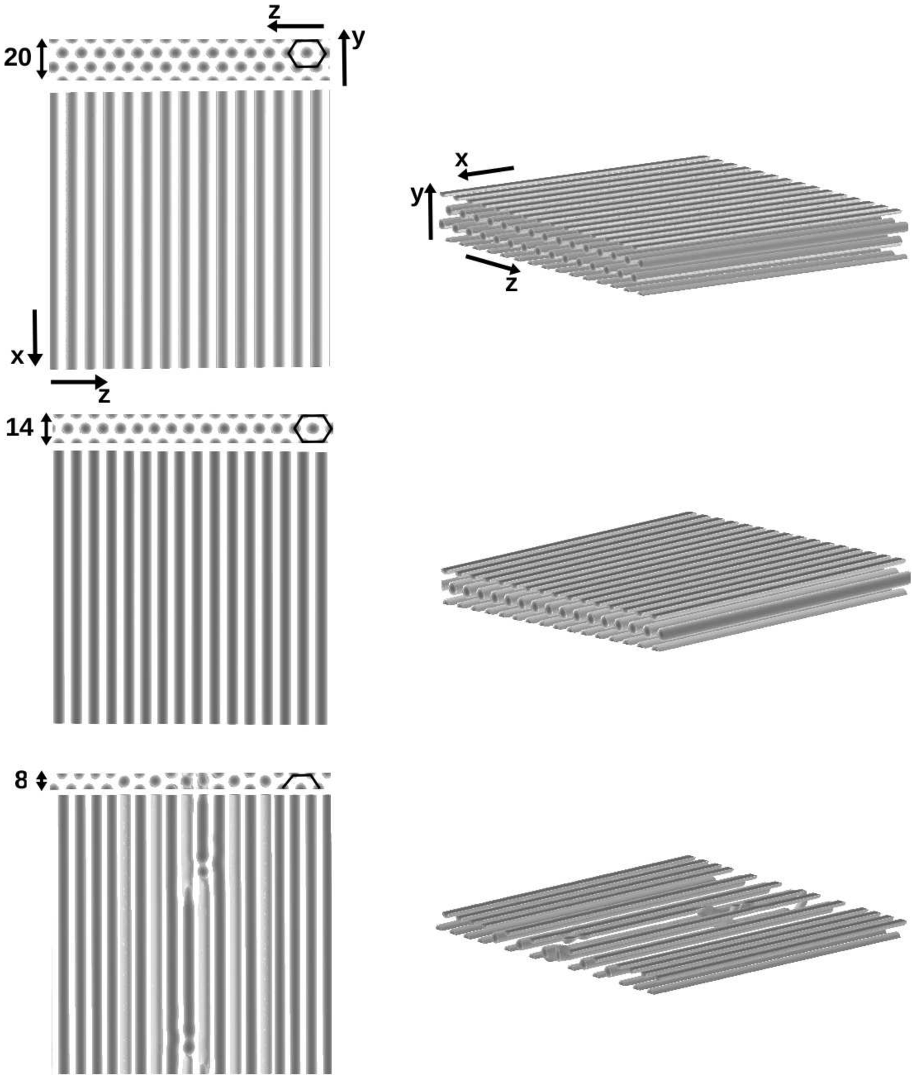

Figure 4.35: *Film morphologies for* $\tilde{\dot{\gamma}}$*=0.005 and* h*=0 as a function of the film thickness* L_y *and* $L_x = L_z = 128$*. The shear flow direction is along* $x-$*axis. Top and side views are shown on the left, 3D views are shown on the right.*

under short- and long-blocks attractive surface. Also, the self-assembled structures confined between short-blocks attractive surface are different from those confined under long-blocks attractive surface. To tailor a desired structure, some of the morphologies previously obtained have been manipulated by a steady shear flow. In this chapter the attention has been focused on the study of perforated lamellae, perpendicular cylinder, and parallel cylinders in thin film, around $\sim L_0$ and $\sim 3L_0$. Under the effect of the shear field, details of the kinetic pathway of the transition are studied. We found that the field can improve hexagonal packing in monolayer of perpendicular cylinders, in monolayer and double layer of perforated lamellae, and also in the case of $PL-C_\perp-PL$. However, shear flow is also observed to induce transitions between morphologies from perforated lamellae to lamellae; from perpendicular cylinders to parallel cylinders; from parallel cylinders with random orientation to one layer of cylinders in the shear direction; from two layers of perforated lamellae to parallel cylinder layers, from two layers of perforated lamellae to two layers of lamellae, and from $PL - C_{\perp} - PL$ to $L - C_{||} - L$. In this chapter, hexagonal symmetry has been observed in both plane parallel or perpendicular to the shear direction. In this chapter the phase transition from perforated lamellae-to-parallel cylinder morphology is similar to the one found by Ly et al.'s, although Ly et al. used electric field.[99] Also, the perfect alignment of parallel cylinders in the direction of the shear flow is in agreement with Register's experimental and computational work.[98] Overall, the current findings provide insights into how shear can be used to tailor structure of cylinder-forming diblock copolymers. Hopefully these findings can be useful for future studies.

Chapter 5

Lamellar-, Cylinder-, Bicontinuous-, and Sphere-Forming Diblock Copolymers in Spherical Confinement

Synopsis

Self-assembly of lamellar-, cylinder-, bicontinuous- and sphere-forming diblock copolymers in spherical confinement are examinated by using cell dynamics computer simulation. Various microstructures are found as a function of confinement size and confinement surface preference.

5.1 Introduction

Nanostructures by self-assembly of block-copolymers (BCPs) have great potential for technological applications as lithographic templates, nanoreactors or nanocontainers for drug delivery or self diagnostic devices[79,112] The nanoconfinement of block copolymers is an interesting method to produce novel morphologies. The influence of confinement can break the symmetry of a structure, stabilizing non bulk morphologies. The simplest confinement is one-dimensional (1D) in which the block copolymers are placed between two flat, parallel surfaces. Experimental[71,113–116] and computational[82,89,117–121] studies have explored the effect of the film thickness and surface preference to one or the other block on symmetric and asymmetric block copolymers. The interplay between the surface preference and the confinement determines deviations from the morphologies observed in the bulk. For the structures such as cylinders in the bulk, one can observe perforated lamellae, parallel or perpendicular (with respect to the surface) lamellae or cylinders in confinement.[71,122,123] In our previous work in Ref.[108] we have investigated the effect of cylinder-forming block copolymer within lateral confinement. We observed that square and hexagonal packing of cylinders perpendicular to the thin film plane depend on the size and the shape of the lateral confinement.[108] Another confinement is a two-dimensional (2D) confined system in which the block copolymers are located in cylindrical nanopores. Experimental[124–127] and computational[44,45,128–136] work have investigated block copolymers self-assembly in cylindrical nanopores. In cylindrical pore geometry, the surface field, the commensurability, and the curvature influences the morphologies. It leads to the creation of novel systems not found in the bulk or in 1D confinement. For instance, asymmetric diblock copolymers confined within cylindrical pores can give rise to helices, stacked toroids, and perforated tubes.[137] Sevink et al.[45], by using dynamic density functional theory, investigated the morphology of symmetric block copolymer in a cylindrical pore. Depending on the energetic wall polymer interactions, they found perpendicular lamellae for neutral or almost neutral interactions, and a parallel lamellae for stronger preferential interactions.[45] Li et al.[128], studied diblock copolymer melt confined in a cylindrical nanopore using self-consistent field theory. They observed for instance structures intermediate between lamellae and cylinders.[128] On the basis of these observations, a three-dimensional confinement (3D), in which block copolymers are placed in a spherical confinement, can lead to new morphologies different from those observed in 1D or 2D confined systems. The sphere confinement is a very interesting technique which has attracted attention of the scientific community.[79,112,138–141]He et al.[131], by means Montecarlo simulations, studied self-assembly of symmetric diblock copolymers within 2-(parallel walls or circle) and 3-dimensional (spherical or cylindrical) space. The interactions between boundaries and diblock copolymers and boundary shape give rise to the formation of novel self-assemble structures, e.g., strip, circle, core-multishell, and multibarrel-layer structures.[131] Fraaije et al[138], by using Dynamics density functional theory (also known as dynamic self consistent field simulation), studied block copolymer droplets. By changing block copolymer composition and the radius, they discovered many remarkable structures. They found onion structure of alternating A and B layers for nearly symmetric block copolymers. For slightly less symmetric block copolymers they discovered concentric perforated layers with a mixed pores pattern of pentagons, hexagons, and septagons. More asymmetric polymers formed cylindrical phase[138]. Yabu et al.[139] experimentally demonstrated a novel and simple method to prepare block-copolymer nanoparticles for droplets of tetrahydrofuran (THF) solution of polymers (polystyrene and polyisoprene) immersed in a poor solvent (water). They observed the formation of microphase separation structures in the block-copolymer nanoparticles, with uniform size and spherical shape. The polymer nanoparticle size is affected by the preparation conditions such as the concentrations of the solutions and the mixing ratio of the good and the poor solvents. They observed block-copolymer nanoparticles in a well-developed lamellar structure. Sevink and Zvelindovsky[142], by using dynamic self consistent field theory, studied the self-assembly block copolymers amphiphiles, which can form a rich variety of complex structures. For instance, for an asymmetric block copolymers they found ellipsoid-like droplets with an internal structure of stacked lamellar disk or slabs with a long axis coinciding with the normal to lamellae, and onion-like structures. In the case of highly asymmetric molecules, the block copolymers form cylinders which are arranged as: concentric or broken tori.[142] Yu et al.[141], by using simulated annealing Monte Carlo simulations, investigated self-assembly of symmetric diblock copolymers confined in spherical nanopores by varying the degree of the confinement and the strength of the surface interactions. They observed that in the case of strong surface preference toward A-blocks concentric-spherical lamellae (onion-like structures) are obtained. The A-blocks segregate to the surface because of the strong surface-preference, while the core of the concentric-spherical lamellae can be either A or B, depending on the degree of the confinement. When the surface-preference is close to the neutral surface field, they observed lamellae perpendicular. At intermediate surface field values, they found a rich variety of complex morphologies. For instance, A-blocks form perforated concentric-spherical lamellae, while the B-blocks form structures embedded in the holes of the A-domains. At weakly preferential surface, they found also helical structures.[141] Chantawansri et al.[143], by using self consistent field theory, studied lamellar- and cylinder-forming diblock copolymer confined on a surface of a sphere in 2D. They studied the formation of defects in the lamellar and cylindrical phases, and their dependence on sphere radius. Uneyama[144] carries out numerical simulations of vesicle formation based on the density functional theory for block copolymer solutions. By changing parameters such as the volume fraction of polymers or the Flory-Huggins interaction parameter between the hydrophobic subchains and solvents, they obtained spherical micelles, cylindrical micelles, or bilayer structures.[144] Rider et al.[145] investigated the 3-dimensional of lamellae and cylinder-forming BCPs in silica colloidal and inverse colloidal crystal. They observed for instance a packed BCP spheres, lamellar onions, and "golf-ball"-type morphology.[145] Chen et al.[140], by using self consistent field theory, performed a systematic study on self assembled microstructures for a cylinder-forming AB-diblock copolymer in spherical confinement. They considered the effects of the surface field and confinement diameter on the diblock copolymer self-assembly. The complexity of the structures that they found increases with increasing the confined volume: an irregular A-block (minority component) droplet; four small A-block droplets symmetrically arranged; systems with thirteen or more droplets; a single sphere surrounded by close cylinders with spherical shape; a mixture of droplets and short cylinders; a single empty sphere surrounded by close cylinders with square shape; a single empty sphere surrounded by droplets; and a single sphere (with a small sphere inside) surrounded by a layer of close cylinders with square shape and a layer of close cylinders with circular shape. When the confinement surface attracts A-blocks, they observed structures similar to the neutral surface case. For the B-attractive surface new structures have been observed, such as: perforated cube, a single sphere. For confinement dimension near four times the natural bulk period they found a single empty sphere surrounded by close cylinders with triangular shape; a single sphere (with a small sphere inside) surrounded by droplets and close cylinders with square shape; and a structure totally composed of droplets.[140] From a computational point of view, Pinna et al.[79], by using Cell Dynamics Simulation, investigated morphologies of thin block copolymers film around a spherical nanoparticle, They performed a systematic study for lamella- cylinder-, and sphere-forming diblock copolymers with respect to different film thickness, particle radius, and boundary conditions at the films interfaces. For lamellae-forming diblock copolymer with similar interfaces, they found, at a certain value of the film thickness, lamellae morphology (onion-like structures) in the case of preferable affinity of one of the blocks for the surface. Changing the surface preference to the another block they observed the inversion of the lamellae sequence. In the case of neutral surface they observed perpendicular lamellae. For intermediate strengths of the surface interaction a mixed morphology develops combining perpendicular and parallel lamellae. By changing the film thickness they found a perforated lamellae with a mixture of five and six neighboring perforations. They also found hybrid structure, where preferential surface induces parallel lamellae while other, neutral surface induces perpendicular lamellae. By changing the film thickness they obtained an asymmetric perforated lamellae morphology with cylindrical necks. For cylinder-forming diblock copolymer they found that selective surfaces can induce, one or two layers of parallel cylinders as a function of the film thickness, and at a certain film thickness a coexistence of parallel cylinders and perforated lamellae has been observed. When the surface is neutral or slightly selective they found perpendicular cylinders, with Y-shape defects. In the case of cylinder-forming diblock copolymers within dissimilar interfaces they found hybrid structures consisting of perpendicular and parallel cylinders. For sphere-forming diblock copolymer and similar interfaces they found one or two layers of spheres , order all in a lattice of five and six neighbors. Changing the affinity from the long- to short-blocks they observed hybrid system of spheres and perpendicular cylinders.[79] Vorselaars et al.[146], by using self consistent field theory,(adjusted for solving structured polymers in a three-dimensional spherical geometry), studied AB diblock copolymers grafted to a spherical core by their B ends. By varying the composition of the diblock, they found that end-block domains A transform from dots to stripes to a layer with holes and finally to a uniform shell.[146] Yang et al.[112] used simulated annealing for a mixture of AB-diblock copolymer and an incompatible C-homopolymer in three-dimensional confinement. They investigated four typical cases: in which the pore surface is equally selective to A, B but repulsive to C; selective to B but repulsive to A and C; neutral to all the three species; and selective to B and C but repulsive to A. In each case, particles with phase separated internal morphologies are obtained as functions of the degree of the confinement and the volume fraction of the homopolymer. They focused on the lamellae-forming and cylinder-forming diblock copolymers. They observed that inside a particle the homopolymers segregate to form one or two domains, therefore the homopolymer may act as an additional controlling parameter for the shape and symmetry of the copolymer domain. When they studied the case in which the surface is equally selective to A, B but repulsive to C, for symmetric AB-diblock copolymers, they found a core-shell particles with the copolymers as the shell wrapping around a homopolymer core. By varying the confinement size and the homopolymer concentration they obtained structures such as: stacked toroids, a single helix, double helices with the terminal part free, or connected in one side, or connected in both sides, two rings with saddle shape, and a ring with saddle shape and an arc. When the pore surface is selective to one block but repulsive to the other block of the copolymer and the homopolymer, they obtained for a symmetric AB-diblock copolymers and C homopolymers onion-like structures. They found a Janus-like particles with the copolymers and the homopolymers on different sides. But they also observed a core-shell particles, with a spherical homopolymer core or a copolymer-homopolymer combined core. When the surface is neutral to all three species they found, for symmetric block copolymers and C homopolymers, that the homopolymers usually form one partial-spherical cap in one side, while the copolymer segregate in a lateral structures in the another side. When the surface is selective to the B-block of the copolymers and the C-homopolymers but repulsive to the A-block of the copolymers they found different morphologies. For symmetric copolymers, they obtained copolymer domain of truncated concentric spherical structures and the homopolymer forms a partial-spherical cap in the another side. For an asymmetric copolymers, they observed that the minority A-blocks form stacked toroids or stacked toroids with spheres, and helix-shape. For a slightly less asymmetric diblock copolymers they found that the A-blocks form truncated shell structures located inside the B-matrix, and the homopolymer forms a spherical cup-shape in one side.[112]

We decided to perform the current study by using a coarse graining technique, Cell Dynamics Simulations (CDS), because our goal is to study how the morphology transforms in a three dimensional spherical confinement. This method is much less computationally intensive compared with more rigorous methods discussed above. CDS is a relatively fast method (see review[25] for a comparative estimate of CDS and DDFT runtimes) and has a good record of describing rather complex experimental phenomena in BCPs.[25,28] Using this code we study self-assembly of lamellae-, cylinder-, bicontinuous-, sphere-forming diblock copolymers confined in spherical cavities. We focused on the dependence of the self-assembled morphologies on the confinement space and the strength of the surface preferences. In addition, to the results that have been found in the literature, here we perform an extensive study by analysing a much wider range of parameters, which helped to obtain several morphologies, most of them comparable with others findings. A variety of structures in these 3D confined system are predicted from our study. To our knowledge, this is the first simulation of spheres in spherical confinement. The systems that have been found can potentially serve as building material for intelligent nanosize bioreactors and vesicles as drug delivery vehicles or self regulating diagnostic devices.[22,23]

5.2 Results and discussion

Diblock copolymers melts in spherical confinement are studied using cell dynamics simulation. Figure 5.1 shows the schematic picture of our system.

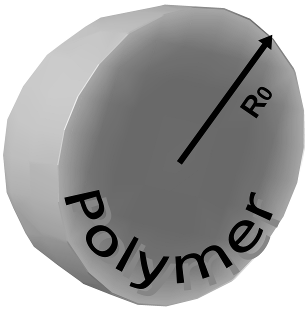

Figure 5.1: *Schematic representation of the proposed system.*

As boundary condition, we choose the most simple model in which the preference of copolymer blocks to the surface is modelled by Dirichlet boundary condition for the order parameter $\psi(R_0) = \psi_0$. Therefore, varying ψ_0 we effectively model the affinity of the surface towards one or another block copolymer component. In this section, results are presented for four typical cases changing the BCP composition: lamellae-, cylinder-, bicontinuous-, spherical-forming diblock copolymer. In each case, three main types of confinement surface are considered: a) neutral surfaces, wherein the surface has no preference for any block ($\psi_0 = 0$); (b) A selective surface, wherein the confinement surface is selective toward A-blocks but is not selective to B-blocks ($\psi_0 < 0$). This case is further subdivided in five cases, where the strength of the selective surface linearly increases from weak to strong interaction ($-0.1 \leq \psi_0 \leq -0.5$); (c) B selective surface, wherein the confinement surface is selective toward B-blocks but is not selective to A-blocks ($\psi_0 > 0$). This case is further subdivided in five cases, where the strength of the selective surface linearly increases from weak to strong interaction ($0.1 \leq \psi_0 \leq 0.5$). Under different selective surface, the self-assembled structures are studied as a function of the confinement (D/L_0), where $D = 2R_0$ is the confinement diameter and L_0 is the natural bulk period. All simulations have been carried out for 100 000 time steps. In this section, simulation results are presented in the form of morphology diagrams. The structure diagrams are displayed in terms of the interaction parameter $\psi_0 = 0$, $\psi_0 > 0$, $\psi_0 < 0$ and spherical confinement D/L_0 for lamellae-forming case, Figure 5.2, cylinder-forming case, Figure 5.3, bicontinuous-forming case, Figure 5.6, and sphere-forming case, Figure 5.7.

5.2.1 Lamellae forming system

For a lamellae forming system we choose the simplest case of symmetric diblock copolymer with equal volume fractions of both blocks, $f = 0.5$. The other parameters entering in Eq. 2.2 are $A = 1.5$, $B = 0.02$, $D = 0.5$, $v = 1.5$, $u = 0.5$, $\tau = 0.3$.[79] In describing our results we use a characteristic length scale L_0 which is the domain spacing of the bulk lamellae. From our previous simulations it is measured to be $L_0 \sim 8$ grid points.[79] Figure 5.2 shows the phase diagram of lamellae-forming diblock copolymer, induced by 3-D spherical confinement, as a function of confinement size D/L_0 and the surface affinity ψ_0.

As is evident from Fig.5.2 the structure diagram is symmetric with respect to $\psi_0 = 0$ line, which is expected for a symmetric block copolymer. Different shades of gray in

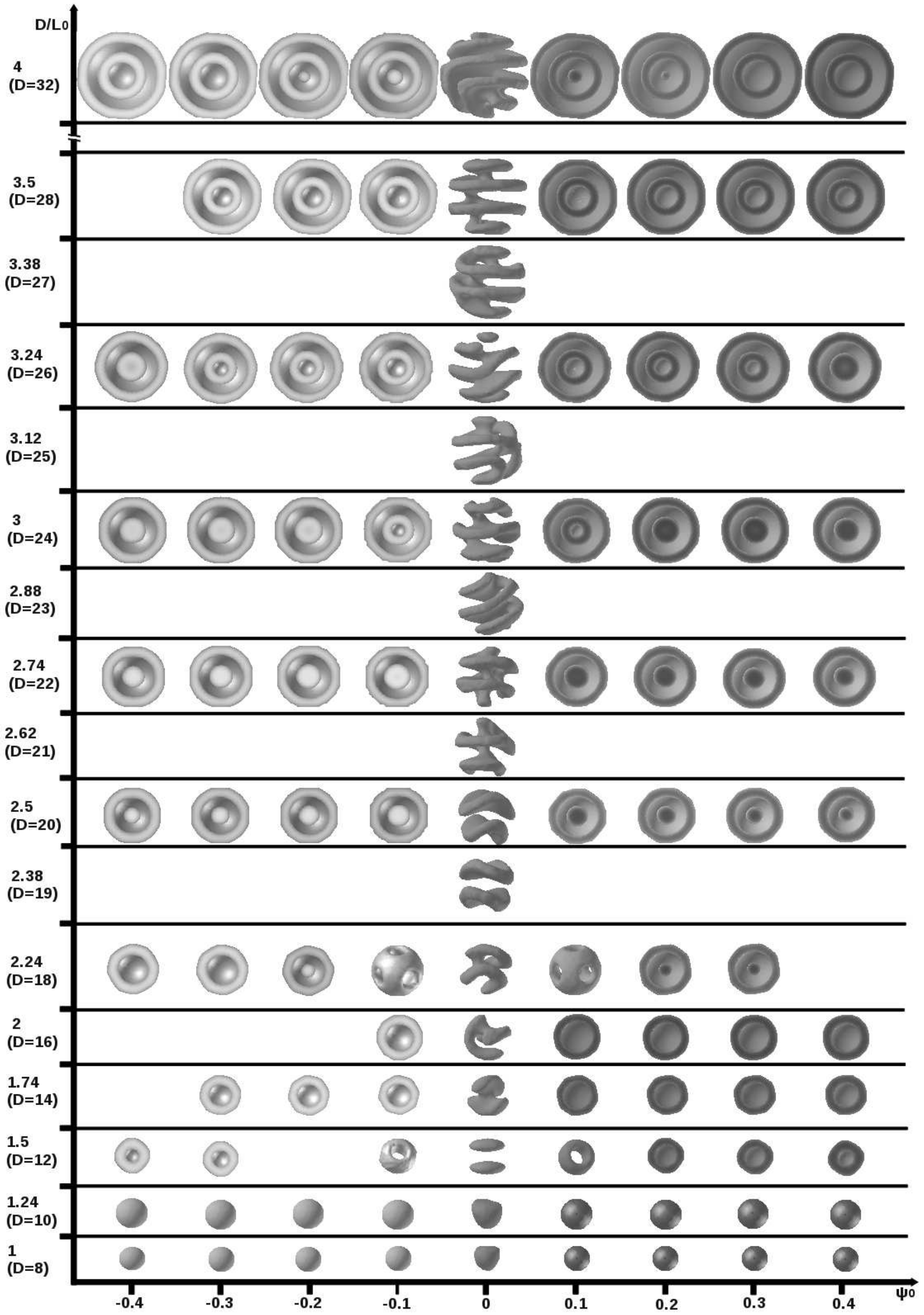

Figure 5.2: *Structure diagram of lamellae-forming diblock copolymers induced by a spherical cavities as a function of the surface field ψ_0 and the confinement D/L_0 (ratio of spherical cavity diameter D versus polymer repeated period L_0). For negative values, and positive and zero values of the surface field ψ_0 the structure diagram shows the morphologies of majority and minority blocks of the diblock copolymer, respectively. For negative and positive values of the surface field ψ_0 the symmetric lamellae shell have been cut in 1/2 to show the particle inside.*

Fig.5.2 reflect the fact, that two opposite blocks of block copolymer swap their places on left and right sizes from $\psi_0 = 0$ line. Therefore we only discuss positive and zero values of ψ_0 here (right hand side of the Fig.5.2). First we consider selective surfaces (non-zero values of ψ_0). The dominant morphology here is spherically concentric lamellae (onions). At small confinement sizes (1L_0¡ D/L_0 ¡1.24 L_0) the system forms a single spherical micelle in the middle, corresponding to concentric 1 lamellae (AB-lamellae) sequence starting from the centre). It becomes 1.5 lamellae (ABA-sequence) at confinement size 1.5 L_0, two lamellae (ABAB-sequence) at the size above $2L_0$, and increasing with a half lamellae increments. Onions were already reported in the first simulation work by[131] using Monte Carlo and observed many times ever since for various systems[56,79,138,142]They are also confirmed by simulated annealing Monte Carlo simulations in Ref.[141] for a system similar to the current work. However, the cavity size in Ref.[141] starts from $1.5L_0$, so we cannot compare our smallest sizes. We observe two non-lamellae morphologies. One is a ring structure at ψ_0=0.1 and $1.5L_0$ confinement. This can be seen as an induced cylindrical morphology. This morphology was also seen in Ref.[141] at precisely the same confinement of $1.5L_0$. Another non-bulk morphology is a perforated lamellae at ψ_0=0.1 and $2.24L_0$ confinement. Such morphology was also reported for various systems in[138,142] using dynamic density functional (self-consistent theory) simulations, as well as seen as a 'golf-ball' morphology in Ref.[145] It was also observed by CDS for spherical thin films in Ref.[79]. For a system similar to ours it was observed Ref.[141] in the same range of confinement size of $2 \div 2.5L_0$. Perforated lamellae transforms to onions at stronger surfaces (larger ψ_0), see Fig.5.2. The same occurs in Ref.[141]. Neutral confining surface ($\psi_0 = 0$) induces no onions. At smallest sizes (two bottom rows in Fig.5.2) the systems forms deformed micelles, which is expected, as neither of the blocks is preferred by the boundary. At $1.5L_0$ the systems forms 2 small parallel lamellar platelets (pills), exactly the same is seen at this confinement in Ref.[141] using a different method. As the size grows, so do the lamellae; they prefer to stay perpendicular to the confining surfaces, and as a result have various defects. At 1.74 L_0 there is one lamellae sheet, but twisted in the middle (like two orange segments joining each other in the middle at 90^o). For a stack of flat lamellae a comfortable confinement shape would be ellipsoid, as seen in Fig.2a of Ref.[142] Within a sphere the lamellae undulate in shape, forming a crisps/chips-like morphology, see our Fig.5.2 at

2.38 and 2.5 of L_0. The most typical morphology at neutral confinement is stacked lamellae with a screw disclination. This defect was also reported in Ref.[142] see Fig.2b there, and in Ref[141].

5.2.2 Cylinder forming system

In this section we consider cylindrical morphology with $f = 0.4$. The other parameters entering in Eq. 2.2 are $A = 1.5$, $B = 0.02$, $D = 0.5$, $v = 1.5$, $u = 0.5$, $\tau = 0.3$. From our previous simulations, the distance between cylinders in the bulk is found to be $L_0 \sim 7.4$ grid points.[108] Figure 5.3 shows the structure diagram of cylinder-forming diblock copolymers as a function of the confinement D/L_0 and the surface field ψ_0. As seen in the structure diagram, the first thing to notice is that the case of cylinder-forming BCPs in 3D confinement forms the most rich and complex morphologies compared to the cases of lamellae-, bicontinuous-, and sphere-forming systems.

The structure diagrams for asymmetric block copolymers are not symmetric over $\psi_0 = 0$ line, as one would expect. At small confinements the cylinder-forming block copolymer forms a single spherical micelle in the middle (denoted as S in Fig.5.3). That can be seen as induced lamellae morphology (a minimal size of concentric lamellae or onion). The region is larger for the selective surface, which prefers minority component (negative ψ_0). That is due to the fact that in the case of majority selective surface the system forms a single concentric lamella (AB-sequence from the centre), while as in the case of minority selective surface, the system forms effectively 1.5 concentric lamellae due a wetting layer at the surface (ABA-sequence from the centre) and that morphology can exist in a larger sizes. At larger sizes stronger surface selectivity is required to induce this non-cylinder morphology. That is in agreement with the general rule, which we first established in Ref.[122] Contrary to the case of symmetric block copolymer, these micelles are perfectly spherical even in small neutral confinement (close to $1L_0$). That is due to the fact that although the surface is neutral ($\psi_0 = 0$), the block copolymer molecule is not, and effectively prefers one of the block at the surface. While the size of neutral confinement increases, the system forms cylinders: first one (as an elongated micelle), then two, three and so on. These prefer to be perpendicular to the surface, and are often very short and can be seen as an induced spherical morphology. In some instances, a coexistence of longer cylinders and very short ones (deformed spheres) is observed, in all

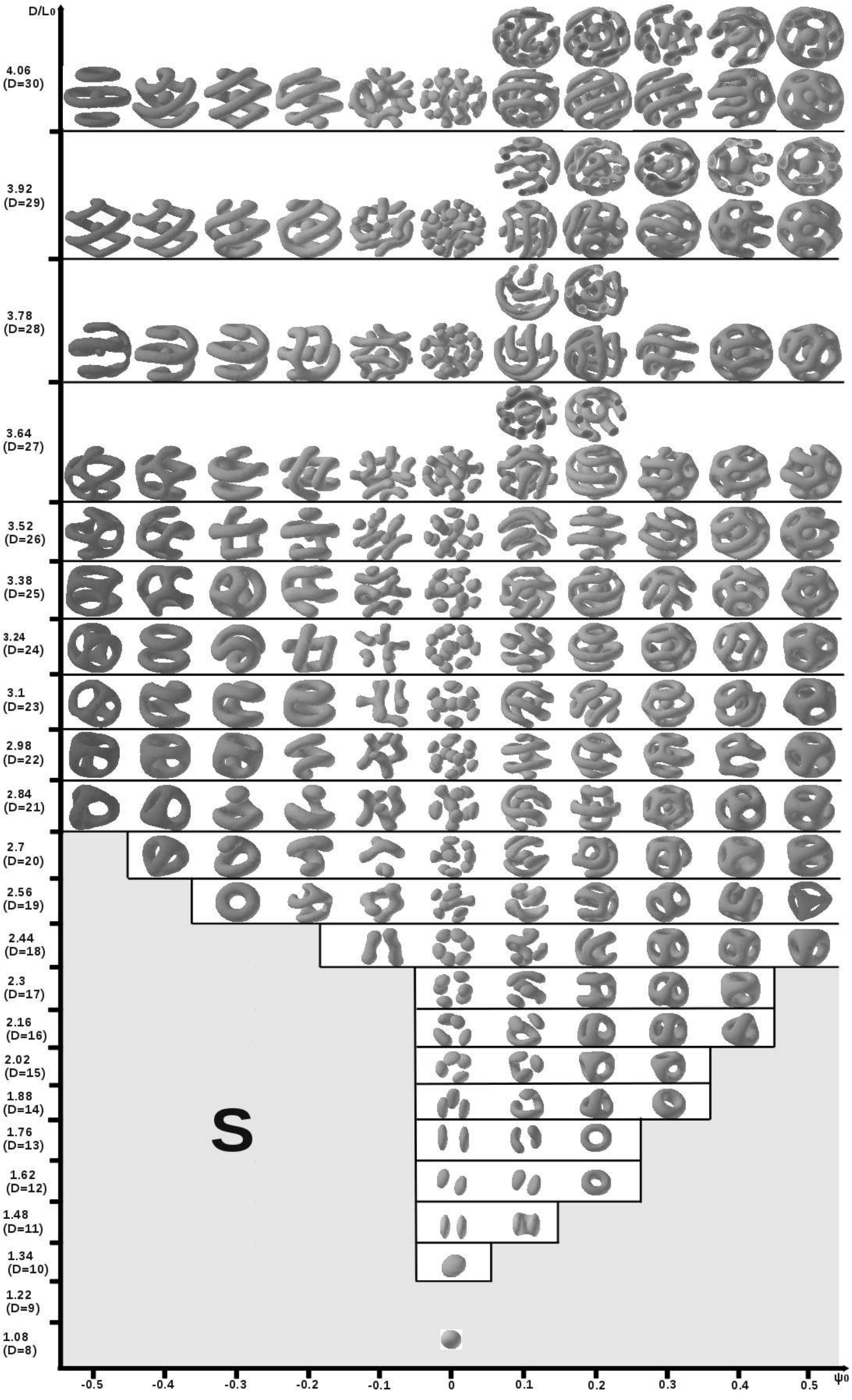

Figure 5.3: *Structure diagram of cylinder-forming diblock copolymers as a function of the surface field ψ_0 and the confinement D/L_0 (ratio of spherical cavity diameter D versus polymer repeated period L_0), obtained within a spherical cavities. The minority component of the diblock copolymer is described by dark colour. The S symbol denotes spherical structures. Some inner structures are shown above the full structures by cut views.*

cases the cylinders align perpendicular to the surface. In the case of selective surfaces, the situation is totally different: the system develops a zoo of structures made up of longer cylinders. There are two very distinct cases here. The majority of morphologies consist of cylinders, which bend towards the surface, trying to follow its curvature. The simplest example is 'two bananas' structure at ψ_0=0.1 and $D = 1.76L_0$, Fig.5.3. More complex structures include knitting balls similar to ones reported in Ref.[79], single, double and triple tori (sometimes with a sphere in the middle, like example at ψ_0=-0.5 and $4.06L_0$), which is very similar to the structure found earlier by dynamic self-consistent theory simulation in Ref.[142] , Fig.12c), single and double helices (also with a sphere in the middle). In many instances the cylinders interconnect forming network of perforations: three (example is at ψ_0=0.2 and $1.88L_0$), four ('pyramid' morphology, like an example at ψ_0=0.5 and $2.56L_0$), six ('cube' morphology, like an example at ψ_0=0.3 and $2.44L_0$). Many of these interconnected structures are defected, but several examples are defect free and rather exotic: 7 hole cage of two pentagons connected by 5 rectangles (ψ_0=0.5 and $3.1L_0$), 9 hole cage of pentagons and squares (ψ_0=0.5 and $3.24L_0$), 10 hole cage of pentagons and squares with a small spherical micelle in the middle (ψ_0=0.5 and $3.38L_0$). As before, the larger size is the stronger surface selectivity is required to induce certain morphology: compare, for instance, structures at (ψ_0=0.2, $1.76L_0$) and (ψ_0=0.3, $1.88L_0$) or (ψ_0=0.2, $1.88L_0$) and (ψ_0=0.3, $2.02L_0$). Many of our defect free structures (such as 'two bananas', tori, perforated cages, helices) have been also reported by self-consistent field theory calculations of cylinder-forming diblock copolymer melts in spherical nanopores,[140,147] which also uses self-consistent field theory calculations, does not report such structures apart of a *'cube'* morphology and multiple spherical micelles morphologies. In contrast, Ref.[140] reports many structures of such various sizes with surprisingly cubically-arranged patterns in the vicinity of the sphere wall. Patterns can be sometimes observed due the discretization of the spherical boundary on a cubic grid. The second class of structures is observed when the surface weakly prefers minority component, ψ_0=-0.1. In this case the cylinders bend very differently, not following the spherical confinement curvature, but connecting with both ends to a thin wetting layer of minority component on the spherical confinement wall. They look like collection of 'handles' stuck on the internal surface of the sphere.

When the system size increases the number of cylinder layers increases as well, see Figure 5.4. The internal layers represent the same structures as observed in the spherical pores of smaller size (compare top row in Figure 5.4 with structures of small sizes in Figure 5.3). In the case of nearly neutral cavity wall the structure consists not of concentric cylinder layers but of a mixture of cylinders, many oriented close to the radial direction (see block diamonds in Figure 5.4). It should be noted that the structures in Figure 5.3 are often kinetically trapped (as it is often the case in experimental practice). They can be moved toward equilibrium morphologies with the addition of noise.

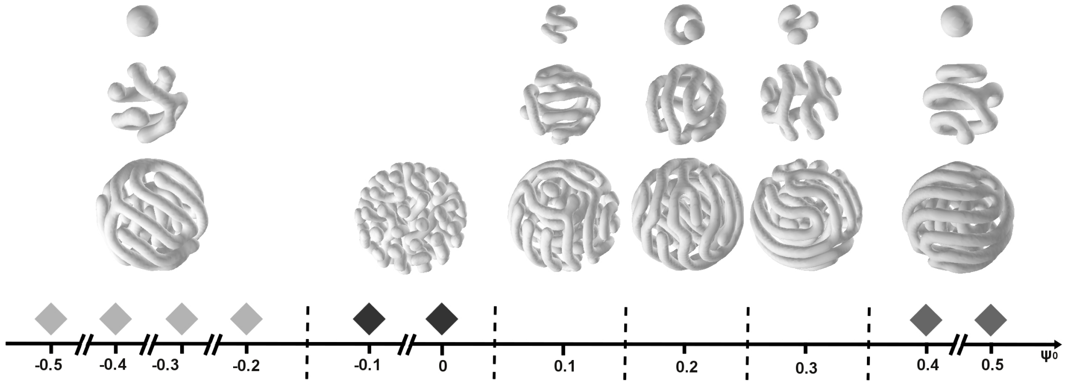

Figure 5.4: *Simulation results for a cylinder-forming diblock copolymer system at different surface field ψ_0 and D/L_0=5.95 (D=44). From the bottom to the top, the picture describes: the total system; the middle layer; and the inner layer.*

Example is shown in Figure 5.5, which represent the defect-free structure of tori and small spheres.

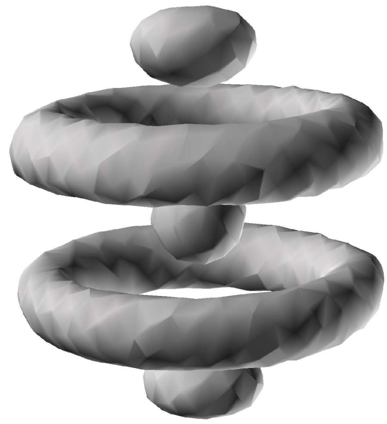

Figure 5.5: *Toroid structures with three spheres obtained after 200. 000 time steps without noise as result of the system at ψ_0=-0.4 and D/L_0=3.92 (D=29) simulated with noise at η=0.03.*

5.2.3 Bicontinuous forming system

In this section we consider bicontinuous morphology with $f = 0.44$. The other parameters entering in Eq. 2.2 are $A = 1.5$, $B = 0.02$, $D = 0.5$, $v = 2.3$, $u = 0.38$, $\tau = 0.33$. From our previous simulations, the distance between cylinders in the bulk is found to be $L_0 \sim 7.5$ grid points.[79] Figure 5.6 shows the phase diagram of bicontinuous-forming diblock copolymers obtained within spherical confinement as a function of the surface field ψ_0 and the ratio D/L_0, where D is the spherical cavity diameter and L_0 is the polymer repeated period.

Overall motif of the structure diagram is similar to the one for cylinder- or lamellae-forming systems: close to $\psi_0 = 0$ line the structures tend to be perpendicular to the surface of the spherical cavity while away from $\psi_0 = 0$ line the structures form concentric layers of various structures. The diagram is not symmetric with respect to $\psi_0 = 0$, as it is expected for a non-symmetric molecule. At small confinement and negative ψ_0 ($\psi_0 < -0.2$ for smallest confinement) the system is shifted into the spherical micellar phase (or simple concentric lamellae). The situation is similar to the one for cylinder-forming system (compare Figures 5.3 and 5.6).

In the opposite corner of the diagram (small confinement size and $\psi_0 > 0$) there are no spherical micelles of the opposite block. Instead the system forms a single perforated lamellae layer.

Then the surface does not prefer any block ($\psi_0 = 0$) or slightly preferential for the minority block the structures consist of interconnected cylinders when are mostly perpendicular to the wall of the cavity. The most typical type of interconnection is a tripod (see snapshot for $\psi_0 = -0.1$, $D/L_0 = 2$), a characteristic feature of a gyroid structure. For “neutral“ surface ($\psi_0 = 0$) and small confinement size ($D/L_0 \sim 2$) some of the short cylinders are parallel to the surface, similar to the small confinement in the case of cylinder-forming system, Figure 5.3. Such asymmetry is again due to the asymmetry of the molecule.

For larger diameters and surfaces which prefer one of the blocks the system forms perforated lamellae. These are formed either as single or multiple layers or mixed structures. For instance, for confinement around $2 < D/L_0 < 3$ and positive ψ_0 a perforated lamellae surrounds a spherical droplet. Similar structures but for negative ψ_0 are found at larger sizes $3.5 < D/L_0 < 4$. This asymmetry of the diagram is also

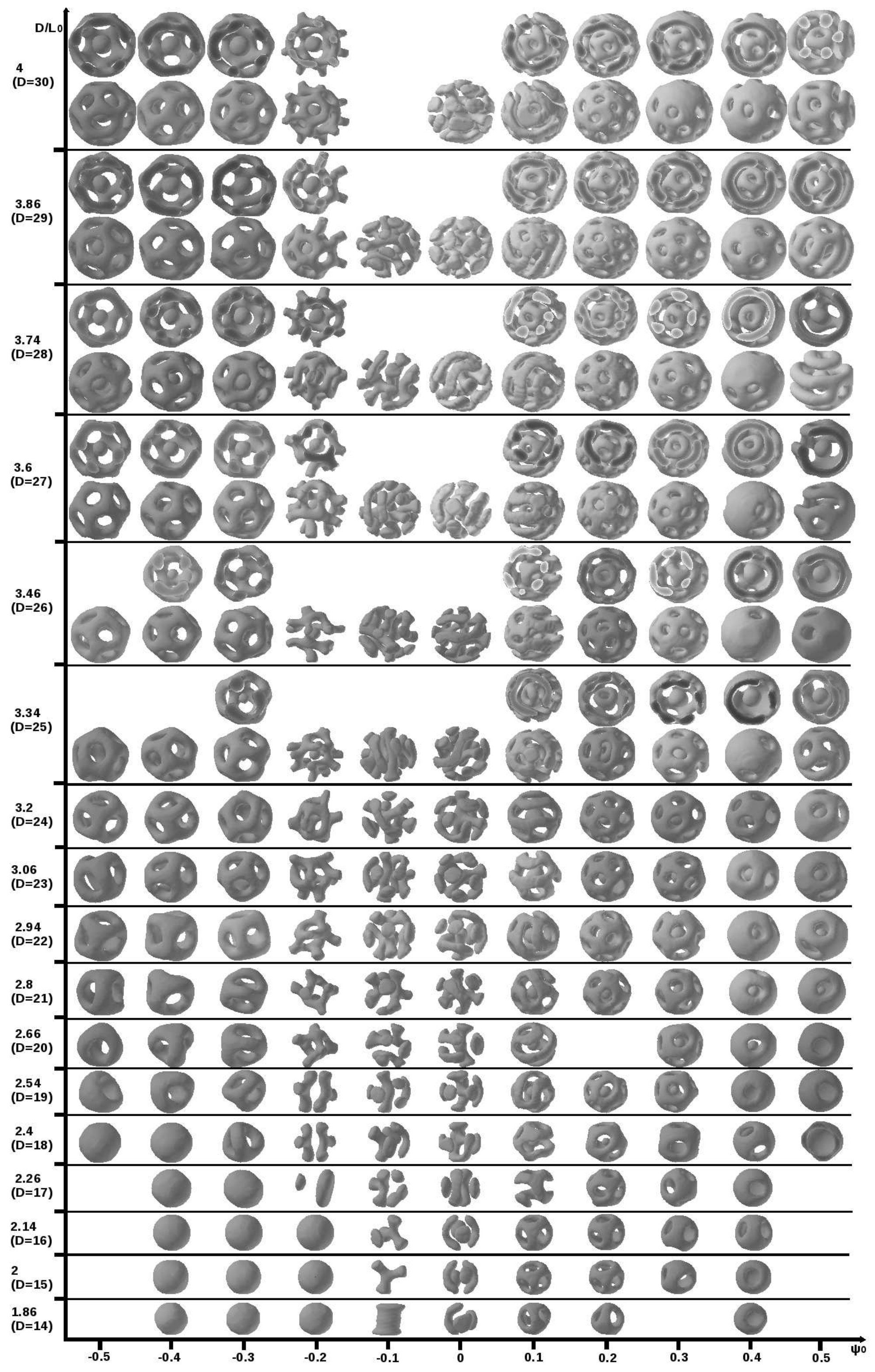

Figure 5.6: *Structure diagram of bicontinuous-forming diblock copolymers as a function of the surface field ψ_0 and the ratio D/L_0 (spherical cavity diameter D versus polymer repeated period L_0), obtained within a spherical cavities. Only the morphology of the minority component of the diblock copolymer are shown, and some inner structures are shown above the full structures by cut views.*

due to the asymmetry of the block copolymer molecule. The perforated lamellae have often defects and the shape of this morphology is different for positive and negative ψ_0. For positive ψ_0 perforated lamellae form a spherical shell with perforations, while for negative ψ_0 the structure looks more like a cage. That is due to the fact, that for $\psi_0 < 0$ there is a minority block layer next to the surface, which reduces amount of the minority block to form the structure inside resulting in a cage-like appearance. There are several special structure. For $\psi_0 = 2$ and larger sizes $3.74 < D/L_0 < 4$ the structure consist of a perforated lamellar cage with necks extending towards the minority layer next to the surface of the spherical cavity. For $\psi_0 = 5$ and larger sizes $3.74 < D/L_0 < 4$ the system forms the outer shell which is a coexistence of perforated lamellae and cylindrical phase.

5.2.4 Sphere forming system

The last system in the present study is a sphere-forming block-copolymer. The diblock copolymer chosen in this section has a volume fraction of a minority-block $f = 0.4$. The other parameters entering in Eq. 2.2 are $A = 1.5$, $B = 0.01$, $D = 0.5$, $v = 2.3$, $u = 0.38$, $\tau = 0.2$.[79] From our previous bulk calculations, the polymer repeated period $L_0 \sim$ is found to be 11 grid points.[79] The diagram in Figure 5.7 summarizes the results of sphere-forming diblock copolymers confined in a closed empty spherical cavity as a function of the selective surface ψ_0 and the confinement size D/L_0. As is seen in the Figure 5.7, the structures are very simple compared to the previous sections. The diagram is not symmetric with respect to ψ_0=0 line due to the asymmetry of the molecule. At small sizes the system forms a single sphere in the middle (structures denoted as S in Figure 5.7). This structures look like a single concentric lamellae or onion. As it was also described in the cylinder-forming section, the region is larger for the selective surface which prefers minority components (negative ψ_0). In the case of selective surface toward the majority component (positive ψ_0) the structure ψ_0 is a single concentric lamellae, while in the case of surface selective toward the minority component the structure is 1.5 concentric lamellae due a wetting layer at the outer surface. When the size of the confinement increases (D/L_0=1.08 and D/L_0=1.28) two spheres appear. For larger size and ψ_0=0 the number of the droplets increase: four, seven, and so on. The diagram in Figure 5.7 shows that increasing the confinement size

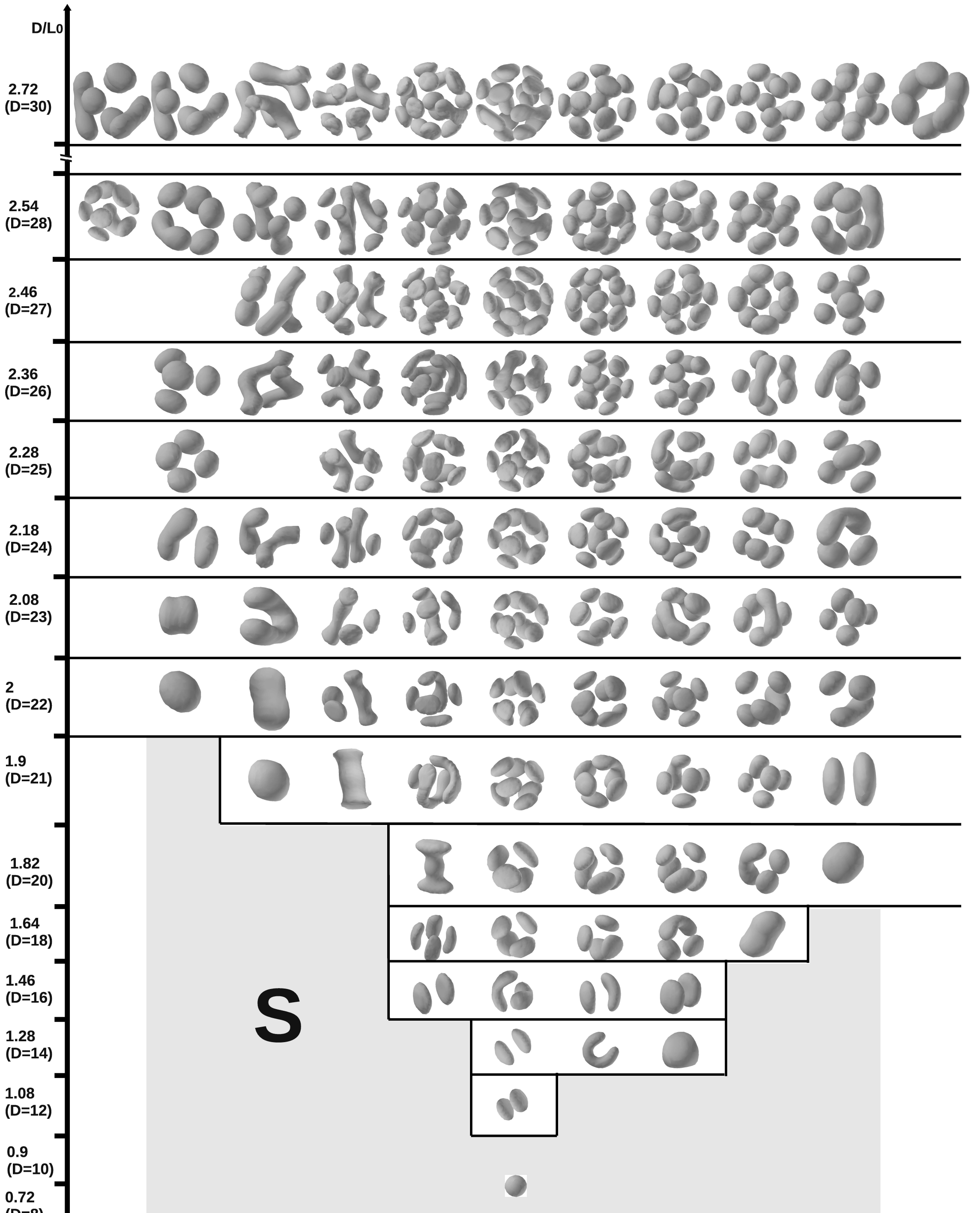

Figure 5.7: *Structure diagram of sphere-forming diblock copolymers obtained within a spherical cavities as a function of the selective surface* ψ_0 *and the confinement* D/L_0 *(ratio of spherical cavity diameter* D *versus polymer repeated period* L_0*). Only the morphology of the minority component (A-blocks) of the diblock copolymer are shown. The S symbol denotes spherical structures.*

two layer structures are formed. Away from the ψ_0=0 line the system can be shifted to a coexistence of cylinders and spheres. In the case surface preferring the majority block the short cylinders bend along the surface (e.g. D/L_0= 2.18 and ψ_0=0.4). In the opposite case of the minority block being selected by the surface, the short cylinders span the whole cavity and connected to the wetting layer near the outer surface (e.g. D/L_0=1.9, ψ_0=-0.2). In some cases the cylinder form "handles" in order to avoid crossing each other (e.g. D/L_0=2.36, ψ_0=-0.3). In general the structural behaviour is similar to the sphere-forming phase between two concentric surfaces.[79]

5.3 Conclusion

We performed cell dynamics simulations to study self-assembly of lamellae-, cylinder-, bicontinuous-, and sphere-forming diblock copolymer confined in spherical cavities. Three different cases are chosen to represent systems in which the surface is selective toward the majority component (positive ψ_0), the minority component (negative ψ_0), non-selective to either of the blocks ψ_0=0. Rich and complex copolymer morphologies have been found in this 3-D confinement, depending on the size of the confinement, the composition of the copolymer and the selectivity of the surface. Our results clearly demonstrate that the geometry and the size of the confining space have a pronounced effect on the structure of the self-assembled morphologies. The self-assembled structures of lamellae-forming diblock copolymers with positive ψ_0 is similar to those observed for negative ψ_0. However, the morphologies obtained with non-selective surface are different. The self-assembled structures of cylinder-, bicontinuous-, and sphere-forming diblock copolymers form different structures (to some extent) for positive ψ_0 and negative ψ_0. The difference is larger for larger ψ_0. While some structures have been found in the previous studies[140–142], CDS allowed to perform the largest parameter search so far. The relative easiness of the CDS method can help to use it as a precursor for more heavier techniques in order to investigate systems confined in complex geometries.

Chapter 6

Summary

6.1 Summary of the Investigation

The realization of more efficient microelectronic components, nanowires,[14–17], nanopores, [18,148], and vesicles as drug delivery[22,23] are crucial in the technological and scientific world. One of the main limitations in the manufacture of integrated circuits is the difficulty in scaling the conventional lithographic techniques used to fabricate devices.[12] The use of block copolymers (BCPs) in the lithographic process is one promising approach to achieve this scaling because BCP feature sizes are typically 5-100 nm.[2,149] Due to the great nanotechnology interest, the control and lateral ordering of the microdomains is essential. Application of external fields, such as surface fields[150], shear flow[80], and electric fields[24] can tailor desired BCP nanostructures and improve their long range order. Also the nanoconfinement of block copolymers is an interesting method to produce novel morphologies,[13] that can potentially serve as building material for intelligent nanosize bioreactors and vesicles as drug delivery vehicles or self regulating diagnostic devices.[22,23]

In this thesis it has been performed a 3-dimensional study of standing up cylinders of block copolymers in two different types of confinement (1-dimensional), computationally emulated: topographical and chemical patterns.

Diblock copolymer cylinder-forming thin films have also been investigated confined between two parallel selective walls, by changing the value of the surface field and the value of the film thickness.

Moreover, self-assembly of lamellar, cylinder-, bicontinuous-, sphere-forming under spherical confinement are studied by changing the confinement size and the selective surface.

6.1.1 Conclusion of Chapter 3

In Chapter 3 the problem of the order and packing symmetry control of diblock copolymer microdomains within 1-dimensional confinement (thin films) for lithographic applications has been addressed. Among the various approaches for controlling the long range order of block copolymer thin films there are the surface topography and chemical pattern methods.[4,53] In Chapter 3, it has been performed 3-dimensional simulations on the self-assembly of cylinder-forming AB-diblock copolymer thin films confined within square, rectangular and diamond-shape patternes of various sizes, realized computationally, emulating the two experimental methods mentioned above: surface topography and chemical patterning.

In order to computationally reproduce the topographic well we modelled it as a lateral confinement with appropriate geometries and with short-block (A-block) attraction. The top and bottom surface have no preference for any block. Self-assembly of diblock copolymers in these lateral confinements gives rise to short block standing-up cylinders on a surface neutral to both blocks, and embedded in a long-block (B-block) matrix.

In order to model the chemical pattern substrate we imposed short-block attraction on a flat surface drawing appropriate geometries. On the selective surfaces the short- and long-blocks form parallel lamellae layers preferentially located at the bottom and at the top, respectively; while in the neutral inner area short-blocks form cylinders perpendicular to the thin film plane, embedded in a long-block matrix. In chemical pattern substrates the edge of the lamellae layer acts as a soft wall directing the self-assembly of microdomains similar to the confining lateral wall of a topographical pattern.

Our study has been inspired by the 2-dimensional self-consistent-field-theory (SCFT) simulations conducted by Hur et al.[4], in which they have shown that the lateral confinement of cylinder-forming diblock copolymer thin films within square wells can induce square packing. Our study has also been inspired by Xu et al.'s experimental findings, where the order and packing symmetry of the self-assembly of cylinder-forming BCP thin films, within lateral confinement induced by chemical patterns, is affected by the size and shape of the confinement.[53]

We confirmed that pattern edges, in both topographical and chemical confinement, direct the phase separation, orientation, and symmetry packing of BCP microdomains, as in the computational[4] and experimental findings[53]. Both square topographic and chemical confinement types with small size $\sim 2L_0$ exhibit their influences in inducing square order with single grain order, while larger square confinement sizes $\sim 9L_0$ give rise to hexagonal packing with multi-grain order, as observed in the bulk. However, our simulations emphasize the role of topographic and chemical pattern in an intermediate square confinement size $\sim 3L_0$, where it is demonstrated that soft-wall confinement induces less square order than hard-wall confinement. In this intermediate size commensurate with a 3 x 3 array of cylinders the square packing is stable, while in a 4 x 4 array of cylinders the square packing is unstable and appears as a transient structure that looks like a twisted hexagonal phase. The latter concept is in agreement with 2D SCFT findings[4]. However in our 3D simulations we modelled both topographic and chemical pattern confinement, which is not possible in 2D SCFT simulations.[4] We also performed simulations in rectangular boxes, and found that single domains align better along the longer edges. The latter result is in agreement with experimental findings[53], however our kinetic analysis suggested a different explanation: longer sides offer a more comfortable fitting of the microdomanis in their hexagonal symmetry.

6.1.2 Conclusion of Chapter 4

The focus of Chapter 4 is the study of shear-induced domain alignments and morphological transitions of diblock copolymers in thin films (1D confinement), for the fabrication of nanoscale patterns. To model thin films in this chapter we confined cylinder-forming AB-diblock copolymers between two parallel surfaces with different surface fields and in different confinement spaces. The morphologies obtained under A-, or B-, or neutral surface fields are different, for instance: wetting layer, parallel cylinder, perpendicular cylinder, perforated lamellae, lamellae, coexistence of perpendicular and parallel cylinder, and coexistence of parallel cylinder and perforated lamellae. Similar morphologies have been found in Lyakhova et al.'s computational study.[89]

In this chapter we were interested in driving the self-assembly of AB-diblock copolymer thin films, and to do so some of our previous thin films morphologies were manipulated by shear flow.

We found that shear flow on an ultra thin film layer, around one polymer period thickness $\sim L_0$, of cylinders perpendicular to the thin film plane improves hexagonal packing of BCP microdomains perpendicular to the shear direction (hexagonal packing is in the plane of the shear application). Only a shear flow value above a certain critical level causes a phase transition from perpendicular cylinders into two half cylinder layers parallel to the thin film plane along the shear direction, with hexagonal packing microdomains in the plane perpendicular to the shear flow direction. Similar results have been found experimentally by Kim et al. In their case, a thin film of triblock copolymer polystyrene (PS)-polybutadiene (PB)- polystyrene (SBS) forms hexagonal packing of cylinders with their axes perpendicular or parallel to the plane as function of solvent evaporation rate, and not shear field as in our case.[109] Computationally, Arya also found hexagonal packing in a plane perpendicular to the shear direction for thicker films, with cylinders aligned parallel to each other along the shear direction.[97]

We also investigated the shear re-alignment effect on an ultra thin film layer, around one polymer period thickness $\sim L_0$, of cylinders parallel to the thin film plane, which after shearing are perfectly aligned along the shear direction. This result is in agreement with Angelescu et al.'s experimental findings, who obtained long-range ordering of cylindrical nanodomains aligned to the shear flow direction in thin film.[98] Re-alignment, after shearing, of a layer of parallel cylinder to the thin film plane was also obtained in the computational work of Arya et al.[97]

We observed that shear flow can also improve hexagonal packing in perforated lamellae ultra thin films of around one polymer period thickness $\sim L_0$. Again, in this case increasing shear above a certain value causes phase transition, from perforated lamellae layer into lamellae layer.

However, in the case of two layers $\sim 2L_0$ of perforated lamellae an increased shear above a certain critical value causes phase transition into two layers of cylinders parallel to the thin film plane and aligned along the direction of the shear flow, but with hexagonal packing in the plane perpendicular to the shear flow direction. Hexagonally perforated lamellae-to cylinder transition in a diblock copolymer thin film has also been found in Ly et al.'s computational work but in their case it was under an electric field.[99]

6.1.3 Conclusion of Chapter 5

In Chapter 5 we focused on the self-assembly of block copolymers within a 3-dimensional (3D) spherical confinement for the realization of nanocontainers, for instance as drug delivery vehicles. Spherical confinement (3D) differs from that in thin films (1D) and in cylinders (2D) by the presence of a confining surface along each axis, and the consequent BCP frustration causing the development of concentric structures or the presence of required defects. In Chapter 5 a systematic study on self-assembled microstructures of lamellae-, cylinder-, bicontinuous-, sphere-forming diblock copolymers under spherical confinement is presented. We investigated the effects of confinement space and neutral, A-selective (long-block), and B-selective (short-block) surfaces on the self-assembly of AB-diblock copolymer.

We found that the self-assembly of cylinder-forming diblock copolymers under 3D spherical confinement gives rise to numerous morphologies. In fact, the self-assembled cylinder-forming BCP structures under an A-selective surface are clearly different from those observed under a B-selective surface, and morphologies under a neutral surface are also different from those under either an A- or B-selective surface. Chen et al.[140] also performed simulations on self-assembled cylinder forming diblock copolymers under 3D spherical confinement but in their case with a more asymmetric BCP composition. In fact, they found more homogeneity in the phase diagram: self-assembled structures under neutral and A-attractive surface fields are similar, but phase behaviour under B-attractive surface fields are different from those observed under neutral and A-attractive surface fields. Some of our cylinder-forming structures are also in agreement with Yang's simulations[112], such as: toroids with a sphere; single helice with a sphere; and double helices with a sphere. However, to obtain the latter morphologies Yang and coworkers exploited the combination of cylinder-forming AB diblock copolymers and C-homopolymers confined in spherical cavities, where the addition of C-homopolymers is credited for its role in the control of the self-assembled morphology.

In contrast, the case of lamellae-forming BCPs within a spherical confinement clearly shows its homogeneity: morphologies obtained under B- and A-selective surfaces are similar, but are different from those phase behaviours found under a neutral surface. We show the symmetry of the lamellae-forming structure diagram, whose morphologies found agreement with other computational and experimental work. Our concentric lamellae are similar to those found experimentally by Thomas and his team[56] for a lamellae-forming system; and our concentric lamellae are also similar to the onion like structures of alternating A and B layers found computationally by Fraaije and coworkers for a symmetric polymer. Also, Yu et al.'s[141] simulations for a symmetric AB diblock copolymer in 3D spherical confinement confirm concentric-spherical lamellae (onion like) systems in the strong surface preference limit; and also a single helice structure with perpendicular lamellae, in agreement with our lamellae-forming structures in neutral surface.

The self-assembly case of sphere-forming block copolymers within spherical confinement gives rise to a simple structure diagram. We demonstrated that the morphologies under a B-selective surface are different to those morphologies under an A-selective surface.

Most of these microstructures are center-symmetric, and exhibit a phase transition from the droplet to sphere system when the selective surface becomes stronger. We also found that our sphere-forming system forms a layer of spheres or droplets close to the 3D spherical confinement, which is agreement with another computational work in Ref.[79], but with a different confinement system, a sphere-forming diblock copolymers confined within a 3D spherical cavities with a inner particle.

Finally, bicontinuous-forming diblock copolymers under 3D spherical confinement is the last system we analyzed. We found that the phase behaviour under a B-selective surface is different from that under an A-selective surface, but morphologies obtained under a B-selective surface are similar to those obtained under a neutral surface. Our perforated lamellae structures find confirmation in the experimental work of Thomas and coworkers[56], related to a bicontinuous-forming diblock copolymer. Confirmation comes also from a computational study conducted in Ref.[138] for bicontinuous-forming diblock copolymers.

6.2 Future outlook

Overall, the current findings provide insights into how lateral confinement, shear, and 3-dimensional confinement can be used to tailor structure of diblock copolymers. Hopefully these findings can be useful for future studies, for instance design of new experiments, and computer aided design of new advanced materials.

Appendix A

Fortran codes for Voronoi diagram application

In this thesis, Voronoi diagram has been used to better visualize orientation and lattice defects in hexagonal symmetry of diblock copolymer (BCP) microdomains in thin films. Voronoi diagram is constructed by drawing a polygon around each microdomain, where the number of polygon sides is equal to the number of neighbors of the central microdomain. In a Voronoi diagram, 6-fold-coordinated sites represents hexagonal packing, typical for BCP cylinder-forming in bulk, while 5-fold and 7-fold-coordinated sites represent defects. A polygon around each microdomain is obtained by drawing the bonds connecting a microdomain with all its neighbors. Then, perpendicular bisectors of these bonds intersect to form a polygon.[53] In order to use Voronoi diagram, it is necessary to elaborate a data file with the center of mass of each microdomains. For this scope, in this thesis a few Fortran codes have been elaborated, which are able to detect the center of mass of our 2 dimensional (2D) BCP microdomains, obtained from our 3D BCP structure. The main idea is to cut one layer, parallel to the thin film plane, of our 3D BCP structure, and also to cut the confinements within self-assembly block copolymers have been grown. The resulting morphology is a layer where the original 3D confined cylindrical microdomains embedded in a long-block matrix became 2D spherical short-block microdomains still embedded in a long-block matrix. Then, the identification of the boundaries of each 2D spherical short-block microdomain in the long-block matrix, through a specific algorithm that will be explained in the next pages, leads to the detection of the center of mass of each 2D spherical short-block microdomain. Each microdomain center of mass is calculated as an average of the coordinate values of its microdomain boundary points. The above idea have been implemented in a few Fortran codes which are presented in the next pages in the right order that they need to be used.

```
!*******************************************************************
!*******************************************************************
!**
!** info.in: Input file that needs to be set with the information
!** regarding the sizes (Nx,Ny,Nz) of the 3D confined BCP
!** structure. Input file also needs information
!** about the new dimensions of the new 2D BCP structure
!** without confinements, obtained from the original 3D one:
!** Nx_Inf and Nx_Sup represent the new lower and upper limits
!** of the coordinate in x-direction, the same for Ny_Inf and
!** Ny_Sup, and for Nz_Inf and Nz_Sup, in y- and z-coordinates,
!** respectively.
!** The last information 'Value limite volume' is related
!** to the isosurface level. This file is an input file
!** for all below fortran codes.
!**
!** Data: September 2011.
!** Location: Preston, UK.
!** Authors: Roberta Dessi & Marco Pinna.
!**
!********************************************************************
!********************************************************************

'Value Nx'
34
'Value Ny'
34
'Value Nz'
5
'Value Nx_Inf'
3
'Value Nx_Sup'
```

```
31

'Value Ny_Inf'

3

'Value Ny_Sup'

31

'Value Nz_Inf'

1

'Value Nz_Sup'

1

'Value limite volume'

-0.18d0
```

```
!***********************************************************
!***********************************************************
!**
!** cut_2D.f90: A program to generate a 2-dimensional
!** BCP structure starting from a 3-dimensional one. This
!** program takes in input a 3D cylindrical
!** short-block microdomains standing-up on the thin
!** film plane, embedded in long-block matrix, and
!** within confinements. The output of this program is a
!** 2D spherical short-block microdomains,
!** embedded in long-block matrix and still within
!** confinements. The selected layer is parallel
!** to the thin film plane.
!**
!** Data: September 2011.
!** Location: Preston, UK.
!** Authors: Roberta Dessi & Marco Pinna.
!**
!************************************************************
!************************************************************

      program cut_2D

      implicit none

      integer Nx,Ny,Nz
      integer Nx_Inf,Nx_Sup
      integer Ny_Inf,Ny_Sup
      integer Nz_Inf,Nz_Sup
      integer i,j,k
      character*80 label
      double precision value
```

```
      double precision Px(0:600,0:600,0:600)

      open(unit=13,file='info.in',status='old')

!*    Reading of the input data from info.in

      read(13,*) label
      read(13,*) Nx
      read(13,*) label
      read(13,*) Ny
      read(13,*) label
      read(13,*) Nz
      read(13,*) label
      read(13,*) Nx_Inf
      read(13,*) label
      read(13,*) Nx_Sup
      read(13,*) label
      read(13,*) Ny_Inf
      read(13,*) label
      read(13,*) Ny_Sup
      read(13,*) label
      read(13,*) Nz_Inf
      read(13,*) label
      read(13,*) Nz_Sup
      read(13,*) label
      read(13,*) value

      open(unit=11,file='data_input',status='old')
      open(unit=12,file='output_cut_2D',status='unknown')

      Px(:,:,:)=0.0d0
```

```
!*    Reading of the order parameter components
!*    from file data_input

      do i = 1, Nx
       do j = 1, Ny
        do k = 1, Nz

          read(11,*)  Px(i,j,k)

        end do
       end do
      end do

!*    Elimination of the order parameter components
!*    for the coordinates k > 1, z-direction,
!*    set as the tickness section of 3D
!*    BCP thin film structure.

      do i = 1, Nx
        do j =  1, Ny
          do k = 1, 1

           write(12,*)  Px(i,j,k)

          end do
        end do
      end do

      close(11)
      close(12)

      end program
```

```
!************************************************************
!************************************************************
!**
!** cut_wall.f90: A program that takes in input
!** the confined 2D spherical short-block microdomains,
!** embedded in long-block matrix.
!** The output of cut_wall.f90 is still the
!** 2D spherical short-block microdomains,
!** embedded in long-block matrix, but without
!** confinements.
!**
!**
!**
!** Data: September 2011.
!** Location: Preston, UK.
!** Authors: Roberta Dessi & Marco Pinna.
!**
!***********************************************************
!***********************************************************

      program cut_wall

      implicit none

      integer Nx,Ny,Nz
      integer Nx_Inf,Nx_Sup
      integer Ny_Inf,Ny_Sup
      integer Nz_Inf,Nz_Sup
      integer i,j,k
      character*80 label
      double precision value
      double precision Px_new(0:600,0:600)
```

```
      double precision Px(0:600,0:600)

      open(unit=13,file='info.in',status='old')

!*    Reading of the input data from file info.in

      read(13,*) label
      read(13,*) Nx
      read(13,*) label
      read(13,*) Ny
      read(13,*) label
      read(13,*) Nz
      read(13,*) label
      read(13,*) Nx_Inf
      read(13,*) label
      read(13,*) Nx_Sup
      read(13,*) label
      read(13,*) Ny_Inf
      read(13,*) label
      read(13,*) Ny_Sup
      read(13,*) label
      read(13,*) Nz_Inf
      read(13,*) label
      read(13,*) Nz_Sup
      read(13,*) label
      read(13,*) value

      open(unit=12,file='output_cut_2D',status='old')
      open(unit=11,file='output_cut_wall',status='unknown')

      Pxi(:,:)=0.0d0
```

```
!*    Reading of the input order parameter
!*    components from file output_cut_2D

      do i = 1, Nx
       do j = 1, Ny

        read(12,*)  Px(i,j)

       end do
      end do

!*    Selection of the order parameter values
!*    excluding the wall coordinates

      do i = Nx_Inf, Nx_Sup
       do j =Ny_Inf, Ny_Sup

        Px_new(i,j) =  Px(i,j)

       end do
      end do



!*    Attributing value zero to the wall coordinates
!*    previously excluded in order to work, for simplicity,
!*    from now on with a system with the original
!*    size Nx and Ny.

      do i = 1, Nx
       do j = 1, Ny

         if (Px_new(i,j)  .NE. 0 )  then
```

```
    write(11,*)  Px_new(i,j)

   else

    Px_new(i,j)  = 0
    write(11,*)  Px_new(i,j)
    write(90,*)  Px(i,j),i,j

    end if

 end do
end do

close(11)
close(12)

end program
```

```
!************************************************************
!************************************************************
!**
!** volume.f90: A program that takes in input
!** a layer of 2D spherical short-block microdomains,
!** embedded in long-block matrix, and gives in
!** output a file where the coordinates of
!** 2D spherical short-block microdomains
!** are set with label '1', and the coordinates of
!** the long-block matrix are set with label '0'.
!** The distinction of the coordiantes in label '0'and '1'
!** will be useful from now on to detect
!** the boundaries of each 2D spherical short-block
!** microdomain embedded in the long-block matrix.
!**
!** Data: September 2011.
!** Location: Preston, UK.
!** Authors: Roberta Dessi & Marco Pinna.
!**
!*************************************************************
!*************************************************************

      program volume

      implicit none

      integer i,j,k
      integer Nx,Ny,Nz
      integer Nx_Inf,Nx_Sup
      integer Ny_Inf,Ny_Sup
      integer Nz_Inf,Nz_Sup
      double precision Pxi(0:600,0:600)
```

```
      double precision value
      character*80 label

      open(unit=13,file='info.in',status='old')

!*    Reading of the input data from file info.in

      read(13,*) label
      read(13,*) Nx
      read(13,*) label
      read(13,*) Ny
      read(13,*) label
      read(13,*) Nz
      read(13,*) label
      read(13,*) Nx_Inf
      read(13,*) label
      read(13,*) Nx_Sup
      read(13,*) label
      read(13,*) Ny_Inf
      read(13,*) label
      read(13,*) Ny_Sup
      read(13,*) label
      read(13,*) Nz_Inf
      read(13,*) label
      read(13,*) Nz_Sup
      read(13,*) label
      read(13,*) value

      open(unit=22,file='output_cut_wall',status='old')
      open(unit=25,file='output_volume',status='unknown')

      Pxi(:,:)=0.0d0
```

```
!*    Reading of the input data of the order parameter
!*    components from file output_cut_wall

      do i=1, Nx
       do j=1, Ny

        read(22,*) Pxi(i,j)

!*      Distintion of the coordinates belonging
!*      to the short- or long-block copolymer: values of the
!*      order parameter less than a specific isosurface level,
!*      evaluated with a visual program, belongs
!*      to the short-block microdomains and their coordinates
!*      are set to '1'.

        if (Pxi(i,j) .LE. value)  then

         Pxi(i,j) = 1.0d0

!*       Checking if the algorithm is working properly and visualizing it
!*       with gnuplot program

         write(90,*) Pxi(i,j),i,j

        else

!*      Otherwise, coordinates with values of the
!*      order parameter greater than a specific isosurface level,
!*      belonging to the long-block matrix,
!*      are set to '0'.
```

```
    Pxi(i,j) = 0.0d0


   end if
    write(25,*) Pxi(i,j),i,j


  end do
 end do


 end program
```

```
!*****************************************************
!*****************************************************
!**
!** boundary.f90: A program which takes in input a
!** file with values '1' and '0' for short- and long-block
!** points, respectively. The output file will have
!** values 1 for the boundary points of 2D spherical short-
!** block microdomains, and values 0 for long-block
!** points and for the short-block points inside
!** a 2D spherical short-block microdomain. A boundary point
!** is defined as a point which have at least one first
!** or second neighbour with value '0'.
!**
!**
!** Data: September 2011.
!** Location: Preston, UK.
!** Authors: Roberta Dessi & Marco Pinna.
!**
!*****************************************************
!*****************************************************

      program boundary

      implicit none

      integer i,j,k
      integer Nx,Ny,Nz
      integer counter_x
      integer counter_y
      integer Nx_Inf,Nx_Sup
      integer Ny_Inf,Ny_Sup
```

```
      integer Nz_Inf,Nz_Sup
      character*80 label
      double precision Pxi(0:600,0:600)
      double precision value

!*    Reading of the input data from file info.in

      open(unit=13,file='info.in',status='old')

      read(13,*) label
      read(13,*) Nx
      read(13,*) label
      read(13,*) Ny
      read(13,*) label
      read(13,*) Nz
      read(13,*) label
      read(13,*) Nx_Inf
      read(13,*) label
      read(13,*) Nx_Sup
      read(13,*) label
      read(13,*) Ny_Inf
      read(13,*) label
      read(13,*) Ny_Sup
      read(13,*) label
      read(13,*) Nz_Inf
      read(13,*) label
      read(13,*) Nz_Sup
      read(13,*) label
      read(13,*) value

      open(unit=32,file='output_volume',status='old')
      open(unit=35,file='output_boundary',status='unknown')
```

```
      Pxi(:,:)=0.0d0

!*   Reading, from file output_volume, of
!*   the coordinate values with label '0'or '1'
!*   corrisponding to long- or short-block points, respectively.

      do i=1,Nx
       do j=1,Ny

        read(32,*) Pxi(i,j)

       end do
      end do

!*   This 'do loop' starts from i=2 and j=2 and stops in
!*   i=Nx-1 and j=Ny-1, respectively,  because the next 'if' statements
!*   check for each point with value '1' the first and the second neighbours,
!*   and the coordinates at i=1, j=1,i=Nx, and j=Ny
!*   are not completely surrounded.


      do i=2,Nx-1
       do j=2,Ny-1

!*   If Pxi(i,j) is equal to label '1' it means that
!*   this is a boundary point
!*   of a 2D spherical short block microdomains.

        if (Pxi(i,j) .EQ. 1)  then

!*      Boundary rule:
```

```
!*      the previous point with label '1'
!*      will be for sure a boundary point of
!*      a 2D spherical short-block microdomain
!*      (and not an internal short-block microdomain point)
!*      if there is at least one neighbour
!*      point with label '0'
!*      (which belonges to the long-block matrix).

A)         if  (Pxi(i+1,j) .EQ. 0.0d0) then

!*      File fort.95 memorizes all coordinates of all points
!*      that belonges to the
!*      boundary of all 2D spherical short
!*      block microdomains. This is useful to check
!*      with gnuplot, a visualization program,
!*      if the algorithm is working properly.

          write(95,*) Pxi(i,j),i,j

         else
         if(Pxi(i-1,j) .EQ. 0.0d0 )  then

          write(95,*) Pxi(i,j),i,j

         else
         if (Pxi(i,j+1) .EQ. 0.0d0  ) then

          write(95,*) Pxi(i,j),i,j

         else
         if (Pxi(i,j-1) .EQ. 0.0d0  ) then
```

```
          write(95,*) Pxi(i,j),i,j

         else
         if (Pxi(i+1,j+1) .EQ. 0.0d0) then

           write(95,*) Pxi(i,j),i,j

         else
         if (Pxi(i+1,j-1) .EQ. 0.0d0) then

           write(95,*) Pxi(i,j),i,j

         else
         if (Pxi(i-1,j+1) .EQ. 0.0d0) then

            write(95,*) Pxi(i,j),i,j

         else
          if (Pxi(i-1,j-1) .EQ. 0.0d0) then

            write(95,*) Pxi(i,j),i,j

         else

!*       If the point with label '1', detected in the 'if' statement at A),
!*       does not belong to the boundary then, it is an inner point of a 2D
!*       spherical short-block microdomains.
!*       It will be
!*       temporary indicated with label '2' and the
!*       algorithm will continue evaluating other points.
```

```
           Pxi(i,j)=2.d0

          end if
          end if
          end if
          end if
          end if
          end if
          end if
          end if
          end if

        end do
      end do



      do i=1,Nx
        do j=1,Ny
         if (Pxi(i,j) .EQ. 1.0d0 ) then

          write(35,*) Pxi(i,j),i,j

         else

!*      All points which differ from value 1,
!*      boundary of a 2D spherical short-block microdomain,
!*      will assume value 0. Therefore, label '0' is now attribuited
!*      to the coordinates of the long-block points and to the
!*      inner points of a 2D spherical short-block microdomain.

          Pxi(i,j)= 0.0d0
```

```
      write(35,*)Pxi(i,j),i,j


     end if

    end do

  end do



    close(32)

    close(35)


  end program
```

```
!*********************************************************************
!*********************************************************************
!**
!** boundary_2.f90: A program which improves the identification
!** of the boundary for each 2D spherical short-block microdomain,
!** generated in output from the previous boundary.f90 code.
!** Boundary_2.f90 code won’t count as a boundary point the points
!** which have only one first neighbours
!** with value ’1’. Boundary_2.f90 needed to be introduced
!** in order to improve the quality in boundary point identification
!** which will be then useful for the calculation of the center of mass
!** of each 2D spherical short-block microdomain.
!**
!** Data: September 2011.
!** Location: Preston, UK.
!** Authors: Roberta Dessi & Marco Pinna.
!**
!**********************************************************************
!**********************************************************************
      program boundary_2

      implicit none

      integer i,j,k
      integer Nx,Ny,Nz
!       integer counter_x
!       integer counter_y
      integer Nx_Inf,Nx_Sup
      integer Ny_Inf,Ny_Sup
      integer Nz_Inf,Nz_Sup
      character*80 label
      double precision Pxi(0:600,0:600)
```

```
      double precision value

!*    Reading of the input data from file info.in

      open(unit=13,file='info.in',status='old')



      read(13,*) label
      read(13,*) Nx
      read(13,*) label
      read(13,*) Ny
      read(13,*) label
      read(13,*) Nz
      read(13,*) label
      read(13,*) Nx_Inf
      read(13,*) label
      read(13,*) Nx_Sup
      read(13,*) label
      read(13,*) Ny_Inf
      read(13,*) label
      read(13,*) Ny_Sup
      read(13,*) label
      read(13,*) Nz_Inf
      read(13,*) label
      read(13,*) Nz_Sup
      read(13,*) label
      read(13,*) value



      open(unit=73,file='output_boundary',status='old')
      open(unit=75,file='output_boundari_2',status='unknown')
```

```
      Pxi(:,:)=0.0d0

!*    Reading of the data input from file output_boundary

      do i=1,Nx
       do j=1,Ny

         read(73,*) Pxi(i,j)

       end do
      end do

!*   This 'do loop' starts from i=2 and j=2 and stops in
!*   i=Nx-1 and j=Ny-1, respectively,  because the next 'if' statement
!*   checks for each point with value '1' the first neighbours,
!*   and the coordinates at i=1, j=1,i=Nx, and j=Ny
!*   are not completely surrounded.


      do i=2,Nx-1
        do j=2,Ny-1

         if (Pxi(i,j) .EQ. 1)  then


          if(((Pxi(i+1,j).EQ.(1.0d0)).and.((Pxi(i-1,j)).EQ.(0.d0)).and.&
          & ((Pxi(i,j+1)).EQ.(0.d0)).and.((Pxi(i,j-1)).EQ.(0.d0))).or.&
          &  (((Pxi(i+1,j)).EQ.(0.d0)).and.((Pxi(i-1,j)).EQ.(1.d0)).and.&
          &  (Pxi(i,j+1).EQ.(0.0d0)).and.(Pxi(i,j-1).EQ.(0.0d0))).or.&
          &  ((Pxi(i+1,j).EQ.(0.0d0)).and.(Pxi(i-1,j).EQ.(0.0d0)).and.&
          &  (Pxi(i,j+1).EQ.(1.0d0)).and.(Pxi(i,j-1).EQ.(0.0d0))).or.&
          &  ((Pxi(i+1,j).EQ.(0.0d0)).and.(Pxi(i-1,j).EQ.(0.0d0)).and.&
```

```
          &  (Pxi(i,j+1).EQ.(0.0d0)).and.(Pxi(i,j-1).EQ.(1.0d0)))) then



!*   If the boundary point has only one first neighbour with value '1'
!*   then this point will be ignored as a boundary point and set equal to '0'



              Pxi(i,j) = 0.0d0

            else



!*   File fort.95 memorizes all boundary points of each
!*   2D spherical short-block microdomain. It is useful to check
!*   with gnuplot if our program is working properly.



              write(78,*) Pxi(i,j),i,j

            end if
           end if



         end do
        end do



!* All points, which differ from value '1',
!* will assume value 0.

        do i=1,Nx
         do j=1,Ny
```

```
  if (Pxi(i,j) .EQ. 1.0d0) then
     write(75,*)  Pxi(i,j)
   else
      Pxi(i,j)= 0.d0
      write(75,*)  Pxi(i,j)
  end if

 end do
end do



close(73)
close(75)



end program
```

```
!*********************************************************
!*********************************************************
!**
!** detective_point.f90: A program to calculate the
!** center of mass of each 2D spherical short-block
!** microdomain, by means the boundary detected as output
!** in the previous boundary_2.f90 code.
!** The boundary points of each microdomain
!** have label '1', and all other points
!** have label '0'. In detective_point.f90 a main do loop
!** will scan the structure from the begining each time that
!** a complete boundary of a microdomain is detected.
!** When a first point of a boundary (with label '1')
!** is detected by the main do loop,
!** a sub do loop will start running in order to check
!** all boundary points of the microdomain.
!** Upon detection of all boundary points of the microdomain,
!** the center of mass of the microdomain will be
!** calculated. After that, the main do loop will
!** scan the structure from the begining.
!** However, boundaries already detected will not be counted
!** again because are set with different label from those
!** that still need to be detected.
!**
!** Data: September 2011.
!** Location: Preston, UK.
!** Authors: Roberta Dessi & Marco Pinna.
!**
!*********************************************************
!*********************************************************


      program detective_point
```

```
      implicit none

      integer i,j,k,l,ll
      integer Nx,Ny,Nz
      integer i_new,j_new
      integer count_ro
      integer zz
      integer Nx_Inf,Nx_Sup
      integer Ny_Inf,Ny_Sup
      integer Nz_Inf,Nz_Sup
      REAL*8 counter_x
      REAL*8 counter_y
      REAL*8 cont
      double precision Pxi(0:600,0:600)
      double precision counter_xx(0:40000),counter_yy(0:40000)
      double precision value
      character*80 label


!* Reading of the input data from file info.in

      open(unit=13,file='info.in',status='old')

      read(13,*) label
      read(13,*) Nx
      read(13,*) label
      read(13,*) Ny
      read(13,*) label
      read(13,*) Nz
      read(13,*) label
      read(13,*) Nx_Inf
```

```
      read(13,*) label
      read(13,*) Nx_Sup
      read(13,*) label
      read(13,*) Ny_Inf
      read(13,*) label
      read(13,*) Ny_Sup
      read(13,*) label
      read(13,*) Nz_Inf
      read(13,*) label
      read(13,*) Nz_Sup
      read(13,*) label
      read(13,*) value



      l=1


      open(unit=62,file='output_boundari_2',status='old')
      open(unit=65,file='detect_point',status='unknown')


      Pxi(:,:)=0.0d0


      zz=0.0d0
      count_ro=0.0d0


!*  Reading of the input data from file output_boundari_2


      do i=1,Nx
       do j=1,Ny


         read(62,*) Pxi(i,j)


       end do
```

```
      end do




!* The main do loop detectes the first
!* point of a boundary microdomain, and
!* once detected a complete microdomain by
!* the sub do loop, the main do loop re-starts
!* from the begining.
!* Boundaries, that have been already detected,
!* are indicated with label '2', so that, during
!* a new scan they will not be
!* considered again.

      do i=1,Nx
       do j=1,Ny


        counter_x =0.0d0
        counter_y =0.0d0
        cont=0.0d0

!* Pxi(i,j) = 1 means that the point at (i,j)
!* is a boundary point of a microdomain


        if (Pxi(i,j) .EQ. 1)  then

!* As a consequence of the previos 'if' statement some
!* variables will be updated:
!* zz=0 means that a boundary point of a microdomain
!* has been detected and the sub do loop can run to detect
!* the all other boundary points of the microdomain;
!* counter_x=i and counter_y=j memorize the values of the
```

```
!* coordinates of the (i,j) boundary point of the microdomain;
!* cont =1.0d0 counts the number of points of the microdomain
!* boundary.

           zz=0
           cont= 1.0d0
           counter_x= i
           counter_y= j
           Pxi(i,j)= 2.0d0

!* New index i_new and j_new have been defined in the sub
!* do loop, as i and j of the main do loop, respectively,
!* in order to scan the boundary points of the
!* microdomain.


           i_new=i
           j_new=j

          do while ((zz)  .EQ. 0.0d0)

!* If the value of the first neighbours
!* (in anticlock wise) is equal to '1' it means that it is
!* an other boundary point of the microdomain

           if  (Pxi(i_new,j_new-1) .EQ. 1.0d0) then

!* Updating of some variables.


               i_new=i_new
               j_new=j_new-1
```

```
    counter_x=counter_x+i_new

    counter_y=counter_y+j_new

    cont=cont+1.0d0

    Pxi(i_new,j_new)= 2.0d0


else

if(Pxi(i_new+1,j_new) .EQ. 1.0d0 )  then

     i_new=i_new+1

     j_new=j_new

     counter_x=counter_x+i_new

     counter_y=counter_y+j_new

     cont=cont+1.0d0

     Pxi(i_new,j_new)= 2.0d0


else

if (Pxi(i_new,j_new+1) .EQ. 1.0d0  ) then


    i_new=i_new

    j_new=j_new+1

    counter_x=counter_x+i_new

    counter_y=counter_y+j_new

    cont=cont+1.0d0

    Pxi(i_new,j_new)= 2.0d0


else

if (Pxi(i_new-1,j_new) .EQ. 1.0d0  )  then


    i_new=i_new-1

    j_new=j_new

    counter_x=counter_x+i_new

    counter_y=counter_y+j_new

    cont=cont+1.0d0
```

```
               Pxi(i_new,j_new)= 2.0d0

           else

!* If none of these 'if' statements are true, it means that
!* all boundary points of the microdomain have been identified, and
!* the variable zz can be set equal to '1',
!* then it is possible go out from the do while loop.

           zz=1

           end if
           end if
           end if
           end if

         end do

!* The center of mass is calculated as:
```

!* $x_c = \sum_{i=1}^{N} \frac{x_i}{N}$ and $y_c = \sum_{i=1}^{N} \frac{y_i}{N}$, where x_i and y_i

```
!* are the coordinates of the
!* i-esim point of the boundary, and N is the total number of the
!* points of the microdomain boundary.

           counter_xx(l) = counter_x / (cont)
           counter_yy(l) = counter_y / (cont)

!* The variable count_ro count the total number of center of mass
!* in the structure.

           count_ro=l
           l=l+1
```

```
  end if



 end do
end do

  write(65,*) count_ro

 do ll=1,count_ro

       write(65,*) counter_xx(ll),counter_yy(ll)

 end do

  counter_xx(:)=0.0d0
  counter_yy(:)=0.0d0
  l=1.0d0
  ll=0.0d0

close(62)
close(65)

end program
```

References

[1] Ruzette, A. V.; Leibler, L. *Nature Materials* **2005**, *4*, 19.

[2] Bates, F.; Fredrickson, G. *Physics Today* **1999**, *52*, 32.

[3] Matsen, M. W. *Macromolecules* **2012**, *45*, 2161.

[4] Hur, S.-M.; Garcia-Cervera, C. J.; Kramer, E. J.; Fredrickson, G. H. *Macromolecules* **2009**, *42*, 5861.

[5] Herr, D. J. C. *Journal Material Research* **2011**, *26*, 233.

[6] Ryan., A. J.; Hamley, I. W. *The Physics of Glassy Polymers*; Springer, 1997.

[7] Qi, S.; Wang, Z. W. *Physical Review E* **1997**, *55*, 1682.

[8] Matsen, M. W. *Journal of Chemical Physics* **2001**, *114*, 8165.

[9] Schick, M. *Physica A* **1998**, *251*, 1.

[10] Vigild, M. E.; Almdal, K.; Mortensen, K.; Hamley, I. W.; Fairclough, J. P. A.; Ryan, J. *Macromolecules* **1998**, *31*, 5702.

[11] Bates, F. S.; Fredrickson, G. H. *Annual Review of Physical Chemistry* **1990**, *41*, 525.

[12] Feng, J.; Ruckenstein, E. *Journal of Chemical Physics* **2004**, *121*, 1609.

[13] Sloan, C. R. S.; Thomas, E. L. *European Polymer Journal* **2011**, *47*, 630.

[14] Farrell, H. A. *Nanoscale* **2012**, *4*, 3228.

[15] Kim, H.; Jia, X.; Stafford, C.; Kim, D.; McCarthy, T.; Tuominen, M.; Hawker, C.; Russell, T. *Advanced Materials* **2001**, *13*, 795.

[16] Lopes, W.; Jaeger, H. *Nature* **2001**, *414*, 735.

[17] Thurn-Albrecht, T.; Schotter, J.; Kastle, G.; Emley, N.; Stubauchui, T.; Krusin-Elbaum, L.; Black, C.; Tuominen, M.; Russell, T. *Science* **2000**, *290*, 2126.

[18] Chan, V. Z.-H.; Hoffman, J.; Lee, V. Y.; Iatrou, H.; Avgeropoulos, A.; Hadjichristidis, N.; Miller, R. D.; Thomas, E. L. *Science* **1999**, *286*, 1716.

[19] Li, R. R.; Dapkus, P. D.; Thompson, M. E.; Jeong, W. G.; Harrison, C.; Chaikin, P. M.; Register, R. A.; Adamson, D. H. *Applied Physics Letters* **2000**, *76*, 1689.

[20] Cheng, J.; Ross, C.; Chan, V.; Thomas, E.; Lammertink, R.; Vancso, G. *Advanced Materials* **2001**, *13*, 1174.

[21] Black, C.; Guarini, K.; Milkove, K.; Baker, S.; Russell, T.; Tuominen, M. *Applied Physics Letters* **2001**, *79*, 409.

[22] Broz, P.; Driamov, S.; Ziegler, J.; Ben-Haim, N.; Marsch, S.; Meier, W.; Hunziker, P. *Nano Letters* **2006**, *6*, 2349.

[23] Chen, W.-Q.; Wei, H.; Li, S.-L.; Feng, J.; Nie, J.; Zhang, X.-Z.; Zhuo, R.-X. *Polymer* **2008**, *49*, 3965.

[24] *Nanostructured Soft Matter*; Zvelindovsky, A. V. Ed., Springer,Dordrecht, 2007.

[25] Hamley, I. W. *Macromolecular Theory and Simulations* **2000**, *9*, 363.

[26] Glotzer, S. C.; Paul, W. *Annual Review of Materials* **2002**, *32*, 401.

[27] Zeng, Q. H.; Yu, A. B.; Lu, G. Q. *Progress in Polymer Science* **2008**, *33*, 191.

[28] Pinna, M.; Zvelindovsky, A. V. *Europian Physical Journal B* **2012**, *85*, 210.

[29] Guo, X.; Pinna, M.; Zvelindovsky, A. V. *Parallel Scientific Computing and Optimization: Advances and Applications. Springer Series in Optimization and Its Applications*; Springer, New York, 2009; Vol. 27, p 253.

[30] Guo, X.; Pinna, M.; Zvelindovsky, A. V. *Macromolecular Theory and Simulations* **2007**, *16*, 779.

[31] Pinna, M. *Mesoscale Modelling of Block Copolymer Systems A Computational Study*; Verlag Dr. Müller, Saarbrücken, 2010.

[32] Oono, Y.; Puri, *Physical Review Letter* **1987**, *58*, 836.

[33] Oono, Y.; Puri, S. *Physical Review A* **1988**, *38*, 434.

[34] Feng, J.; Liu, H.; Hu, Y.; Prausnitz, J. M. *Chemical Engineering Science* **2004**, *59*, 1701.

[35] Teixeira, P. I. C.; Mulder, B. M. *Physical Review E* **1996**, *53*, 1805.

[36] Wang, D.; Shi, T.; An, L.; Jia, Y. *Journal of Chemical Physics* **2008**, *129*, 194903.

[37] Zhou, D.; Shi, A. C.; Zhang, P. *Journal of Chemical Physics* **2008**, *129*, 154901.

[38] Chen, X. B.; Niu, L. S.; Shi, H. J. *Biophysical Chemistry* **2008**, *135*, 84.

[39] Pinna, M.; Zvelindovsky, A. V.; Todd, S.; Goldbeck-Wood, G. *Journal of Chemical Physics* **2006**, *125*, 154905.

[40] Zvelindovsky, A. V.; Sevink, G. J. A. *Europhysics Letter* **2003**, *62*, 370.

[41] Lyakhova, K. S.; Zvelindovsky, A. V.; Sevink, G. J. A. *Macromolecules* **2006**, *39*, 3024.

[42] Xu, T.; Zvelindovsky, A. V.; Sevink, G. J. A.; Gang, O.; Ocko, B.; Zhu, Y.; Gido, S. P.; Russell, T. P. *Macromolecules* **2004**, *37*, 6980.

[43] Pinna, M.; Guo, X.; Zvelindovsky, A. V. *Journal of Chemical Physics* **2009**, *131*, 214902.

[44] Sevink, G. J. A.; Zvelindovsky, A. V. *Journal of Chemical Physics* **2008**, *128*, 084901.

[45] Sevink, G. J. A.; Zvelindovsky, A. V.; Fraaije, J. G. E. M.; Huinink, H. P. *Journal of Chemical Physics* **2001**, *115*, 8226.

[46] Pinna, M.; Pagonabarraga, I.; Zvelindovsky, A. V. *Macromolecular Theory and Simulations* **2011**, *20*, 769.

[47] Ohta, T.; Enomoto, Y.; Harden, J. L.; Doi, M. *Macromolecules* **1993**, *26*, 4928.

[48] Bahiana, M.; Oono, Y. *Physical Review A* **1990**, *41*, 6763.

[49] Ohta, T.; Kawasaki, K. *Macromolecules* **1986**, *19*, 2621.

[50] Ren, S. R.; Hamley, I. W. *Macromolecules* **2001**, *34*, 116.

[51] Leibler, L. *Macromolecules* **1980**, *13*, 1602.

[52] Lyakhova, K. S. *Mesoscale Modelling of Block Copolymers Under External Fields*; 2005, p.126.

[53] Xu, J.; Russell, T. P.; Ocko, B. M.; Checco, A. *Soft Matter* **2011**, *7*, 3915.

[54] Segalman, R.; Yokoyama, H.; Kramer, E. J. *Advanced Materials* **2001**, *13*, 1152.

[55] Hexemer, A.; Stein, G.; Kramer, E.; Magonov, S. *Macromolecules* **2005**, *38*, 7083.

[56] Cheng, J. Y.; Ross, C. A.; Smith, H. I.; Thomas, E. L. *Advanced Materials* **2006**, *18*, 2505.

[57] Segalman, R. A. *Material Science and Enginering R* **2005**, *48*, 191.

[58] Park, S.; Lee, D. H.; Xu, J.; Kim, B.; Hong, S. W.; Jeong, U.; Xu, T.; Russell, T. P. *Science* **2009**, *323*, 1030.

[59] Rockford, L.; Liu, Y.; Mansky, P.; Russell, T.; Yoon, M.; Mochrie, S. *Physical Review Letters* **1999**, *82*, 2602.

[60] Kim, S.; Solak, H.; Stoykovich, M.; Ferrier, N.; de Pablo, J.; Nealey, P. *Nature* **2003**, *424*, 411.

[61] Xu, J.; Park, S.; Wang, S.; Russell, T. P.; Ocko, B. M.; Checco, A. *Advanced Materials* **2010**, *22*, 2268.

[62] Bita, I.; Yang, J. K. W.; Jung, Y. S.; Ross, C. A.; Thomas, E. L.; Berggren, K. K. *Science* **2008**, *321*, 939.

[63] Ruiz, R.; Kang, H.; Detcheverry, F. A.; Dobisz, E.; Kercher, D. S.; Albrecht, T. R.; de Pablo, J. J.; Nealey, P. F. *Science* **2008**, *321*, 936.

[64] Park, S.-M.; Stoykovich, M. P.; Ruiz, R.; Zhang, Y.; Black, C. T.; Nealey, P. E. *Advanced Materials* **2007**, *19*, 607.

[65] Bosse, A. W.; Garcia-Cervera, C. J.; Fredrickson, G. H. *Macromolecules* **2007**, *40*, 9570.

[66] Kawakatsu, T. *Statistical Physics of Polymers*; Springer, Berlin, 2001.

[67] Cahn, J. W.; Hilliard, J. E. *Journal of Chemical Physics* **1957**, *28*, 258.

[68] Cook, H. E. *Acta Metall* **1970**, *18*, 297.

[69] Fraaije, J. G. E. M. *Journal of Chemical Physics* **1993**, *99*, 9202.

[70] Drolet, F.; Fredrickson, G. H. *Physical Review Letters* **1999**, *83*, 4317.

[71] Knoll, A.; Lyakhova, K. S.; Horvat, A.; Krausch, G.; Sevink, G. J. A.; Zvelindovsky, A. V.; Magerle, R. *Nature Materials* **2004**, *3*, 886.

[72] Pinna, M.; Zvelindovsky, A. V.; Guo, X.; Stokes, C. L. *Soft Matter* **2011**, *7*, 6991.

[73] Pinna, M.; Zvelindovsky, A. V. *Soft Matter* **2008**, *4*, 316.

[74] Ly, D. Q.; Honda, T.; Kawakatsu, T.; Zvelindovsky, A. V. *Macromolecules* **2007**, *40*, 2928.

[75] Honda, T.; Kawakatsu, K. *Macromolecules* **2006**, *39*, 2340.

[76] Zvelindovsky, A. V.; Sevink, G. J. A. *Physical Review Letters* **2003**, *90*, 049601.

[77] Pinna, M.; Schreier, L.; Zvelindovsky, A. V. *Soft Matter* **2009**, *5*, 970.

[78] Sevink, G. J. A.; Pinna, M.; Langner, K.; Zvelindovsky, A. V. *Soft Matter* **2011**, *7*, 5161.

[79] Pinna, M.; Hiltl, S.; Guo, X.; Böker, A.; Zvelindovsky, A. V. *ACS Nano* **2010**, *4*, 2845.

[80] Hamley, I. W. *The Physics of Block Copolymers*; Oxford University Press, Oxford, 1998.

[81] Jung, J.; Park, H. W.; Lee, S.; Lee, H.; Chang, T.; Matsunaga, K.; Jinnai, H. *ACS Nano* **2010**, *4*, 3109.

[82] Matsen, M. W. *Journal Chemical Physics* **1997**, *106*, 7781.

[83] Tsori, Y.; Andelman, D.; Lin, C.-Y.; Schick, M. *Macromolecules* **2006**, *39*, 289.

[84] Anastasiadis, S. H.; Russell, T. P.; Satija, S. K.; Majkrzac, C. F. *Physical Review Letters* **1989**, *62*, 1852.

[85] Kikuchi, M.; Binder, K. *Journal of Chemical Physics* **1994**, *101*, 3367.

[86] Fredrickson, G. H. *Macromolecules* **1987**, *20*, 2535.

[87] Stein, G. E.; Cochran, E. W.; Katsov, K.; Fredrickson, G. H.; Kramer, E. J.; Li, X.; Wang, J. *Physical Review Letters* **2007**, *98*, 158302.

[88] Wang, Q.; Nealey, P. F.; de Pablo, J. J. *Macromolecules* **2001**, *34*, 3458.

[89] Lyakhova, K. S.; Sevink, G. J. A.; Zvelindovsky, A. V.; Horvat, A.; Magerle, R. *Journal of Chemical Physics* **2004**, *120*, 1127.

[90] Huinink, H. P.; van Dijk, M. A.; Brokken-Zijp, J. C. M.; Sevink, G. J. A. *Macromolecules* **2001**, *34*, 5325.

[91] Harrison, C.; Park, M.; Chaikin, P.; Register, R. A.; Adamson, D. H.; Yao, N. *Macromolecules* **1998**, *31*, 2185.

[92] Karim, A.; Singh, N.; Sikka, M.; Bates, F. S.; Dozier, W. D.; Felcher, G. P. *Journal of Chemical Physics* **1994**, *100*, 1620.

[93] Konrad, M.; Knoll, A.; Krausch, G.; Magerle, R. *Macromolecules* **2000**, *33*, 5518.

[94] Chremos, A.; Margaritis, K.; Panagiotopoulos, A. Z. *Soft Matter* **2010**, *6*, 3588.

[95] Morkved, T. L.; Lu, M.; Urbas, A. M.; Ehrichs, E. E.; Jaeger, H. M.; Mansky, P.; Russell, T. P. *Science* **1996**, *273*, 931.

[96] Hamley, I. W. *Journal of Physics: Condensed Matter* **2001**, *13*, 643.

[97] Arya, G.; Panagiotopoulos, A. Z. *Physical Review E* **2004**, *70*, 031501.

[98] Angelescu, D. E.; Waller, J. H.; Adamson, D. H.; Deshpande, P.; Chou, S. Y.; Register, R. A.; Chaikin, P. M. *Advanced Materials* **2004**, *16*, 1736.

[99] Ly., D. Q.; Honda, T.; Kawakatsu, T.; Zvelindovsky, A. V. *Macromolecules* **2008**, *41*, 4501.

[100] Hong, Y.-R.; Adamson, D. H.; Chaikin, P. M.; Register, R. A. *Soft Matter* **2009**, *5*, 1687.

[101] Chremos, A.; Chaikin, P. M.; Register, R. A.; Panagiotopoulos, A. Z. *Soft Matter* **2012**, *8*, 7803.

[102] Kim, S. Y.; Nunns, A.; Gwyther, J.; Davis, R. L.; Manners, I.; Chaikin, P. M.; Register, R. A. *Nano Letters* **2014**, *14*, 5698.

[103] Nikoubashman, A.; Davis, R. L.; Michal, B. T.; Chaikin, P. M.; Register, R. A.; Panagiotopoulos, A. Z. *ACS Nano* **2014**, *8*, 8015.

[104] Davis, R. L.; Chaikin, P. M.; Register, R. A. *Macromolecules* **2014**, *47*, 5277.

[105] Ludwigs, S.; Böker, A.; Voronov, A.; Rense, N.; Magerle, R.; Krausch, G. *Nature Matter* **2003**, 744.

[106] Kim, J. K.; Lee, J. I.; Lee, D. H. *Macromolecular Research* **2008**, *16*, 267.

[107] Harrison, C.; Adamson, D.; Cheng, Z.; Sebastian, J.; Sethuraman, S.; Huse, D.; Register, R.; Chaikin, P. *Science* **2000**, *290*, 1558.

[108] Dessí, R.; Pinna, M.; Zvelindovsky, A. V. *Macromolecules* **2013**, *46*, 1923.

[109] Kim, G.; Libera, M. *Macromolecules* **1998**, *31*, 2569.

[110] Mecke, K. R.; Stoyan, D. *The Art of Analysing and Modelling Spatial Structures and Pattern Formation. Lecture Notes in Physics*; Springer, Berlin, 2000.

[111] Hamley, I. W.; Pople, J. A.; Fairclough, J. P. A.; Terrill, N. J.; Ryan, A. J.; Booth, C.; Yu, G.-E.; Diat, O.; Almdal, K.; Mortensen, K.; Vigild, M. *Journal of Chemical Physics* **1998**, *108*, 6929.

[112] Yang, R.; Li, B.; Shi, A.-C. *Langumuir* **2012**, *28*, 1569.

[113] Kellogg, G. J.; Walton, D. G.; Mayes, A. M.; Lambooy, P.; Russell, T. P.; Gallagher, P. D.; Satija, S. K. *Physical Review Letters* **1996**, *76*, 2503.

[114] Tsarkova, L. *Nanostructured Soft Matter*; Zvelindovsky A. V. Ed., Springer, Dordrecht, 2007; p 231.

[115] Xu, T.; Wang, J.; Russell, T. P. *Nanostructured Soft Matter*; Zvelindovsky A. V. Ed., Springer, Dordrecht, 2007; p 171.

[116] Huang, E.; Russell, T. P.; Harrison, C.; Chaikin, P. M.; Register, R. A.; Hawker, C. J.; Mays, J. *Macromolecules* **1998**, *31*, 7641.

[117] Wang, Q.; Qiliang, Y.; Nealey, P. F.; de Pablo, J. J. *Macromolecules* **2000**, *33*, 4512.

[118] Horvat, A.; Lyakhova, K. S.; Sevink, G. J. A.; Zvelindovsky, A. V.; Magerle, R. *Journal of Chemical Physics* **2004**, *120*, 1117.

[119] Ludwigs, S.; Krausch, G.; Magerle, R.; Zvelindovsky, A. V.; Sevink, G. J. A. *Macromolecules* **2005**, *38*, 1859.

[120] Horvat, A.; Sevink, G. J. A.; Zvelindovsky, A. V.; Krekhov, A.; Tsarkova, L. *ACS Nano* **2008**, *2*, 1143.

[121] Wang, Q. *Nanostructured Soft Matter*; Zvelindovsky A. V. Ed., Springer, Dordrecht, 2007; p 495.

[122] Knoll, A.; Horvat, A.; Lyakhova, K. S.; Krausch, G.; Sevink, G. J. A.; Zvelindovsky, A. V.; Magerle, R. *Physical Review Letters* **2002**, *89*, 035501.

[123] Knoll, A.; Magerle, R.; Krausch, G. *Journal of Chemical Physics* **2004**, *120*, 1105.

[124] Xiang, H.; Shin, K.; Kim, T.; Moon, S. I.; McCarthy, T. J.; Russell, T. P. *Macromolecules* **2004**, *37*, 5660.

[125] Shin, K.; Xiang, H.; Moon, S. I.; Kim, T.; McCarthy, T. J.; Russell, T. P. *Science* **2004**, *306*, 76.

[126] Wu, Y.; Chen, G.; Katsov, K.; Sides, S. W.; Wang, J.; Tang, J.; Fredrickson, G. H.; Moskovits, M.; Stucky, G. D. *Nature Materials* **2004**, *3*, 816.

[127] Xiang, H.; Shin, K.; Kim, T.; Moon, S.; McCarthy, T. J.; Russell, T. P. *Journal of Polymer Science: Part B: Polymer Physics* **2005**, *43*, 3377.

[128] Li, W.; Wickham, R. A.; Garbary, R. A. *Macromolecules* **2006**, *39*, 806.

[129] Chen, P.; He, X.; Liang, H. *Journal of Chemical Physics* **2006**, *124*, 104906.

[130] Wang, Z.; Li, B.; Jin, Q.; Ding, D.; Shi, A.-C. *Macromolecular Theory and Simulations* **2008**, *17*, 86.

[131] He, X.; Song, M.; Liang, H.; Pan, C. *Journal of Chemical Physics* **2001**, *114*, 10510.

[132] Yu, B.; Sun, P.; Chen, T.; Jin, Q.; Ding, D.; Li, B.; Shi, A.-C. *Physical Review Letters* **2006**, *96*, 138306.

[133] Feng, J.; Liu, H.; Hu, Y. *Macromolecular Theory and Simulations* **2006**, *15*, 674.

[134] Wang, Z.; Li, B.; Jin, Q.; Ding, D.; Shi, A.-C. *Macromolecular Theory and Simulations* **2008**, *17*, 301.

[135] Feng, J.; Ruckenstein, E. *Macromolecules* **2006**, *39*, 4899.

[136] Xiao, X.; Huang, Y.; Liu, H.; Hu, Y. *Macromolecular Theory and Simulations* **2007**, *16*, 732.

[137] Chen, P.; Liang, H.; Shi, A.-C. *Macromolecules* **2007**, *40*, 7329.

[138] Fraaije, J. G. E. M.; Sevink, G. J. A. *Macromolecules* **2003**, *36*, 7891.

[139] Yabu, H.; Higuchi, T.; Ijiro, K.; Shimomura, M. *Chaos* **2005**, *15*, 047505.

[140] Chen, P.; Liang, H.; Shi, A.-C. *Macromolecules* **2008**, *22*, 8938.

[141] Yu, B.; Li, B.; Jin, Q.; Ding, D.; Shi, A.-C. *Macromolecules* **2007**, *40*, 9133.

[142] Sevink, G. J. A.; Zvelindovsky, A. V. *Macromolecules* **2005**, *38*, 7502.

[143] Chantawansri, T. L.; Bosse, A. W.; Hexemer, A.; Ceniceros, H. D.; Garciá-Cervera, C. J.; Kramer, E. J.; Fredrickson, G. H. *Physical Review E* **2007**, *75*, 031802.

[144] Uneyama, T. *Journal of Chemical Physics* **2007**, *126*, 114902.

[145] Rider, D. A.; Chen, J. I. L.; Eloi, J.-C.; Arsenault, A. C.; Russell, T. P.; Ozin, G. A.; Manners, I. *Macromolecules* **2008**, *41*, 2250.

[146] Vorselaars, B.; Kim, J. U.; Chantawansri, T. L.; Fredrickson, G. H.; Matsen, M. W. *Soft Matter* **2011**, *7*, 5128.

[147] Miao, B.; Tulkens, J.; Li, W.; Wickham, R. A. *Bulletin of the American Physical Society, APS March Meeting* **2008**.

[148] Fasolka, M. J.; Mayes, A. M. *Ann. Rev. Mat. Res.* **2001**, *31*, 323.

[149] Stoykovich, M. P.; Nealey, P. F. *Materials Today* **2006**, *9*, 20–29.

[150] Mansky, P.; Liiu, Y.; Huang, E.; Russel, T. P.; Hawker, C. *Science* **1997**, *275*, 1458.

Curriculum Vitae

The author of this thesis was born on 8 January 1982 in Cagliari, Sardinia, Italy. In July 2001 she obtained a high school degree from scientific lycée 'Edoardo Amaldi' in Carbonia, Sardinia. On October 2010 she graduate from the University of Cagliari (Italy) with a Laurea Degree in Electronic Engineering. She wrote an undergraduated thesis 'Atomistic study of the structural property of nano hybrid system for photovoltaic applications' under the supervision of Prof. Luciano Colombo, Dr. Alessandro Mattoni, and Dr. Claudio Melis. In January 2011 she started working on her PhD project under supervision of Prof. Andrei V. Zvelindovsky and Dr. Marco Pinna in the School of Mathematics and Physics in the United Kingdom. She studied structure formation and dynamics of phase transitions of block copolymer under external fields, described in the present thesis. During her PhD studies the author attended several UK and international conferences, winter and summer schools. During international Workshop Computational condensed matter in Whitehaven, the Lake District, UK, 7-9 September 2014 she received a Springer Poster prize for her contribution'The Cell Dynamics Simulations of Cylinder-Forming Diblock Copolymers in Thin Films on Topographical and Chemically Patterned Substrates'.